Nonlinear force-free reconstruction of the coronal magnetic field with advanced numerical methods

Von der Fakultät für Elektrotechnik, Informationstechnik, Physik
der Technischen Universität Carolo-Wilhelmina
zu Braunschweig
zur Erlangung des Grades eines
Doktors der Naturwissenschaften
(Dr.rer.nat.)
genehmigte
Dissertation

von **Tilaye Tadesse Asfaw**
aus Boroda/ Eastern Harrarge, Ethiopia

Bibliografische Information der Deutschen Nationalbibliothek

Die Deutsche Nationalbibliothek verzeichnet diese Publikation in der Deutschen Nationalbibliografie; detaillierte bibliografische Daten sind im Internet über `http://dnb.d-nb.de` abrufbar.

1. Referentin oder Referent: Prof. Dr. Karl-Heinz Glaßmeier
2. Referentin oder Referent: Prof. Dr. Sami K. Solanki

eingereicht am: 05.01.2011

mündliche Prüfung (Disputation) am: 01.03.2011

ISBN 978-3-942171-45-8

uni-edition GmbH 2011

http://www.uni-edition.de

Printed in Germany

Contents

Summary

Magnetic fields play a key role in the physics of the solar surface and atmosphere and in solar activity in particular. To understand the physical mechanism of any of the activity phenomena observable in the solar atmosphere one needs to know the underlying magnetic field. The magnetic field also provides the link between different manifestations of solar activity like, for instance, sunspots, flares, or coronal mass ejections. Therefore, there is a strong need for information about the magnetic vector throughout the solar atmosphere. Routine measurements of the solar magnetic field are still mainly carried out in the photosphere. Therefore, one has to infer the field strength in the higher layers of the solar atmosphere from the measured photospheric field based on the assumption that the corona is force-free. This approach assumes that the Lorentz force vanishes, i.e. that the magnetic field and the electric currents are co-aligned with each other. This is justified in regions where the ratio of the plasma pressure to the magnetic pressure and flow speeds to Alfven speed are significantly lower than unity. This is true in large parts of the chromosphere and corona while the photosphere is a region where this assumption is not warrantable. The procedure used to infer the 3D coronal magnetic field is known as magnetic field extrapolation.

Extrapolation codes in cartesian geometry for modelling the magnetic field in the corona do not take the curvature of the Sun's surface into account and can only be applied to relatively small areas, e.g., a single active region. Within this thesis, we develop numerical methods to carryout magnetic field extrapolation into solar corona from the photospheric boundary using spherical geometry. The computational box can then be chose as large that can accommodate much of the connectivity between neighbouring solar active regions. The method minimizes the volume-integrated force-free and solenoidal condition for the magnetic field vector simultaneously. Since we use routine measurements of the photospheric field vector as an input for our numerical method (as lower boundary condition), we have to "preprocess" the photospheric data in order to achieve boundary conditions that are consistent with the force-free assumption. We also extend the preprocessing algorithm of Wiegelmann et al. (2006) to spherical geometry which approximates the physics at a chromospheric level as it transforms an observed, not force-free, photospheric magnetic field to a nearly force-free, chromospheric-like state. The method minimizes a functional in spherical geometry so that the preprocessed magnetogram suffices the force-balance and torque-balance conditions (Molodensky 1969, 1974) in such a way that the optimized boundary condition stays close to the measured photospheric data and is sufficiently smooth. From these consistent boundary conditions, we are then able to reconstruct nonlinear force-free fields. While potential fields, only need the longitudinal (line-of-sight) component of the photospheric magnetic field as an input, the more general approach of nonlinear force-free fields, needs the longitudinal component of the photo-

spheric electric current in addition. In our approach, we make use of the full photospheric magnetic field vector as input. We also calculate the corresponding potential fields in the computational domain from the normal component of the surface field at the photosphere at $r = 1R_\odot$, which is used as initial condition for the code. With these prerequisites, we are able to investigate the topology of the 3D coronal magnetic field above solar active regions and to estimate the related physical quantities such as the magnetic energy content, the free magnetic energy (which can partly be released during solar eruptions) and the magnetic energy density (i.e. the amount of stored magnetic energy per unit volume) for larger field of views.

In particular, we solve the nonlinear force-free field equations by minimizing a functional in spherical coordinates over a restricted area of the Sun. We extend the functional by an additional term, which allows to incorporate measurement error and treat regions with missing observational data. We use vector magnetograph data from the Synoptic Optical Long-term Investigations of the Sun survey (SOLIS) to model the coronal magnetic field. We study two neighbouring magnetically connected active regions observed on May 15 2009 and three neighbouring active regions observed on March 28, 29, and 30 2008. For vector magnetograms with variable measurement precision and randomly scattered data gaps (e.g., SOLIS/VSM) the new code yields field models which satisfy the solenoidal and force-free condition significantly better, as it allows deviations between the extrapolated boundary field and observed boundary data within measurement errors. Data gaps are assigned to an infinite error. We extend this new scheme to spherical geometry and apply it for the first time to real data.

1 Solar atmosphere and the importance of its magnetic field

The sun is a magnetically "active" star in the center of our solar system. But compared to other cool stars it is considered rather quiet. It is the only star on which we can resolve physical processes down to some important scales. Sunspots are the most readily visible manifestations of solar magnetic field concentrations and of their interaction with the Sun's plasma. It was the rediscovery of sunspots by Galilei, Scheiner and others around 1611, with the help of the then newly invented telescope, that marked the beginning of the systematic study of the Sun in the western world and heralded the dawn of research into the Sun's physical character (Solanki 2003). Over the last years, several satellite missions such as *Ulysses*, *Yohkoh*, SOHO, TRACE, RHESSI, Hinode (SOLAR-B), STEREO and ground-based observations such as the solar flare telescope/NAOJ (Sakurai et al. 1995), the imaging vector magnetograph/MEES Observatory (Mickey et al. 1996), Big Bear Solar Observatory, VTT, SST (La Palma), DST/NSO (Sacramento Peak) and SOLIS/NSO (Henney et al. 2008) have helped to improve our understanding about the Sun (Domingo 2002, Bhatnagar and Livingston 2005). The magnetic field of the Sun is an important quantity which couples the solar interior with the photosphere and atmosphere (Solanki 2004a). Observations have shown that physical conditions in the solar atmosphere are strongly controlled by solar magnetic field. The appearance of photospheric, chromospheric and coronal structures, including active regions and flares, seen in enhanced emissions in Hα and different lines in the ultraviolet and extreme-ultraviolet as well as in white light observations, provides evidence of the prevalent nature and importance of the solar magnetic field. As a matter of fact, to understand the physics of active regions, the storage and release of flare energy, and the formation of hot plasmas and mass ejections, it is necessary that we understand and study the 3D structure of the coronal magnetic field. In this chapter, the focus lies on the structures of the solar atmosphere and the importance of its magnetic field.

In the following, an overview of the solar atmosphere and its structure will be emphasized in § 1.1. The phenomenological examples of the dominant role of coronal magnetic field and its direct measurement techniques are outlined in § 1.2. Finally, the basic principles and assumptions of force-free magnetic field are discussed in § 1.3.

1.1 The solar atmosphere

The properties of the surface layers of the Sun are very important to understand many physical phenomena and the relationships between each other. The surface layers of the

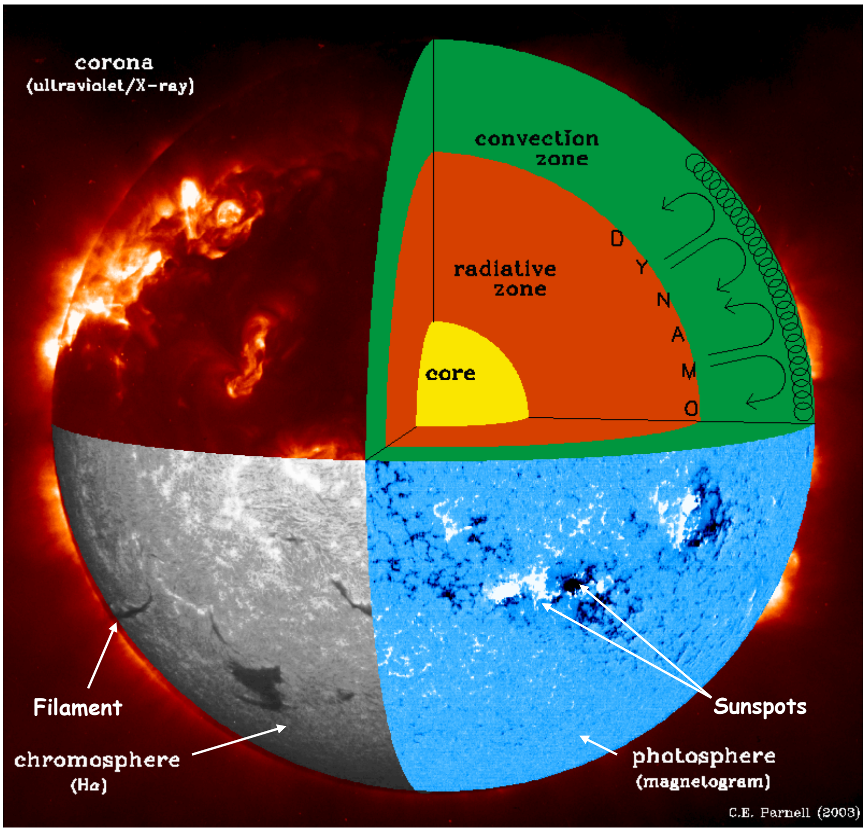

Figure 1.1: Basic overview of the Sun's constituent parts. The cut-out shows the three major interior zones: the core, the radiative zone, and the convection zone. (Courtesy of C. E. Parnel).

Sun are shown in Fig. 1.1. The region above the visible surface of the Sun including the *photosphere*, *chromosphere*, *transition region*, and *corona* is known as the solar atmosphere. One should not visualize these layers as spherical shells, but as physical regimes with different physical properties (Benz 2002). The Sun's atmosphere becomes less dense as one moves outwards and upwards (see Fig. 1.4). The atmosphere involves a range of structures and dynamical phenomena including sunspots, fibrils, spicules and 'bright points', to mention only a few, all of which need to be explained if we are to say that we understand the solar atmosphere. Improved understanding depends crucially on the acquisition of improved diagnostic data with high spectral and spatial resolution (Sturrock et al. 1986). In the next few subsections, the general overviews of each atmospheric layers will be emphasized independently.

1.1.1 Photosphere

The lowest atmospheric layer, called the *photosphere*, is an extremely thin and visible surface layer of the Sun where most photons interact with atoms a last time before escaping from the Sun. Its has a temperature between 4500K and 6000K and the overall density is about $10^{17} cm^{-3}$. The photosphere is covered by granulation, which represents the tops

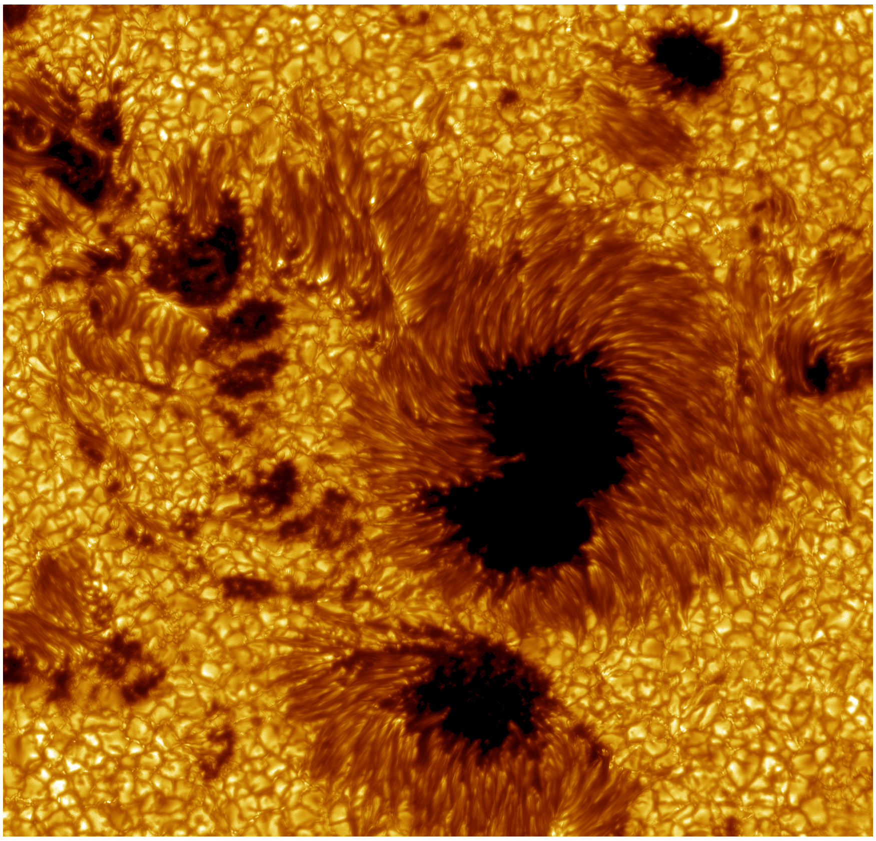

Figure 1.2: High-resolution picture recorded with the Swedish 1-m solar telescope on La Palma, showing a dark sunspot (active region 10030) and surrounding granules. (online source: www.solarphysics.kva.se).

of convective cells rising from the interior. Two or three characteristic cell sizes can be distinguished: granules are bright features of order of hundreds to a thousand km across, with lifetimes of about 10 minutes, surrounded by dark edges, representing the down flow of convection cells; supergranules are of order of 30,000 km across, with lifetimes of 12 to 24 hours. However, over small fractions of the solar surface, the granulation is replaced by sunspots (Fig. 1.2) usually surrounded by a filamentary penumbra. They are regions where strong magnetic field is concentrated (Hale 1908, Zeeman and Winawer 1910). Sunspots are formed when magnetic flux tubes just below the Sun's surface are compressed by the subsurface plasma pressure and poke through the solar photosphere. They are somewhat cooler (4,000 K) than the average surface (6,000K), and so they appear darker by comparison. Furthermore, it is observed that sunspots often come in pairs, with opposite magnetic field polarity. The boundaries of supergranules contain a concentration of magnetic fields, swept there by horizontal motions in the supergranule cells. This concentration of magnetic fields gives rise to the chromospheric network in the layer above the photosphere (Benz 2002). Inspite of its small altitude, the photosphere has been a major source of information about the Sun. The magnetic field can be accurately measured and mapped by observing the Zeeman effect. The photosphere comprises the footpoints of the field lines extending into the regions above.

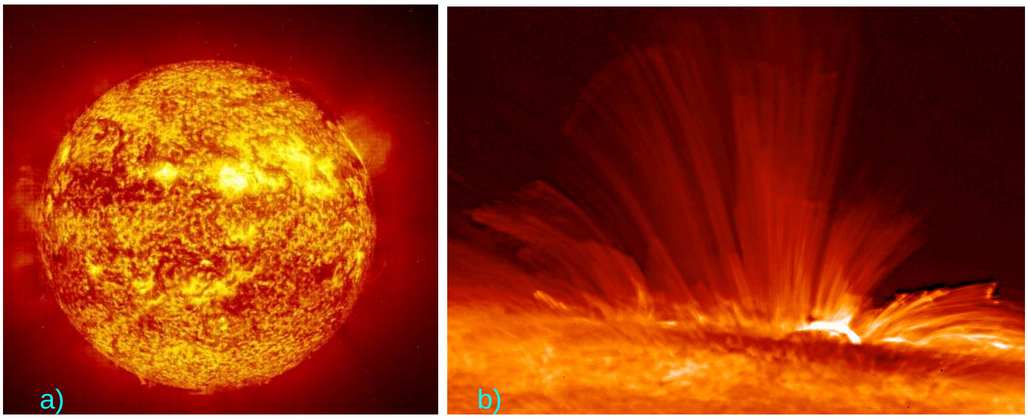

Figure 1.3: a) Picture of the chromosphere which is taken at the same yellow wavelength of light emitted by helium atoms; b) the image of the solar 'chromosphere' which was obtained on on 20 November 2006 by the Hinode solar observatory, and reveals the structure of the solar magnetic field rising vertically from a sunspot, outward into the solar atmosphere. (Credits: Hinode JAXA/NASA/PPARC.)

1.1.2 Chromosphere

The chromosphere is an irregular layer above the photosphere where the temperature rises from 4200°C to about $10,000°$ C (Priest 1982a). At these higher temperatures hydrogen emits light that gives off a reddish color (H-alpha emission). This colourful emission can be seen in prominences that project above the limb of the sun during total solar eclipses. This is what gives the chromosphere its name (color-sphere). The chromosphere is very faint because the atmosphere becomes transparent (optically thin) in the continuum spectrum. At the start of an eclipse one can see light that has originally come up from the photosphere and is then scattered towards earth at the chromospheric level as well as the intrinsic photospheric emission. The gas has a density of around $10^{11} cm^{-3}$ and is almost transparent to visible radiation, but opaque in some atomic transition lines. Because of the importance of outward temperature increase, especially for Ca II emission, a more precise definition of the chromosphere is used frequently: the layer between the temperature minimum and the level where $T = 25,000K$. In the one-dimensional model, this layer comprises some $2000km$. On the other hand the spicules, which also have a chromospheric temperature, cover a range of $\approx 5000km$ when observed at the limb (Stix 2002).

The magnetic field in the chromosphere connects the coronal magnetic structures with their photospheric footpoints, i.e. it forms the transition from the photospheric flux tubes to the coronal loops and open field lines. This transition is far from trivial, involving magnetic canopies, cool and hot loops and strongly bent field lines (Solanki 2004b). The most prominent chromospheric features are filaments, prominences, the chromospheric network associated with the boundaries of super-granular cells. Filaments and prominences are the same phenomena seen from different perspectives and with different background. Filaments are seen against the bright disk in absorption whereas prominences are seen above the limb against dark space in emission of scattered light from the surface.

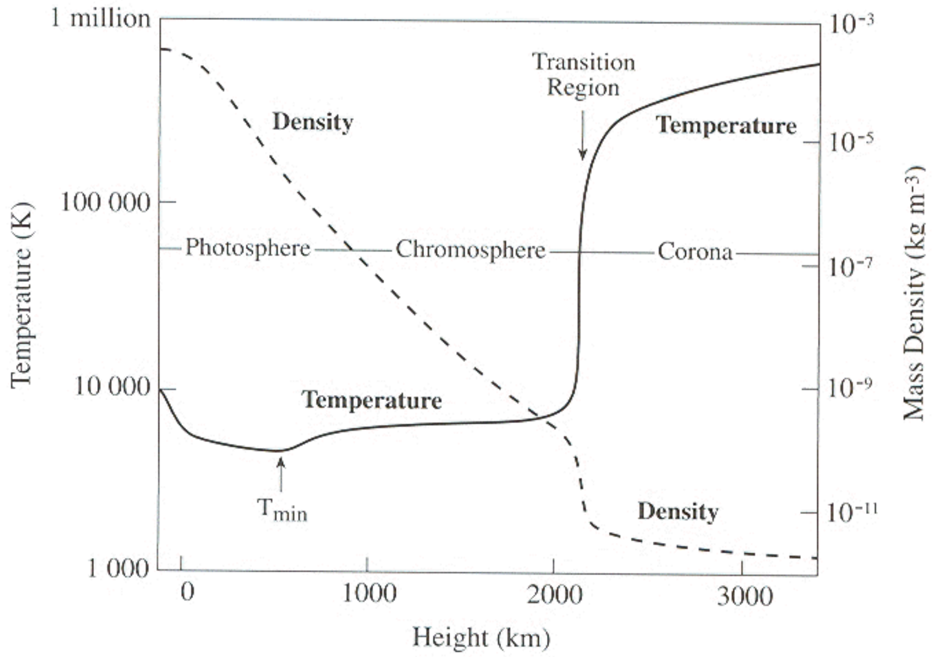

Figure 1.4: Temperature and density profile of the solar atmosphere. Adopted from Lang (2001).

1.1.3 Transition region

The transition region is a very thin layer of the Sun's atmosphere, just above the chromosphere, a relatively small regime of few hundred kilometers (about 500km). This region is locally visible by space telescopes in the UV (ultraviolet) range. Analyses of both solar ultraviolet and radio observations have shown the existence of a steep increase of temperature within transition region. This region is an important chromosphere-corona boundary over which the temperature rises drastically from 20,000 degrees Kelvin in the upper chromosphere to over 2 million degrees Kelvin in the corona (see Fig. 1.4). Other important changes also take place in this part of the atmosphere. As the temperature rises, the atmosphere changes from predominantly neutral with radiation from hydrogen and helium dominating the spectrum to highly ionized with radiation from the less abundant heaver ions dominating (Mariska 1993). The magnetic field also changes here from being controlled by the denser photospheric gas to controlling the structure of the corona. It is suspected that the complicated structure of the Sun's magnetic field may provide clues to the dramatic increase in temperature over such a small change in radius. Most of the transition region emission occurs in the VUV (vacuum ultraviolet) range of the electromagnetic radiation (Wilhelm et al. 2007). Thus, ultraviolet emission lines can provide ample information about the magnetic structures and plasma properties of the transition region.

1.1.4 Corona

The corona is the outermost part of the Sun's atmosphere. It can clearly be seen during the total solar eclipse as a bright region that extends more than some solar radii away from the disk of the sun (see Fig. 1.5). The corona is not always evenly distributed across the surface of the sun. During periods of quiet, the corona is more or less confined to the equatorial regions, with coronal holes covering the polar regions. However during the Sun's active periods, the corona is distributed over the equatorial and polar regions, though it is most prominent in areas with sunspot activity. The solar corona is structured by the coronal magnetic field which is rooted at the solar surface and is partially open to the heliosphere. Its magnetic fields have generally very complex structure depending on the solar activity cycle. Often, however, they take shapes of arcades and loops emerging from the photosphere, penetrating through the coronal medium and sinking into the photosphere again. Observational data indicate large spatial scales of such magnetic structures and their stationarity over comparatively long time intervals. The outer boundary of the corona is not precisely defined. Its outer boundary may be placed at a distance of $\sim 2-3R_{\odot}$ above the solar surface where the magnetic field lines are dragged out by the solar wind and bent into radial direction. There are two different magnetic zones in the solar corona that have fundamentally different properties: open-field and closed-field regions. Open-field regions connect the solar surface with the interplanetary field and are the source of the fast solar wind (Schwenn and Marsch 1990). A consequence of the open-field configuration is efficient plasma transport out into the heliosphere, whenever chromospheric plasma is heated at the footpoints. Closed-field regions, in contrast, contain mostly closed field lines in the corona up to heights of about one solar radius, which open up at higher altitudes and connect eventually to the heliosphere, but produce a slow solar wind component. It is the closed-field regions that contain all the bright and overdense coronal loops, filled with chromospheric plasma that stays trapped on these closed field lines (Aschwanden 2005). The corona displays a variety of features including streamers, plumes, and loops. These features change continuously with the variation of the surface field configuration and the overall shape of the corona changes with the sunspot cycle. Figure 1.5 shows an ground-based observation of the corona taken during the eclipse in 2008. Helmet streamers, large cap-like coronal structures with long pointed peaks into the heliospheric space, are formed by a network of magnetic loops above the solar surface. Polar plumes, associated with the open magnetic field lines at the Sun's surface, are long thin streamers that project outward from the Sun's north and south poles at solar minimum activity.

1.2 Magnetic field of the solar corona

One of the most fascinating characteristics of the Sun is its magnetic field. Although the solar magnetic field is not special among stars (neither especially strong nor especially fast evolving), the proximity of the Earth to the Sun allows to analyse this magnetic field with high spatial and temporal resolution, as well as in different solar layers. According to the present knowledge, the magnetic field of the sun is generated by hydromagnetic dynamo processes (Ossendrijver 2003) in the presence of differential rotation, turbulent convection, and meridional flows. The most likely location for the intensification of the

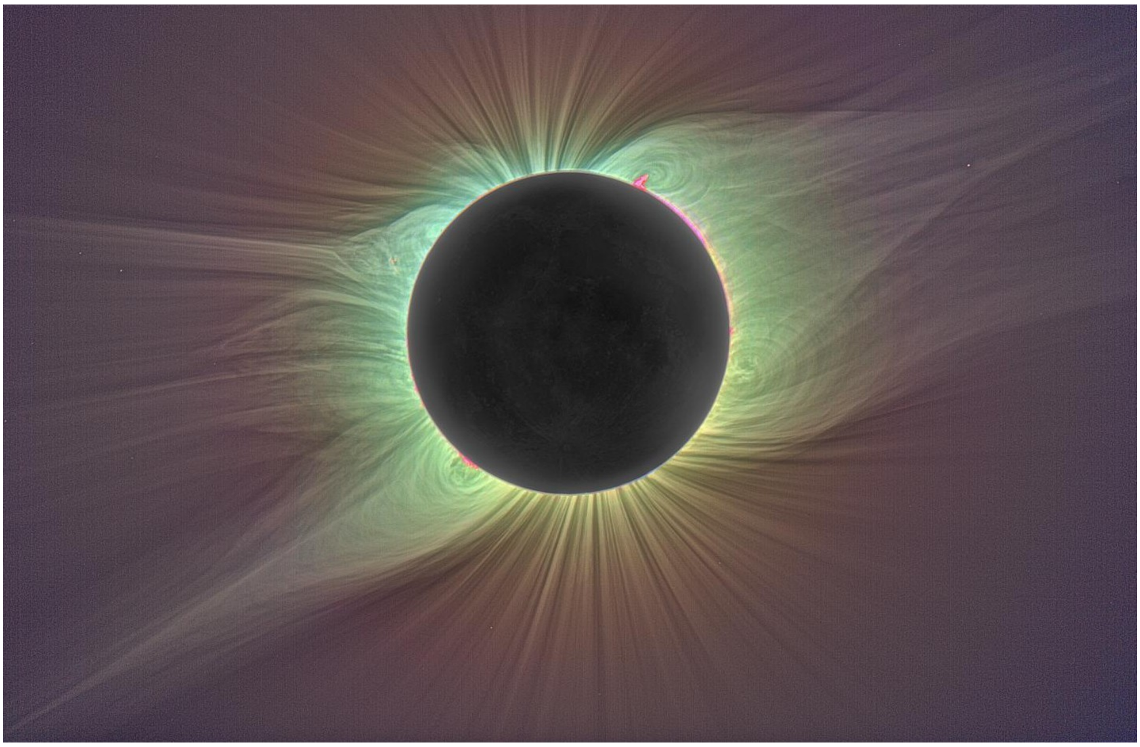

Figure 1.5: Image of the solar corona taken during the 2008 total eclipse . The brush-like strokes in the corona are aligned with the sun's magnetic field, similar to iron filings around a magnet. Photo: Miloslav Druckmüller, Peter Aniol and Vojtech Rusin.

large-scale azimuthal magnetic field is the tachocline region at the bottom of the convection zone, where there is a strong radial and azimuthal differential rotation (Thompson et al. 2003). From there, the solar magnetic field rises to the solar surface, expands from there to the corona in magnetic loops and swept away by the solar wind, filling the interplanetary medium until meeting with the interstellar medium. On its way from the interior to far outside, the solar magnetic field affects all matter which it encounters either by just perturbing it or even by confining it and governing its dynamics. At the solar surface and below, the magnetic field modifies the normal gas flow, the convection pattern, the travelling of waves, and more, gives rise to so-called "active phenomena" as sunspots, plages, etc. The plasma in the solar corona is dominated by the magnetic field in the sense that the magnetic energy density is orders of magnitude greater than the thermal, kinetic and gravitational energy density (Gary 2001). Hence the Lorentz force affects the charged particles of the corona plasma consisting electrons and ions, which are guided in a spiraling gyromotion along the magnetic field lines. The critical parameter plasma-β which is the ratio of the thermal pressure p_{th} to the magnetic pressure p_{mag} is:

$$\beta = \frac{p_{\mathrm{th}}}{p_{\mathrm{mag}}} = \frac{2n_e \kappa_B T_e}{B^2/8\pi} \tag{1.1}$$

where κ_B the Boltzmann constant, B the magnetic field strength, n_e the electron density and T_e the electron temperature. In the corona a plasma-β parameter is very much less

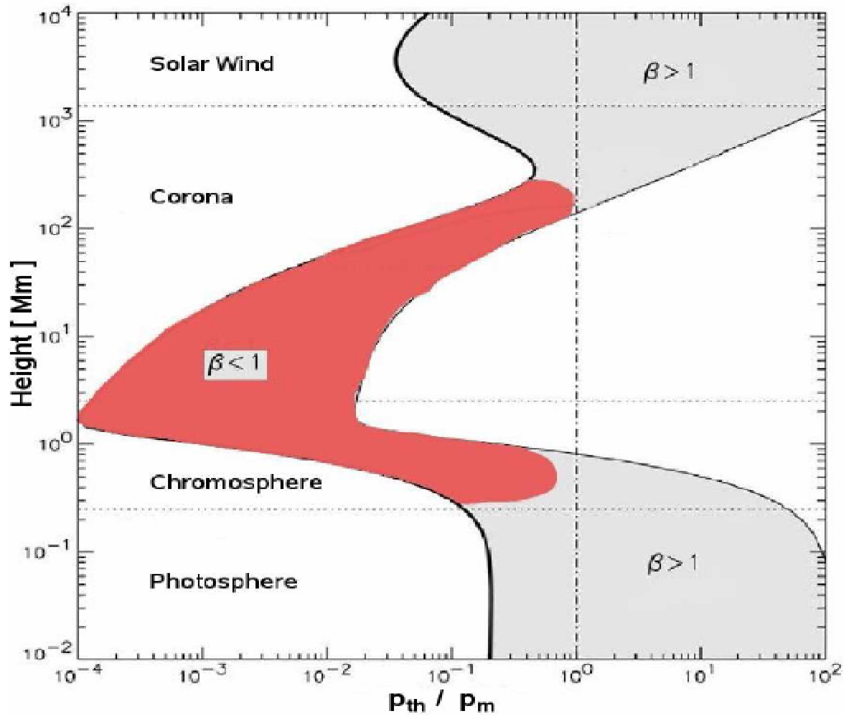

Figure 1.6: Plasma-β as a function of height in the solar atmosphere. Outlined in red is the region in the chromosphere and the corona where magnetic field is dominant over non-magnetic forces. Horizontal dashed lines outline the approximate vertical extension of the atmospheric layers. (Courtesy of G. A. Gary.)

than unity (see Fig. 1.6). Therefore it is the magnetic field in the corona which dictates the plasma motion. If the changes of the coronal structures take place on length scales comparable to the typical coronal scale height ($\gtrsim$50 000 km, as a consequence of the high coronal temperature and light hydrogen gas; see Aschwanden 2005), one can assume the electric currents to be co-aligned with the magnetic field. Thus, the Lorentz force vanishes and the magnetic field is said to be in a "force-free" state, which we will illustrate using basic MHD equations in section 1.4. Then the coronal magnetic field can be considered to evolve slowly through a sequence of neighbouring force-free equilibria, which, however, is not the case during an eruption. In the next subsection we will discuss some effects of the magnetic fields influence in the solar corona and the techniques that have been used to measure the magnetic field of the Sun at the photospheric level.

1.2.1 Phenomenological examples of the dominant role of corona magnetic field

The magnetic field in the solar corona is generally believed to be a necessary ingredient for a wide range of phenomena from being the carrier of MHD waves (through the plasma) to heat the corona, to produce the gyro-synchrotron radiation in the radio wavelength range. The structure and evolution of the magnetic field (and the associated electric currents) that permeates the solar atmosphere plays key roles in a variety of dynamical processes observed to occur on the Sun. Such processes range from the appearance of extreme ultraviolet (EUV) and X-ray bright points, to brightenings associated with nanoflare events, to the confinement and redistribution of coronal loop plasma, to reconnection events, to X-ray flares, to the onset and liftoff of the largest mass ejections. It is believed that many of these observed phenomena take place on different morphologies depending on the configurations of the magnetic field, and thus knowledge of such field configurations is becoming an increasingly important factor in discriminating between different classes of events. In the next two subsections we discuss two phenomenological examples such as coronal loops and filaments to illustrate the dominant role of magnetic field in the solar corona.

1.2.1.1 Corona loops

Coronal loops are a phenomenon of active regions and there is growing evidence that they are in fact the dominant structures in the higher levels (inner corona) of the Sun's atmosphere. They are visible at X-ray, ultraviolet, and white-light wavelengths, consisting of an arch, extending upward from the photosphere for tens or hundreds of thousands of kilometers. They form the basic structure of the lower corona and transition region of the Sun. These highly structured and elegant loops are a direct consequence of the solar magnetic flux tubes within the solar interior. They owe their high luminosity and variety to their nature of magnetic flux tubes where the plasma is confined and isolated from the surroundings. They are magnetic flux tubes threading through the solar interior, thrusting up into the solar atmosphere (see Fig. 1.7). They are nothing other than conduits filled with heated plasma shaped by the geometry of the coronal magnetic field (Aschwanden 2005). The population of coronal loops can be directly linked with the solar cycle. Coronal loops are ideal structures to observe when trying to understand the transfer of energy from the solar interior, through the transition region and into the corona. Many scales of coronal loops exist, neighbouring open flux tubes that give way to the solar wind and reach far into the corona and heliosphere. Anchored in the photosphere (with two footpoints of opposite polarity, see Fig. 1.7.a), coronal loops penetrate the chromosphere and transition region, extending high into the corona. Magnetized and fully-ionized plasma conducts thermal energy mostly along the magnetic field lines. Observations show that coronal loops have a wide variety of temperatures along their lengths. Loops existing at temperatures between 10^5K and 1MK are generally known as cool loops (Brekke et al. 1997). Warm loops are well observed by EUV imagers such as SoHO/EIT[1] and TRACE[2], and confine plasma at temperature around 1 - 1.5 MK (Lenz et al. 1999). Hot loops are those typically observed in the X-ray band and hot UV lines (e.g., Fe xvi), with temperatures around or above 2 MK (Bray et al. 1991). Naturally these different categories radiate at different EUV wavelengths.

1.2.1.2 Filaments

Filaments are dark, thread-like features (see Fig. 1.8.a) seen in the red light of hydrogen (H-alpha). These are dense, somewhat cooler than the surroundings, clouds of material

[1]Solar and Heliospheric Observatory /Extreme ultraviolet Imaging Telescope
[2]Transition Region and Coronal Explorer

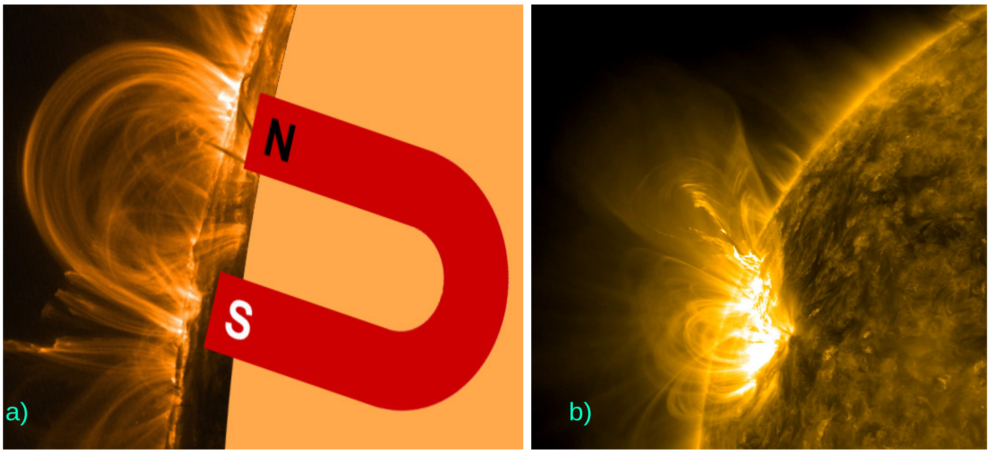

Figure 1.7: a). The image of coronal loops over the eastern limb of the Sun which was taken in the TRACE 171Å pass band, characteristic of plasma at 1 MK, on November 6, 1999. (Windows to the Universe original artwork by Randy Russell using an image from NASA's TRACE). b). The image taken by SDO's AIA instrument in the 171 Å wavelength of extreme ultraviolet light for coronal loops of the July 9th, 2010. Credit: SDO satellite / NASA.

that are suspended above the solar surface by loops of coronal magnetic field against gravity. A prominence is a large, bright feature extending outward from the Sun's surface, often in a loop shape. When a prominence is viewed from a different perspective so that it is against the sun instead of against space, it appears darker than the surrounding background, which is known as a solar filament. They form over a wide range of latitudes on the Sun. Their locations spread everywhere, from the active belt to the polar crown. Poleward transport of magnetic flux across the solar surface during the solar cycle is accompanied by a poleward migration of the preferred locations of filament formation (Minarovjech et al. 1998, Ambrož and Schroll 2002). They are cooler and darker because thermal conduction across a field line is negligible compared to thermal conduction along a field line, where the magnetic fields also insulate the cool filament material ($T \sim 10,000$K) from the surrounding hot corona ($T_c > 10,000$K) (Sankarasubramanian et al. 2005). Although solar filaments may form at many locations on the Sun, they always form above Polarity Inversion Lines (PIL) which divide regions of positive and negative flux (i.e. locations where $B_z = 0$ and the field is mainly horizontal). However, the existence of a PIL is not a sufficient condition for a filament to form (Benz 2002, Bhatnagar and Livingston 2005). Magnetic diagnostics of solar filaments in the chromosphere are crucial for our understanding of their formation, maintenance, and final eruption. However, due to the intrinsically weak chromospheric magnetic field (Solanki et al. 2006), direct spectropolarimetric measurements of magnetic field vectors in filaments had been extremely rare, difficult, and unreliable for a long time. Filaments last for a few weeks or months. The gas in a filament will eventually move to a different layer in the Sun and will no longer be visible in an image of the chromosphere. But at the same time, other

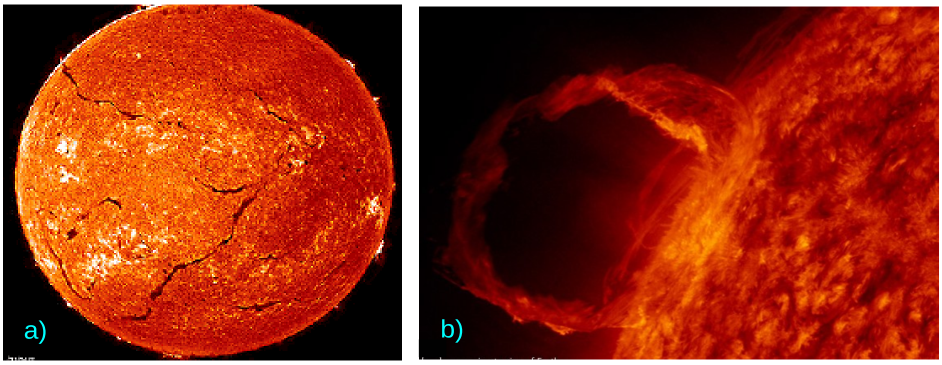

Figure 1.8: a). Hα image showing filaments on the Sun. b). image of solar prominance taken by SDO's AIA instrument on the March 30, 2010. Credit: SDO satellite / NASA.

gas may move into the chromosphere and create a new filament someplace else. The birth and death of filaments is a mystery and the subject of ongoing study by solar scientists.

1.2.2 Measurements

The magnetic field has had a unifying role in solar physics, bringing order to the chaos of solar events and phenomena. The reason is that solar activity is an electromagnetic phenomenon caused by the ordered interplay between solar rotation, convective motions and magnetic fields. As a matter of fact, to understand those activities in the solar atmosphere, one has to know more about the magnetic field of the solar corona. One way to achieve this would be to measure the magnetic field (Hagyard 1985, Stenflo 1978). Spectro-polarimetric measurement allows to deduce the magnetic field strength and its orientation by means of the Zeeman effect and the Hanle effect. The spectral-line polarization has to be recorded and interpreted using the theory of radiative transfer of the Stokes vector in a magnetized plasma. Such remote measurements are restricted by the requirement to observe more or less indirect effect of magnetic field vector $\boldsymbol{B}$ on the electromagnetic radiation and by various limits in the resolution and span in coordinate space. There are different ways of magnetic field determination on the Sun, which can be divided into two groups (Beckers 1971). The first utilizes the influences of the magnetic field on the solar electromagnetic radiation. It includes measurements made by means of the Zeeman effect, Hanle effect (or resonance scattering), the gyro-resonance radiation and synchrotron radiation in the radio region, and the Faraday rotation of radio waves. The second group makes use of the influence of magnetic field on the temperature and density structure of the solar atmosphere. In the following, Zeeman and Hanle effects will be discussed along with the inversion techniques and resolving 180° ambiguity.

1.2.2.1 Zeeman effect

It is well known that electronic states of atom are characterized by a unique set of discrete energy levels. When excited through photon absorption or collision, the electron state makes transitions between these quantized energy levels. The emitted light forms a discrete spectrum, reflecting the quantized nature of the energy states or energy levels. In the presence of a magnetic field, these energy levels can shift (Herzberg 1950). This effect is known as the Zeeman effect. The effect is the splitting of spectral lines into several components in the presence of an external magnetic field. It was first recorded by Pieter Zeeman in 1896. An early attempt to explain the the origin of Zeeman effect was given by Lorentz in term of the classical Larmor's precession theory. The quantum mechanical approach offers a more adequate and general explanation of the Zeeman effect. The splitting of spectral lines into several components is due to a change in energy levels of the electrons involved in the quantum transitions. In the presence of a magnetic field each level with the magnetic quantum number M_J gets additional energy

$$E_B = gM_J\hbar\frac{eB}{2m_e} = g\hbar\omega_L \tag{1.2}$$

where e is the elementary charge, B is the magnetic field strength, m_e the mass of the electron, $\hbar$ the Planck constant, ω_L is the Larmour frequency, g is the Landé factor depending on the quantum numbers L, S, J, and M_J: L is for orbital angular momentum of the electrons, S is their spin quantum number, J is the associated total angular momentum quantum number, and M_J is the quantum number for the component of total angular momentum along the direction of the magnetic field (magnetic quantum number)(Stenflo 1978, Stix 2002). The Landé factor is

$$g = 1 + \frac{J(J+1) - L(L+1) + S(S+1)}{2J(J+1)} \tag{1.3}$$

Each level with total angular momentum J splits into $(2J+1)$ sublevels. As a result, the frequencies related to the transitions between the lower level with J_l and upper level with J_u are defined by

$$\nu_{J_lM_l\longleftrightarrow J_uM_u} = \nu_0 + \frac{eB}{2m_e}(g_uM_u - g_lM_l) \tag{1.4}$$

where ν_0 is the frequency of the line in the absence of magnetic field, g_u and g_l are the Landé factors for upper and lower levels respectively, and M_u and M_l are the magnetic quantum numbers for those levels.

The selection rules for allowed electric dipole transitions are:

$$\begin{aligned} &\Delta J = 0, \pm 1,\ J_u = 0 \rightarrow J_l = 0 \text{ is forbidden}, \\ &\Delta L = 0, \pm 1,\ \Delta S = 0, \\ &\Delta M = 0, \pm 1 \end{aligned} \tag{1.5}$$

The selection rule for magnetic dipole transition is $\Delta M = 0, \pm 1$. The lines 5303Å and 10747Å for Fe XIV and Fe XIII ions, are forbidden for the electric dipole transitions but allowed for the magnetic dipole transitions. When the spectral lines split into the three

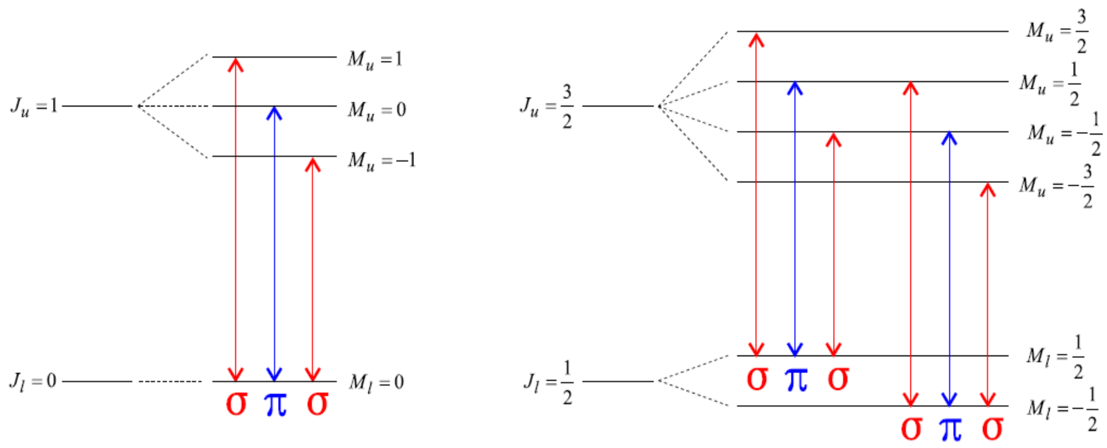

Figure 1.9: Zeeman transitions.

components, σ_b, σ_r, and π, the effect is known as normal Zeeman effect, which agrees with the classical theory of Lorentz. The π-components correspond to the transitions with $\Delta M = 0$, and σ-components with $\Delta M = \pm 1$. The case when spectral lines split into more than three components is known as anomalous Zeeman effect, depends on electron spin, and is purely quantum mechanical (Stix 2002) (see Fig. 1.9).

The degree of the splitting depends on the field strength. For weak magnetic field (*weak-field Zeeman effect*), which is not strong enough to produce energy changes comparable to the separation of the sublevels, the separation between the splitting line components is directly proportional to $g\lambda^2 B$, where B is the field strength, λ is the wavelength. It is the ratio of the splitting to the linewidth which determines the ability to detect small splitting effects and, consequently, the Zeeman effect is more significant when probed at longer wavelengths.

For a normal Zeeman triplet, the π-component can not be observed in a view direction for which the magnetic field is parallel to the line-of-sight (longitudinal Zeeman effect), and the two σ-components become right- and left-handed circularly polarized. Therefore, the longitudinal Zeeman effect has the great advantage that it allows circular polarization maps to be directly interpreted as maps of the line-of-sight component of the magnetic field strength. When the magnetic field is perpendicular to the line-of-sight, the intensity of the π-component equals the sum of the two σ-components. In emission, the π-component is linearly polarized with the electric vector parallel to the magnetic field, and in absorption it is perpendicular to the field. The σ-components are linearly polarized in the perpendicular direction with respect to the π-component (transversal Zeeman effect). When the magnetic field makes an arbitrary angle to the line-of-sight, the π and σ-components have elliptical and mutually orthogonal polarizations. Although these rules appear straightforward to apply, a correct interpretation generally requires the use of a theory of spectral line formation in magnetic fields, particularly in the case when the splitting does not exceed the linewidth. (Stenflo 1978, 1994). In the case of very strong magnetic fields (*strong-field Zeeman effect*), where the field is sufficiently strong to produce energy changes comparable with the separation of the sublevels, the line-splitting effect is no longer linearly proportional to the magnetic field (Condon and Shortley 1970). Then, line splitting can be large compared to the separation of the spin-orbit system so that the coupling between the orbital and spin angular momenta gets disrupted and the spectral line rearranges (which is referred to as the "Paschen-Back effect"). This is different from the weak-field Zeeman effect in which the magnetic field is not strong enough to disturb the orbit-spin interaction so that the total angular momentum is conserved. For strong-field Zeeman effect the external magnetic field overpowers the spin-orbit effect and decouples L and S so that they precess about B nearly independently; thus, the M_L and M_S are approximately conserved and the effect reduces to three lines, each of which is a closely spaced doublet. The impact of the strong-field Zeeman effect for field strengths found on the Sun is, in general, small compared to the weak-field Zeeman effect and is thus neglected.

1.2.2.2 Hanle effect

The Hanle effect is the modification of the polarization by a local magnetic field of scattered radiation, which provides a very sensitive tool for studying the distribution of weak magnetic fields on the Sun (Sahal-Brechot 1981, Leroy 1985). The change of the polarization depends on the magnetic field orientation (Fig. 1.10). The effect begins to have an influence on the polarization at fairly small field strengths of just a few gauss, with sensitivity to fields up to around 300 G (Ignace et al. 2004). Experiments to describe the polarization from resonance line scattering date primarily back to the first third of the 20th century (Mitchell and Zemansky 1934). The influence of a magnetic field on line polarization was explained first by a young physicist named Wilhelm Hanle. Hanle (1924) described the change of linear polarization by the magnetic field in semiclassical terms as arising from the precession of an atomic, damped, harmonic oscillator. From a quantum mechanical point of view, the effect is understood in terms of interferences that occur when the degeneracy of the magnetic sublevels in the excited state is partially lifted.

The Hanle effect is most sensitive when the magnetic splitting is comparable to the natural line width. For most atomic transitions this implies weak magnetic fields, so that the level splitting can be calculated in the Zeeman effect (ZE) regime (Shapiro et al. 2007). The well-known Zeeman effect and the Hanle effect are complementary because they respond to magnetic fields in very different parameter regimes. The Zeeman effect depends on the ratio between the Zeeman splitting and the thermal line width. The Hanle effect though depends on the ratio between the Zeeman splitting and the inverse life time of the atomic levels involved in the process of the formation of the polarized line. For the permitted UV lines, the Zeeman effect is of limited interest for the determination of the magnetic field in the quiet corona. This is because the ratio between the Zeeman splitting and the thermal width is small due to the weakness of the magnetic field and the high Doppler width in the hot coronal plasma. On the contrary, the measurement and physical interpretation of the scattering polarization of the UV lines are a very efficient diagnostic tool for determining the coronal magnetic field through its Hanle effect (Derouich et al. 2010, Trujillo Bueno 2001).

Although the Hanle effect opens new diagnostic possibilities that are not available with the Zeeman effect, it has the disadvantage that it does not lead itself to direct mapping of

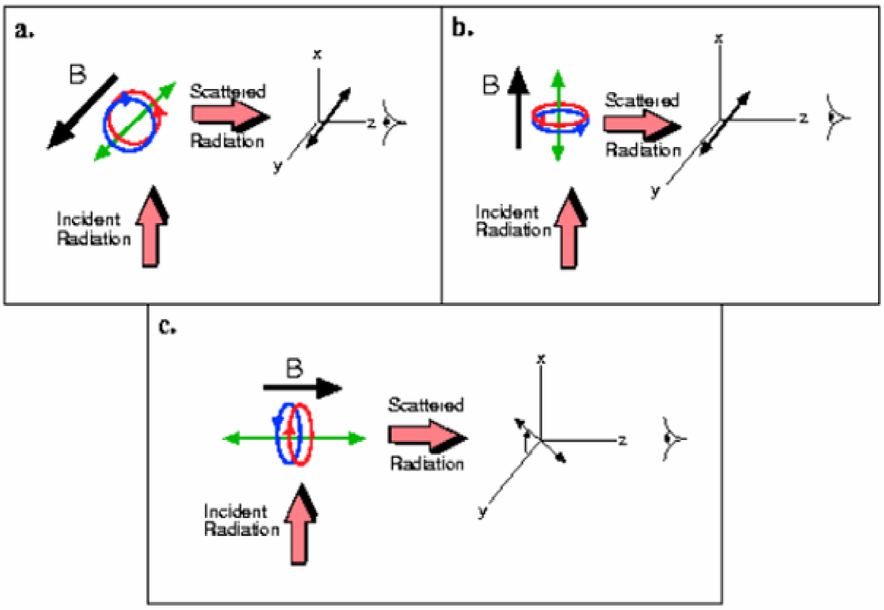

Figure 1.10: Hanle effect in scattering.

the magnetic field but instead constrains the field properties in more convolved ways. A fundamental reason for this is that the Hanle effect shows up in two observed parameters, Q and U[3], while the magnetic field vector needs three parameters to fully constrain its three vector components (Parker 2003). The field vector is therefore not uniquely constrained by Hanle observations alone, but needs some additional constraint, either from theory or other types of observations (e.g. from the longitudinal Zeeman effect in Stokes V[4]).

1.2.2.3 Inversion

Solar magnetic field leaves its fingerprint in the state of polarization of the emergent electromagnetic radiation. Zeeman-induced polarization in photospheric absorption lines contains most of the information necessary to recover the vector magnetic field. However, inference of the vector magnetic field from the polarization profiles of solar absorption lines is an inverse problem (Unno 1956, Skumanich and Lites 1987, Ruiz Cobo and del Toro Iniesta 1992). Typically, those problems are solved by linearizing an appropriate forward model, computing the sensitivities and then iteratively solving a regularized optimization problem. In this sense most of the inversion procedures for Stokes profiles are based on a non-linear least-squares minimization (Landolfi et al. 1984). The results of this inversion are, therefore, to some extent model-dependent and one can only expect to find a

[3] where Q describes the amount of linear polarization and U the amount of +45° or −45° polarization.
[4] V describes the amount of right- or left-handed circular polarization.

set of model parameters that are capable of reproducing the observations (Socas-Navarro 2001).

Four quantities are needed to fully describe the state of polarization of electromagnetic radiation. The Stokes four-dimensional vector $\mathbf{I} = [I, Q, U, V]$ is widely used to represent the state of polarized light, where I is total intensity. Conveniently, the components of $\mathbf{I}$ may be defined operationally in terms of intensities measured with ideal optical elements. The advantage of the Stokes vector is that it describes partial polarization of radiation from multiple incoherent sources of light. In order to compute synthetic Stokes profiles one has to solve the radiative transfer equation (RTE) for polarized light (Unno 1956). The RTE describes how energy (i.e. a polarized light beam) is transmitted through a medium where a magnetic field is present, taking into account how the magnetic field modifies the polarization state of the light. One of the simplest solutions of the radiative transfer equation for polarized radiation is the solution for an atmosphere under the Milne-Eddington (ME) approximation, which is based on the assumption that all the atmospheric and atomic parameters involved in the radiative transfer are constant along the line formation region and over the whole resolution element (except for the source function). This simplification yields an analytical solution to the RTE. An inversion code based on such an atmospheric model is applied to the data and gives a fast estimation of the magnetic field strength. However, such an assumption is far from being verified for most solar observations: in all those cases when the magnetic field is a function of optical depth, or of position within the observed area, or both, the deduced value represents a sort of ill-defined mean of the real values.

A basic inversion of the Stokes profiles yields the major vector properties of the mean field: its components in the line of sight ($B_{\rm LOS}$) and transverse ($B_{\rm trans}$) directions, and its inclination (γ) and azimuth (φ) angles. Sophisticated methods that perform least-squares fits of the Stokes profiles can extract more information. For instance, the response function technique of Ruiz Cobo and del Toro Iniesta (1992) can invert the profiles into a model solar atmosphere with stratified velocities, magnetic fields, and temperatures, without the need to rely on the analytical Milne-Eddington solution and therefore it is able to retrieve height dependent information within a reasonable time. This method is one of the most modern techniques used to invert Stokes profiles, but it is computer intensive due to the large number of profiles to fit and the large number of parameters involved in the fitting procedure.

1.2.2.4 Resolving 180° ambiguity

After decades of performing solar vector magnetography, a quantitative interpretation of the measurements is still hampered by the azimuthal ambiguity inherent in the transverse $B_{\rm trans}$ (perpendicular to the line of sight) magnetic field component. While the Zeeman effect reliably yields the magnetic field vector in the active region solar photosphere or chromosphere, its symmetric properties allow a 180° difference between two equally likely values of the azimuth angle γ or $\gamma + 180°$ for the transverse magnetic field. Therefore, one cannot easily tell which direction is correct. This ambiguity is attributed to the fact that the polarization signal due to the transverse field component provides only the plane of linear polarization. Using the linear polarization of magnetically sensitive spectral lines to determine the field perpendicular to the line-of-sight results in an ambiguity of 180°

in its direction (Harvey 1969). The resolution of this 180°-ambiguity or, equivalently, the *azimuth disambiguation* of the measured magnetic field vector needs to be performed self-consistently over the observational field of view to eliminate bogus magnetic field discontinuities and subsequent artificial electric currents before the vector magnetic field can be fully determined.

There is no known method for resolving the ambiguity through direct observation using the Zeeman effect, at least for the single-height observations that are the most popular and well-understood approach for inferring the solar magnetic field. Hence, to resolve the ambiguity, some further assumption on the nature of the solar magnetic field must be made (Leka et al. 2009). Many algorithms are presently in use for resolving the ambiguity in vector magnetic field observations. These methods typically fall into one of two categories: comparison to a reference field (e.g., Cuperman et al. 1992, Moon et al. 2003, Li et al. 2007), or minimization of some property of the field, typically related to the forces or currents present (e.g., Canfield et al. 1993, Metcalf 1994, Gary and Demoulin 1995, Georgoulis 2005). In all cases, an assumption or approximation must be made which may not be valid for solar photospheric or chromospheric fields. However, Crouch and Barnes (2008) demonstrated that the azimuthal ambiguity that is present in solar vector magnetogram data can be resolved with line-of-sight and horizontal heliographic derivative information by using the divergence-free property of magnetic fields without additional assumptions. They discussed the specific derivative information that is sufficient to resolve the ambiguity away from disk centre, with particular emphasis on the line-of-sight derivative of the various components of the magnetic field. Conversely, they also showed cases where ambiguity resolution fails because sufficient line-of-sight derivative information is not available.

In the following, we describe some methods that have been used to solve the 180° ambiguity problem in the transverse fields.

✪ Acute angle method

In this method, the directions of transverse field, $\boldsymbol{B}^{\rm obs}_{\rm trans}$, are determined by comparing them with the transverse field directions of an equivalent potential field, $\boldsymbol{B}^{\rm pot}_{\rm trans}$, which is matched to the observed line-of-sight field strength at the surface. Although some areas of the solar atmosphere where vector magnetic field measurements are made are clearly not force-free, let alone current-free, it is often useful to consider a potential, or linear force-free, extrapolation of the magnetic field as a reference for comparison to the observations. The simplest approach is to use the observed, ambiguity-free longitudinal or line-of-sight component of the magnetic field B_l as a boundary condition to calculate the potential field using the Green's function method (Chiu and Hilton 1977). Acute Angle Methods resolve the 180° ambiguity by comparing the observed field to an extrapolated model field. The azimuth is thus resolved by requiring that some component (i.e., image-plane transverse, or heliographic-plane horizontal) of the observed field and the extrapolated field make an acute angle, i.e., $-90° \leq \Delta\theta \leq 90°$, where $\Delta\theta = \theta_{\rm obs} - \theta_{\rm extrapol}$ is the angle between the observed and extrapolated components. This condition may also be expressed as $\boldsymbol{B}^{\rm obs}_{\rm trans} \cdot \boldsymbol{B}^{\rm pot}_{\rm trans} > 0$, where $\boldsymbol{B}^{\rm obs}_{\rm trans}$ is the transverse or horizontal component of the observed field, and $\boldsymbol{B}^{\rm pot}_{\rm trans}$ is the transverse or horizontal component of the extrapolated potential field (see Metcalf et al. 2006, for more details).

✪ Magnetic Field Pressure Gradient

Implemented by Cuperman et al. (1993), this analytic method uses the condition that the magnetic field is nonlinear force-free. Under this assumption, magnetic fields are proportional or parallel to the electric current density, where the steady state equations describing force-free magnetic field configurations are: $\nabla \times \boldsymbol{B} = \alpha \boldsymbol{B}$. Multiplying the this equation with $\boldsymbol{B}$ vectorially, one can obtain

$$\boldsymbol{B} \times (\nabla \times \boldsymbol{B}) = \frac{1}{2}\nabla B^2 - (\boldsymbol{B} \cdot \nabla)\boldsymbol{B}$$

Because the left side of the equation is null, the equation leads to

$$\frac{1}{2}\nabla B^2 = (\boldsymbol{B} \cdot \nabla)\boldsymbol{B}$$

In Cartesian coordinate, the z-component of the above equation is

$$\frac{1}{2}\frac{\partial}{\partial z}B^2 = \Big(B_x\frac{\partial}{\partial x} + B_y\frac{\partial}{\partial y} + B_z\frac{\partial}{\partial z}\Big)B_z$$

Combining the above equation with the magnetic field divergence-free condition, $\nabla \cdot \boldsymbol{B}$, one obtains

$$\frac{1}{2}\frac{\partial}{\partial z}B^2 = \Big(B_x\frac{\partial B_z}{\partial x} + B_y\frac{\partial B_z}{\partial y}\Big) - B_z\Big(\frac{\partial B_x}{\partial x} + \frac{\partial B_y}{\partial y}\Big) \tag{1.6}$$

where $B^2 = B_x^2 + B_y^2 + B_z^2$. Variables appearing on the right hand side of the equation (1.6) are three observable magnetic components in the photosphere, except for 180° ambiguous directions of B_x and B_y. A switch by 180° in (B_x, B_y) just changes the sign of the RHS of Eq. (1.6). We assume that the magnetic pressure decreases with vertical direction perpendicular to the solar surface, i.e., the magnetic pressure gradient is negative:

$$\frac{\partial}{\partial z}B^2 \leqq 0$$

which then determines the sign of (B_x, B_y) uniquely if the RHS of Eq. (1.6) is nonzero. The signs of $\boldsymbol{B}_{\rm trans}^{\rm obs}$ are determined to satisfy the above equation at each pixel with three observable magnetic field components in the photosphere (see Li et al. 2007, Metcalf et al. 2006, for more details). At disk center, the vertical field and the magnitude of the horizontal components of the field are measured, and the two choices for the direction of the horizontal component give equal magnitude but oppositely signed results for the vertical derivative of the magnetic pressure. Away from disk center, the observed line-of-sight and transverse fields can be transformed into heliographic coordinates for either choice of the ambiguity resolution, and Equation (1.6) still holds. In either case, the ambiguity is resolved, with no iteration, by evaluating $\partial B^2/\partial z$ for an initial choice of the direction of the transverse field. The direction of the transverse field is reversed at each pixel if $\partial B^2/\partial z > 0$ at that point.

✪ **Minimum energy method**

Implemented by T. Metcalf (Metcalf 1994, Metcalf et al. 2006), this method simultaneously minimizes both the electric current density, $\boldsymbol{J}$, and the magnetic field divergence, $\nabla \cdot \boldsymbol{B}$. Unfortunately, one can not compute the divergence exactly since the height dependence of the vertical magnetic field is unknown. However, the divergence condition is still useful, since one can drive an approximate height derivative of B_z from potential (or force-free) field computed from the observed line-of-sight field. Minimizing $|\nabla \cdot \boldsymbol{B}|$ gives a physically meaningful solution and minimizing $\boldsymbol{J}$ provides a smoothness constraint. For a force-free field, the magnetic free energy is bounded above by a value proportional to the maximum value of J^2/B^2 as shown by Aly (1988). Since B^2 is unambiguous, by minimizing J^2 we are minimizing the upper bound on the magnetic free energy. The functional to be minimized is

$$E = \sum_{pixels} \left(|\nabla \cdot \boldsymbol{B}| + |\boldsymbol{J}|\right)^2$$

The calculation of the vertical electric current density, J_z, is straightforward, requiring only observed quantities in the computation and a choice of the ambiguity resolution. However, calculation of $\nabla \cdot \boldsymbol{B}$ and the horizontal current, J_x and J_y, requires a knowledge of the vertical derivatives of the magnetic field. Variations of the magnetic field with height are not normally known, so the vertical derivatives of the field are approximated from a linear force-free field (LFFF) extrapolation using the unambiguous line-of-sight field as the lower boundary condition.

✪ **The nonpotential magnetic field calculation method**

Implemented by M. Georgoulis (Georgoulis 2005), this method assumes that an isolated, current-carrying, solar magnetic structure $\boldsymbol{B}$ is measured on a plane S by means of a longitudinal field B_l, a transverse field B_{trans}, and an azimuth angle ϕ of the transverse field on the line-of-sight reference system. Then the two equally likely ambiguity solutions in this coordinate frame are $[B_l, B_{\text{trans}}, \phi]$ and $[B_l, B_{\text{trans}}, \pi + \phi]$. Then transforming these two solutions to the local, heliographic, reference system to obtain the two heliographic ambiguity solutions $\boldsymbol{B}_1$ and $\boldsymbol{B}_2$, respectively. The disambiguation then corresponds to finding the correct spatial combination of $\boldsymbol{B}_1$ and $\boldsymbol{B}_2$ that provides $\boldsymbol{B}$ over the observational field of view. Georgoulis (2005) decomposed the magnetic field vector $\boldsymbol{B}$ into a current-free, vacuum, magnetic field component $\boldsymbol{B}_p$ and a nonpotential, current-carrying, magnetic field component $\boldsymbol{B}_c$; i.e., $\boldsymbol{B} = \boldsymbol{B}_p + \boldsymbol{B}_c$. The solenoidal condition ensures that all terms in this equation are divergence-free for a closed, flux-balanced, magnetic configuration on S. Moreover, $\boldsymbol{B}$ and $\boldsymbol{B}_p$ share the same boundary condition for the normal (local vertical) magnetic field component B_z on S; i.e., $B_z|_S = B_{pz}|_S$ then the nonpotential magnetic field component $\boldsymbol{B}_c$ follows from

$$\nabla \cdot \boldsymbol{B}_c = 0; \quad \boldsymbol{B}_c \cdot \hat{z}|_S = 0 \quad \text{and} \quad (\nabla \times \boldsymbol{B}_c) \cdot \hat{z}|_S = J_z \tag{1.7}$$

These conditions still leave the horizontal divergence $\nabla_S \cdot \boldsymbol{B}_c = \partial B_{cx}/\partial x + \partial B_{cy}/\partial y$ undetermined. The assumption $\partial B_{cz}/\partial z = 0$ enforces $\nabla_S \cdot \boldsymbol{B}_c = 0$ which freely determines $(B_x, B_y)|_S$ upto a 2D Laplacian. The nonpotential component $\boldsymbol{B}_c$ is responsible for any electric currents present since $\boldsymbol{B}_p$ is current-free. From these conditions, and the further assumption that $\partial B_{cz}/\partial z$ vanishes on the boundary S, the nonpotential field $\boldsymbol{B}_c$ becomes analytically determined on S in terms of the vertical electric current density by

$$\boldsymbol{B}_c = \mathscr{F}^{-1}\Big[\frac{ik_y}{k_x^2 + k_y^2}\mathscr{F}(j_z)\Big]\hat{\mathbf{x}} + \mathscr{F}^{-1}\Big[\frac{-ik_x}{k_x^2 + k_y^2}\mathscr{F}(j_z)\Big]\hat{\mathbf{y}} + \nabla_S \phi \tag{1.8}$$

where $\mathscr{F}(r)$ and $\mathscr{F}^{-1}(r)$ are the direct and inverse Fourier transforms of r, respectively, and $j_z = 1/4\pi J_z$ with the condition $\Delta_S \phi = 0$ in 2D. However, the disambiguated J_z is not known a priori. If J_z was known, then the disambiguation would be performed numerically, but self-consistently, as follows: First, $\boldsymbol{B}_c$ can be calculated from equation (1.8). Then a distribution of the vertical magnetic field B_z can be found as a combination of B_{z1} and B_{z2} of the two ambiguity solutions $\boldsymbol{B}_1$ and $\boldsymbol{B}_2$, respectively. This B_z distribution gives rise to a potential field $\boldsymbol{B}_p$ such that $\boldsymbol{B}_p + \boldsymbol{B}_c$ best matches the respective combination of $\boldsymbol{B}_1$ and $\boldsymbol{B}_2$. Inferring B_z for a known J_z would be sufficient to resolve the π-ambiguity. Since J_z is unknown, Georgoulis (2005) follows a common strategy among disambiguation techniques which pursue a minimum magnitude for J_z. This can be performed by used an ambiguity-free proxy of J_z derived by extracting from the longitudinal magnetic field B_l any information on the heliographic horizontal field present in B_l due to projection effects. Specifically, the average of the two possible heliographic ambiguity solutions, $\boldsymbol{B}_{\mathrm{av}} = (1/2)(\boldsymbol{B}_1 + \boldsymbol{B}_2)$. Then, a proxy for vertical current density J'_{z_p} is constructed by applying Ampère's law to $\boldsymbol{B}_{\mathrm{av}}$. The calculation of J'_{z_p} is done once, at the beginning of the iterative process for B_z, and the resulting nonpotential field $\boldsymbol{B}_c$ is fixed and used in each iteration. The magnitude of J'_{z_p} depends on the observing angle to the active region, since the extent of the projection effects on B_l depends on the location of the measurements. On or close to disk center, $J'_{z_p} \simeq 0$, so the resulting $\boldsymbol{B}_c \simeq 0$. In this case, the NPFC method degenerates to a simple potential field acute angle method.

For more methods on 180° ambiguity removal and comparison among each other one can see Metcalf et al. (2006).

1.3 Force-free assumptions in the solar corona

Magnetic fields can induce currents in a moving conductive fluid, which create forces on the fluid, and also change the magnetic field itself. The ideal MHD (magnetohydrodynamics) equations describe the motion of a perfectly conducting fluid (i.e., plasma) interacting with the magnetic field (Alfven 1950, Priest 1982b, Sturrock 1994, Parker 1979, Jackson 1975). Such interaction is introduced through the equations involving the velocity $\mathbf{v}$ of the plasma fluid. Under conditions of electric neutrality, the equation of mass conservation and Newton's equation of motion for a plasma element, may be written as

$$\frac{\partial \rho}{\partial t} + \nabla \cdot (\rho \mathbf{v}) = 0 \tag{1.9}$$

$$\rho\Big(\frac{\partial \mathbf{v}}{\partial t} + \mathbf{v}\cdot\nabla\mathbf{v}\Big) = -\nabla p + \rho\boldsymbol{g} + \boldsymbol{J}\times\boldsymbol{B} + \boldsymbol{F}_{\text{visc}} \tag{1.10}$$

$$\frac{\partial \boldsymbol{B}}{\partial t} = \nabla\times(\boldsymbol{v}\times\boldsymbol{B}) \tag{1.11}$$

$$\nabla\cdot\boldsymbol{B} = 0 \tag{1.12}$$

where the plasma is subjected to a plasma pressure gradient ∇p, the Lorenz force $\boldsymbol{J}\times\boldsymbol{B}$ per unit volume and other forces like viscous force, $\boldsymbol{F}_{\text{visc}}$. Furthermore, ρ, $\boldsymbol{J}$, $\mathbf{g}$, and $\boldsymbol{B}$ stand for the plasma density, electric current density, gravitational acceleration, and magnetic field, respectively. Note that the energy equation and the equation of state for the plasma to close the system of equations are omitted here. In a plasma where the flow velocity is much smaller than both the isothermal sound and Alfven velocities, the equation of motion of the plasma (i.e., Eq. (1.10)) reduces to magnetohydrostatics (MHS) (Eq. (1.15)). Viscous forces are also negligible in the tenuous plasma of the corona. Along with Ampere's law in the limit of negligible electric fields, vanishing electron diffusivity, and together with assumption that the plasma is in equilibrium ($\partial_t = 0$, i.e. the temporal variations to be slow), the plasma of the solar atmosphere can be expressed by

$$\nabla\times\boldsymbol{B} = 4\pi\boldsymbol{J} \tag{1.13}$$

$$\nabla\cdot\boldsymbol{B} = 0 \tag{1.14}$$

$$\boldsymbol{J}\times\boldsymbol{B} - \nabla p + \rho\boldsymbol{g} = 0 \tag{1.15}$$

The set of equations (1.13)-(1.15) allows to describe the equilibrium state of the plasma in the solar atmosphere, including the photosphere and corona. It has been shown (Woltjer 1958, Gold and Hoyle 1960) that the pressure and gravity forces can be neglected in Eq. (1.15) for large parts of the corona: the gravity scale height is large compared to the variation of the magnetic field and the gas pressure, and the coronal plasma-β (ratio of the gas pressure and of the magnetic pressure) is, on average, less than 1 from the top of the chromosphere to about 2.5 solar radii. Neglecting the gas pressure and the gravity leads to the so-called ***force-free fields*** for which only the magnetic force is taken into account to determine the magnetic field configuration in the corona. This, according to Eq. (1.15), allows to neglect the pressure gradient and gravitational force only perpendicular to $\boldsymbol{B}$ so that

$$\boldsymbol{J}\times\boldsymbol{B} = 0 \tag{1.16}$$

$$\nabla p_{\shortparallel} = \rho\boldsymbol{g}_{\shortparallel} \tag{1.17}$$

i.e. that the Lorentz force vanishes and, consequently, that the electric currents can be assumed to be aligned with the magnetic field. Recent numerical simulations of flux emergence including partial ionization (Leake and Arber 2006) have shown that the final state of the coronal magnetic field is force-free. In fact, the solar atmosphere shows a varying pattern of dominance of either the plasma or the magnetic pressure. Thus, only for the atmospheric layers from the mid-chromosphere until the mid-corona one can regard the solar atmosphere as being almost entirely force-free, so that one is allowed to neglect the pressure gradient and gravitational term in Eq. (1.15) with the aforementioned conditions to ensure the validity of Eq. (1.16). Once the force-free approximation is justified, however, one finds a proportionality between the electric current density (assumed to be field-aligned) and the magnetic field, equivalent to Eq. (1.16), which can be written as

$$4\pi \boldsymbol{J} = \alpha \boldsymbol{B} \tag{1.18}$$

This equation is often rewritten in the form

$$\nabla \times \boldsymbol{B} = \alpha \boldsymbol{B} \tag{1.19}$$

where α is the so-called "force-free parameter" which is in general different for each field line, although it must be constant along a given field line. This can be seen by taking the divergence of Eq. (1.19) by the virtue of the solenoidal condition of Eq. (1.14) to obtain

$$\boldsymbol{B} \cdot \nabla \alpha = 0 \tag{1.20}$$

Three different assumptions on the nature of the force-free parameter can be made. First, the most simple of all approximations to the coronal magnetic field, is that α is zero everywhere, the field is potential. Secondly, if α has the same but nonzero value throughout the field domain, the resulting subclass of force-free fields is called a "constant α" or linear field, since the field components satisfy a linear differential equation (Nakagawa and Raadu 1972). Finally, if α depends on position in the field domain, the resulting subclass of force-free fields is nonlinear field which assumes that relation between the current density and the magnetic field is no longer linear. The detail explanations of the three classes of field will be illustrated in the next chapter.

2 Magnetic field extrapolations into the solar atmosphere

Despite the importance of the magnetic field in the physics of the corona and despite the tremendous progress made recently in the remote sensing of solar magnetic fields, reliable measurements of the coronal magnetic field strength and its orientation do not exist, except for a few individual cases in chromosphere, e.g., in newly developed active regions (Solanki et al. 2003). This is largely due to the weakness of coronal magnetic fields, previously estimated to be on the order of 10 G, and the difficulty associated with observing the extremely faint solar corona emission. Using a very sensitive infrared spectropolarimeter to observe the strong near-infrared coronal emission line Fe XIII λ10747 above active regions, one can succeeded in measuring the weak Stokes V circular polarization profiles resulting from the longitudinal Zeeman effect of the magnetic field of the solar corona (Lin et al. 2000). As a matter of fact, we must usually rely on numerical computations of the field that use the observed photospheric field as a boundary condition by using the model assumption that the corona is force-free. This so-called extrapolation requires a knowledge of the physical laws governing the coronal magnetic field. Classical approximations are a potential field (no electric current in the corona) or a linear force-free field (electric current proportional to the magnetic field and their ratio is constant throughout a volume). The algorithms and limitations of these techniques are well known, and they have been used extensively with magnetograms which routinely measure the photospheric magnetic field vector. The more realistic and more demanding of computational resources than the two above is a nonlinear force-free field (the electric current is parallel to the magnetic field and where their ratio is spatially varying). In this chapter, the focus lies on the why and how of "extrapolating" the force-free coronal magnetic field from routinely measured photospheric vector magnetograms.

In the following, we will point out the importance of inferring coronal magnetic field from boundary measurements on the photosphere in § 2.1. The three distinct classes of magnetic field models, namely potential, linear force-free and nonlinear force-free models arise from force-free assumptions are described in § 2.2, along with the existing computational methods to solve the related set of equations. Alternative attempts that are currently being carried out to measure the magnetic field higher up into the corona will be discussed in § 2.3. Finally, in § 2.4 a short summary is given.

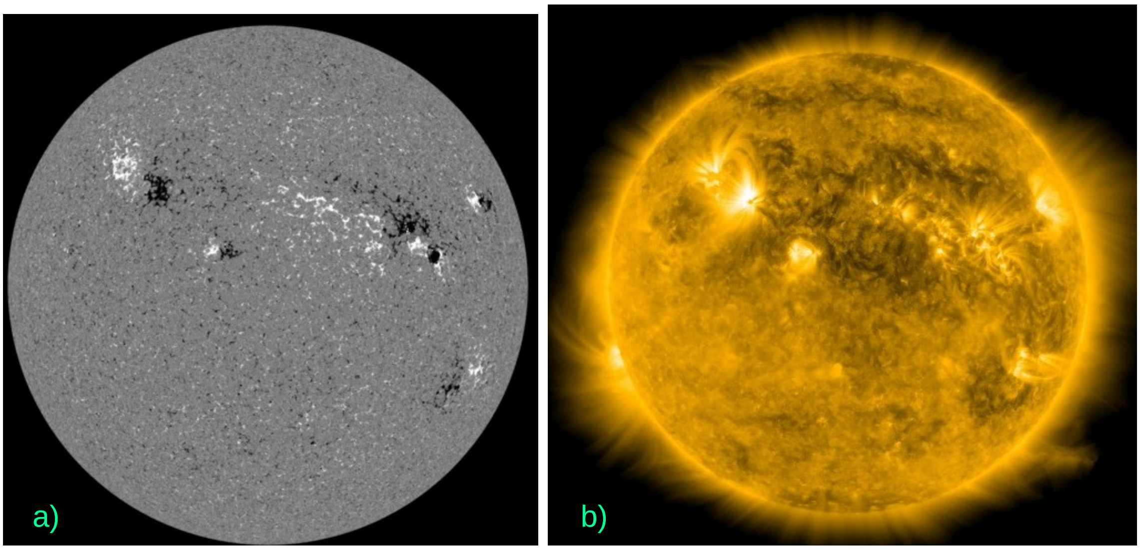

Figure 2.1: A comparison of a). a magnetogram from SDO/HMI on August 13th, 2010 with b). coronal emission from SDO/AIA at the same time, showing a clear correlation between regions of strong magnetic field and enhanced emission. Credit: SDO satellite / NASA.

2.1 Why extrapolation?

Coronal magnetic fields are believed to play a crucial role in several major unsolved mysteries of solar physics, including coronal heating, solar flares and coronal mass ejections (Priest 1982a, Benz 2002, Bhatnagar and Livingston 2005). Therefore, the determination by measurement or theoretical calculation of the magnetic field structure in the solar atmosphere is one of the most important tasks to improve our understanding of physical processes in the solar atmosphere (Aschwanden 2005). This can be seen quite clearly by comparing, for example, magnetograms and pictures of coronal emission (Fig. 2.1), which shows a strong correlation between regions of strong magnetic field and the regions of strongest emission. The measurement of fields throughout the coronal volume is an intrinsically more difficult problem since it requires three dimensional information, whereas photospheric fields are measured on a two dimensional surface. The techniques used to measure magnetic fields in the photosphere rely on Zeeman splitting and Stokes profile measurements and are not as effective in the solar corona, since lines formed at coronal temperatures are intrinsically broader and are scarce in the infrared where Zeeman splitting is (relatively) large. Alternatively, the Hanle effect on ultraviolet emission lines can be used to measure the coronal magnetic field but this requires space-based observations. In particular, Trujillo Bueno and Asensio Ramos (2007) used the He I 1083.0 nm multiplet and Raouafi et al. (2009) used the H I Lyα and Lyβ lines to test their ability to probe the coronal magnetic field. Coronal emission lines at optical frequencies are very faint and extremely broadened due to the low coronal plasma density and the high temperature of emitting ions, respectively. Not only the extraction of very weak signals hampers the success of coronal magnetic field measurements but also the necessary long integration times and the line-of-sight integrated character of the measurements (the latter especially for off-limb observations). Kramar et al. (2006) discussed the associated limitations and pictured the possibility of reconstructing the 3D structure of the coronal magnetic field based on longitudinal Zeeman effect measurements of magnetically sensitive lines, using a tomographic inversion method. Optionally, the gyroresonance emission of strong active-region magnetic fields, originating from electrons gyrating along the coronal magnetic field lines can be measured.

Under exceptional circumstances the measurement techniques applicable to the lower layers of the solar atmosphere can also be applied to measure magnetic fields at somewhat greater heights (e.g., Solanki et al. 2003), which is discussed in section 2.3. Solar physicists have thus been led to consider the so-called ***reconstruction*** problem of the coronal magnetic field: this consists of solving the equations of a model (defined by some reasonable assumptions about the physical state of the corona) as a Boundary Value Problem (BVP), the boundary conditions being taken to be the measured values of the magnetic field in the denser and cooler photosphere. Therefore, the extrapolation of magnetic field measurements taken at photosphere (and/or chromospheric) level into the corona to get an estimate of the coronal magnetic field is an essential tool for solar physics (Schmidt 1964, Semel 1967, Chiu and Hilton 1977, Seehafer 1978, Sakurai 1981, Seehafer 1982, Semel 1988, Wu et al. 1990, Cuperman et al. 1991, Demoulin et al. 1992, Mikic and McClymont 1994, Roumeliotis 1996, Amari et al. 1997, 1999, Clegg et al. 2000, Wheatland et al. 2000, Yan and Sakurai 2000, Wheatland 2004, Wiegelmann 2004, Valori et al. 2005, Neukirch 2005, Amari et al. 2006, Wiegelmann 2007, Tadesse et al. 2009, DeRosa et al. 2009, Wheatland and Régnier 2009)

However, the problem of extrapolation of photospheric magnetic fields into the corona is neither simple nor straightforward as we do not know which type of magnetic field we are really dealing with, i.e. which equations we have to solve. Then, does the boundary condition of the magnetic field on the photosphere suffice for a unique solution in the corona with a proper asymptotic behaviour at infinity? What are contributions of electric currents in the corona to its magnetic field distribution? Such questions cannot be answered in a simple way which leaves the door open to approximations and a priori assumptions in making physical models of the system (photosphere to corona) to compute coronal magnetic fields. Therefore, the extrapolated coronal magnetic field depends on assumptions regarding the coronal plasma, for example, force-freeness. Force-free means that all nonmagnetic forces like pressure gradients and gravity are neglected. This approach is well justified in the solar corona owing to the low plasma beta (which is the ratio of the thermal pressure p_{th} to the magnetic pressure p_{mag}). One has to take care, however, about ambiguities, noise and nonmagnetic forces in the photosphere, where the magnetic field vector is measured (Wiegelmann 2008, Cadez 2005).

The commonly used magnetic field extrapolation (or reconstruction) methods rely on various assumptions made about the physical conditions in the solar corona. The most commonly made assumptions are that

- the coronal magnetic field is in equilibrium and plasma flows can be neglected[1],

[1]If the flow speed is much smaller than the sound speed, the Alfvèn speed and the gravitational free-fall speed, it can be neglected.

- plasma densities are small so that the Lorentz force greatly exceeds the gravitational force.

- the ratio of thermal pressure to magnetic pressure (the plasm β) in the corona is small, and

- the corona structures change on length scales comparable to or shorter than the typical coronal scale height as explained in section 1.3 of the previous chapter.

The last two assumptions allow us to neglect force-free magnetic fields, carrying only field-aligned currents, with the sub-classes of nonlinear force-free fields, linear force-free fields and potential (current free) fields (Neukirch 2005). According to these assumptions, force-free coronal magnetic fields are defined entirely by requiring that the field has no Lorentz force and is divergence free (the "solenoidal condition"):

$$4\pi \boldsymbol{J} \times \boldsymbol{B} = (\nabla \times \boldsymbol{B}) \times \boldsymbol{B} = 0 \tag{2.1}$$

$$\nabla \cdot \boldsymbol{B} = 0 \tag{2.2}$$

where $\boldsymbol{B}$ and $\boldsymbol{J}$ are the vectors of the magnetic field strength and of the electrical current density, respectively. Equation (2.1) can be rewritten by introducing a scalar function (α), sometimes known as the torsion function, so that

$$4\pi \boldsymbol{J} = \nabla \times \boldsymbol{B} = \alpha \boldsymbol{B} \tag{2.3}$$

At the moment, potential ($\alpha = 0$) and linear force-free field (α = constant) extrapolation methods are still the most commonly used. There are two reasons for this:

1. these extrapolation methods are easy to use, both from the mathematical and the numerical point-of-view, and

2. line-of-sight magnetograms are more readily available, in particular through the MDI instrument on SoHO, and are easier to handle than vector magnetograph data.

Despite the popularity and frequent use of these simplified models (potential and linear force-free field) in the past, there are several limitations in these models, which are discussed in the next subsection. Both observational and theoretical arguments show that at least the magnetic field prior to eruptive processes in the corona is not a linear force free (or potential) field (Wiegelmann 2008). The nonlinear force-free field has a more most realistic description of the coronal magnetic field, which is subject of discussion in the next sections.

In general, the boundary value problem to be solved for the force-free fields requires the determination of the magnetic field in a given volume (enclosed by a boundary surface ∂V) in terms of the line-of-sight component or the full magnetic field vector on ∂V (in case of potential and linear or nonlinear force-free fields, respectively) such that the field vanishes at infinity. The boundary surface at the bottom of the computational domain, representing the solar photosphere, should be specified as a sphere or can be approximated with a planar surface, if the computational domain is much smaller than a solar radius.

2.2 Magnetic field models

In principle, if both the magnitude and direction of the magnetic field vector could be determined at every point in the solar corona at any given time, there would be no difficulty in programming a computer to construct a detailed three-dimensional field line map. Therefore, one has to be forced to infer magnetic field throughout corona volume using numerical models from photospheric footprint. The photospheric vector magnetic field of solar active regions has been measured for the last decades. These measurements provide the input to 3D numerical magnetic field models. The spatial resolution of measurements has improved steadily, and models are able to incorporate some departures from the force-free field approximation. Several of these models are now capable of reproducing the observed sheared coronal magnetic features. In the following subsections, basic coronal magnetic field models such potential, linear force-free, nonlinear force-free and MHD will be discussed independently.

2.2.1 Potential field models

The simplest way to model the coronal field is to assume that it is potential, i.e. that it carries no electric current. solutions for this model in plane geometry have been obtained by Schmidt (1964), for the case where the vertical component of the field is specified at the photospheric boundary. This model has now led to an almost routine type reconstruction, used for observational purposes (Sakurai 1989), but also for building initial conditions for dynamical MHD numerical simulations (Amari et al. 1996, Mikic et al. 1996). This assumption has proven to be adequate for many quiescent, old active regions and even for the non-eruptive global coronal-heliospheric interface (e.g., Wang and Sheeley 1990, Hoeksema 1991, Schrijver and De Rosa 2003). Studies of the coupling of the coronal field into the heliosphere suggest that the global coronal magnetic field is often largely potential. For the practical calculation of the global field, the so-called source-surface model has been introduced, in which the influence of the solar wind is artificially taken account of by the requirement that the field be radial at some exterior spherical (source) surface typically at $2.5R_\odot$ from the sun's center. The potential-field source surface (PFSS) model, uses this concept to extrapolate the line-of-sight surface magnetic field through the corona with the boundary assumed to be at the source surface. With the assumption of current-free corona, such models are not able to reproduce any topological developments of the coronal magnetic field. It is a fundamental theorem in electromagnetic theory the current-free magnetic field is the state of minimum energy subject to the given boundary condition. In other words, the variational problem for solenoidal vector field $\boldsymbol{B}$

$$W = \int_V \frac{\boldsymbol{B}^2}{8\pi} dV = \text{stationary},$$
$$B_n \text{ is given on S}$$

(B_n is the normal component of $\boldsymbol{B}$ on the boundary surface S), leads to the so-called Euler equation for variational problem which reduces to $\nabla \times \boldsymbol{B} = 0$ and it can be shown that the solution is unique and that it makes the functional W minimum (Sakurai 1979). Hence, they are only to be used for estimating the lowest-energy state corresponding to an observed line-of-sight magnetic field and they do not provide any estimate for the amount of energy which is built up in a solar active region prior to eruptions and the part of it which could be involved in the reconfiguration of the field. That is because this excess energy is mainly related to the change in the transversal (horizontal) photospheric magnetic field components which a potential field approach is not capable of reproducing.

The potential field model fails, of course, in many interesting cases because it is by definition wrong when we look at regions that can support flares, filament eruptions, or coronal mass ejections: such regions contain free energy in the form of strong electrical currents. Schrijver et al. (2005) showed that potential field model cannot be used to determine the energy contained in electrical currents and magnetic fields available for driving instabilities, or even provide the simple assessment of where such energy might exist within active regions.

The magnetic scalar potential ϕ is uniquely determinable if ϕ itself or if its normal derivative $\partial_n\phi$ (which is equivalent to the magnetic field component normal to the boundary B_n) is specified on the boundaries and, therefore, one has to solve a Dirichlet or Neumann boundary value problem, respectively. As the line-of-sight component of the magnetic field near the solar disk center is essentially radial it can be used to determine the distribution of magnetic sources which show a straightforward relation to the current-free field above the photosphere. Since any gradient, $\hat{\boldsymbol{n}} \cdot \nabla\phi$ is sufficient condition, the Laplace field can also be calculated far off disk center from the line-of-sight components. A solution is obtained by solving the Laplace equation for ϕ with the normal magnetic field as a boundary condition and standard methods, using either Green's functions or eigenfunction expansions, for this purpose are existing.

We shall pursue the solution of this boundary-value problem in a standard form of harmonic expansion in terms of eigen-solutions of the Laplace equation written in a spherical coordinate system, (r, θ, ϕ). Assuming that a currentless ($\boldsymbol{J} = 0$) approximation holds either throughout the space above the photospheric surface S_p, or between the photosphere and some spherical surface S_s (source surface), the force-free equation reduces to ,

$$\nabla \times \boldsymbol{B} = 0$$

, and can be rewritten using scalar potential Φ as

$$\boldsymbol{B} = -\nabla\Phi \tag{2.4}$$

Substituting Eq. (2.4) into divergence-free equation, $\nabla \cdot \mathbf{B}$, one can find Laplace equation for Φ as

$$\nabla^2\Phi = 0 \tag{2.5}$$

Using separation of variable in spherical (r, θ, ϕ) coordinates Eq. (2.5) has the solution (Jackson 1975):

$$\Phi(r, \theta, \phi) = \sum_{l=0}^{\infty} \sum_{m=-l}^{l} \left[A_{lm} r^l + B_{lm} r^{-(l+1)}\right] Y_{lm}(\theta, \phi) \tag{2.6}$$

where Y_{lm} are Spherical Harmonics expressed through the associated Legendre polynomials, $P_l^m(\cos\theta)$ by equation,

$$Y_{lm}(\theta,\phi) = \sqrt{\frac{2l+1(l+m)!}{4\pi(l+m)!}}P_l^m(\cos\theta)e^{im\phi} \tag{2.7}$$

where A_{lm} & B_{lm} are Spherical Harmonics coefficients. An intergrable function $g(\theta,\phi)$ can be represented as

$$g(\theta,\phi) = \sum_{l=0}^{\infty}\sum_{m=-l}^{l} C_{lm}Y_{lm}(\theta,\phi) \tag{2.8}$$

with C_{lm} is given by (Jackson 1975):

$$C_{lm} = \int_0^{2\pi}\int_0^{\pi} Y_{lm}^*(\theta,\phi)g(\theta,\phi)\sin\theta d\theta d\phi \tag{2.9}$$

with $Y_{lm}^* = (-1)^m Y_{l,-m}$. From the radial component of the vector magnetic field measured on the photosphere at $r = R_\odot$, we can prescribe Von Neumann boundary condition as $B_r(R_\odot,\theta,\phi) = \frac{\partial\Phi}{\partial r}$ and applying Eq. (2.9) to calculate C_{lm} for $g(\theta,\phi) = B_r(R_\odot,\theta,\phi)$. Hence the radial component of the magnetic field is given by

$$B_r(r,\theta,\phi) = \sum_{l=0}^{\infty}\sum_{m=-l}^{l}\left[A_{lm}lr^{l-1} - B_{lm}(l+1)r^{-(l+2)}\right]Y_{lm}(\theta,\phi) \tag{2.10}$$

The values of A_{lm} & B_{lm} are not completely determined with C_{lm}, hence we have to impose additional boundary condition with the assumption that magnetic field at source surface, S_s, is completely radial at $r \geq r_1$ as:

$$B_\theta = \frac{1}{r}\frac{\partial\Phi(r,\theta,\phi)}{\partial\theta} = 0 \quad \text{and} \quad B_\phi = \frac{1}{r\sin(\theta)}\frac{\partial\Phi(r,\theta,\phi)}{\partial\phi} = 0 \quad \text{at} \quad r = r_1 \tag{2.11}$$

Consequently the potential only depends on the radial component $r \geq r_1$, where

$$\Phi(r) = \sum_{l=0}^{\infty}\sum_{m=-l}^{l}\left[A_{lm}r^l + B_{lm}r^{-(l+1)}\right]$$

and all coefficient of Y_{lm} except $Y_{00} = 1$ have to vanish. Together with the photospheric boundary condition Eq. (2.9), one can get two equations to calculate A_{lm} and B_{lm} for $l \geq 1$:

$$A_{lm}lR_\odot^{(l-1)} - B_{lm}(l+1)R_\odot^{-(l+2)} = C_{lm} \tag{2.12}$$

$$A_{lm}r_1^l + B_{lm}r_1^{-(l+1)} = 0 \tag{2.13}$$

which leads to:

$$A_{lm} = \frac{C_{lm}R_\odot^{l+2}}{r_1^{2l+1} + l(R_\odot^{l+2} + r_1^{2l+1})} \tag{2.14}$$

$$B_{lm} = -\frac{C_{lm}R_\odot^{l+2}r_1^{2l+1}}{r_1^{2l+1} + l(R_\odot^{l+2} + r_1^{2l+1})} \tag{2.15}$$

The distance of the source surface sphere r_1 might be chosen in a way that we can fit some additional constraints, e.g., observations of radiating loops or helmet streamer. We might compare the magnetic field and observed plasma structures similar as for the cartesian linear force-free case and minimize with respect to r_1. Therefore, all components of potential field $\boldsymbol{B}$ can be calculated analytically from Φ.

In general, even if there are several limitations to potential field models which led to the introduction of the so-called constant-α and non-constant-α force-free hypothesis (both allow for the presence of electric currents in the corona) , the potential field has been used as initial condition for many nonlinear force-free model codes for extrapolating coronal magnetic field.

2.2.2 Linear force-free field models

Extrapolating magnetic fields from measured photospheric boundary upward into the corona are difficult due to the general nonlinear character of the equations. However, the linear force-free field model (LFF) corresponds to the case of a spatially constant (in general non-vanishing) α, in force-free equation $\nabla\times\boldsymbol{B} = \alpha\boldsymbol{B}$ (the ratio of field strength to current density is constant throughout a volume) (Chiu and Hilton 1977, Seehafer 1982, Semel 1988, Clegg et al. 2000, Alissandrakis 1981). This simplest variant of the force-free problem leads to a linear differential equation which collapses to the potential field when the constant of proportionality α vanishes. Taking the curl of $\nabla\times\boldsymbol{B} = \alpha\boldsymbol{B}$ one gets (in Cartesian coordinates) the Helmholtz equation:

$$\left(\nabla^2 + \alpha^2\right)\boldsymbol{B} = 0$$

It follows that a necessary (but not sufficient) condition for a linear force-free field is that it satisfies the Helmholtz equation. This subset is important because it gives the only general solution which can be used to understand currents in the solar atmosphere (Gary 1989). Linear force-free models might provide a rough estimate of the true 3D magnetic field structure if the nonlinearity is weak. The use of simpler models was often justified owing to limited observational data, in particular if only the line-of-sight photospheric magnetic field has been measured (Wiegelmann 2008).

Nakagawa and Raadu (1972) were first to describe a generalized representation of LFF magnetic fields and to provide (non-unique) solutions of force-free equation using a Fourier series expansion in Cartesian coordinates. Barbosa (1978) computed the surface Green's function for LFF magnetic fields and imposed boundary conditions on the normal component of $\boldsymbol{B}$ on two parallel planes which represent the force-free volume. This procedure ensures that the magnetic field energy remains bounded, and that the field lines have a smooth behaviour. Seehafer (1978) used a Fourier representation to seek the solution to the set of linear force-free equations in a Cartesian coordinate system. He pointed out that fields being linear force-free in the whole volume outside the Sun neither possess a finite energy content nor can be determined uniquely from the normal photospheric magnetic field component alone. In other words, he found that the consideration of global-scale LFF fields is problematic.

Linear force-free fields have certain properties that limit their usefulness as solutions to the boundary-value problem posed by photospheric magnetic field determinations.

Chiu and Hilton (1977) had investigated that LFF fields have non-unique solutions if only the normal (line-of-sight) magnetic field at the photosphere is used as boundary. To achieve uniqueness both the normal and tangential component need to be defined on the boundary so that the physical character of the field is clearly reflected. Linear force-free fields are not suitable for problems like strong localized currents and for detailed studies of the energy and helicity budgets of active regions, and the calculated magnetic fields perhaps do not contain free energy (Wheatland 1999). Differencing of observationally determined transverse field values provides estimates of α over an active region. Measurements of this type typically show a highly nonuniform distribution of α (e.g., Wang 1993, Pevtsov et al. 1994), indicating that strong field-aligned currents flow in localized areas in active regions. Therefore linear fields cannot reproduce the observed localized currents. In addition, linear force-free fields are poor models of large-scale coronal fields for two reasons (Wheatland 1999). First, in general, linear force-free fields have an infinite energy in a half-space (apart from a restricted class of linear fields ; see Aly 1992)), making them unsuitable as large-scale models of the field above a "photospheric plane". Second, linear force-free fields do not become potential at large distance.

Because of the limitations of linear force-free field modeling, considerable effort has been devoted to methods for calculating nonlinear force-free fields to match the photospheric boundary conditions.

2.2.3 Nonlinear force-free field models

Potential and LFF fields are inappropriate in reproducing the energy content of the coronal magnetic field accurately, since they cannot hold the full magnetic energy content according to their computation from the measured normal (line-of-sight) magnetic field only. Usually α (of Eq. 2.3) changes in space, even inside one active region. This can be seen, if we try to fit for the optimal linear force-free parameter α by comparing field lines with coronal plasma structures. An example is given by Wiegelmann and Neukirch (2002) where stereoscopic reconstructed loops by Aschwanden et al. (1999) have been compared with a linear force-free field model. The optimal value of α changes even sign within the investigated active regions, which is a contradiction to the α= constant linear force-free approach.

A realistic way to model the non-potential coronal fields in active regions is to assume that the electric currents are parallel to the magnetic field, $\nabla \times \boldsymbol{B} = \alpha \boldsymbol{B}$, with α being constant only along every field line ($\boldsymbol{B} \cdot \nabla\alpha = 0$) but varying from field line to field line, giving us the nonlinear force-free field (NLFFF). The computation of nonlinear force-free fields is however, more challenging for several reasons. Mathematically, problems regarding the existence and uniqueness of various boundary value problems dealing with nonlinear force-free fields remain unsolved (see Amari et al. 2006, for details). Another issue is their numerical analysis of given boundary values. This class of field configuration is complex to compute, and solutions depend strongly on the implementation of the boundaries. An additional complication is to derive the boundary data from observed photospheric vector magnetic field measurements, which are consistent with the force-free assumption. Measurement uncertainties in the transverse components of the measured field vector, ambiguities regarding the field direction, and non-magnetic forces in the photosphere complicate the task of deriving suitable boundary conditions from measured data.

The assumption of force-freeness is well accepted for the coronal magnetic fields in active regions, while it is not true for the photosphere. The photospheric plasma is a finite β-plasma and nonmagnetic forces like pressure gradient and gravity cannot be neglected. As a result, electric currents have a component perpendicular to the magnetic field, which contradicts the force-free assumption. We will discuss later in the next chapter how these difficulties can be mitigated using a preprocessing scheme.

Several methods have been developed over the past few decades to compute the most general class of force-free fields, the nonlinear force-free (NLFF)field. This class of field configuration is difficult to compute, and solutions depend strongly on the implementation of the boundaries. For a more complete review of existing methods for computing nonlinear force-free coronal magnetic fields, we refer to the review works by Amari et al. (1997), Schrijver et al. (2006), Metcalf et al. (2008), Wiegelmann (2008), Régnier (2007).

2.2.3.1 Upward integration method

This method was among the first to be seriously investigated for nonlinear force-free extrapolation. The basic equations for the upward integration method (or progressive extension method) have been published by Nakagawa (1974). The upward integration method is a straight forward approach to use the nonlinear force-free equations (2.2 & 2.3) directly to extrapolate the photospheric magnetic field into the corona. The idea is to reformulate the nonlinear force-free equations as:

$$\frac{\partial B_x}{\partial z} = \alpha B_y + \frac{\partial B_z}{\partial x} \tag{2.16}$$

$$\frac{\partial B_y}{\partial z} = -\alpha B_x + \frac{\partial B_z}{\partial y} \tag{2.17}$$

$$\frac{\partial B_z}{\partial z} = -\frac{\partial B_x}{\partial x} - \frac{\partial B_y}{\partial y} \tag{2.18}$$

$$\alpha = \frac{1}{B_z}\Big(\frac{\partial B_y}{\partial x} - \frac{\partial B_x}{\partial y}\Big) \tag{2.19}$$

$$\alpha\frac{\partial B_z}{\partial y} = \frac{\partial}{\partial x}\Big(\frac{\partial B_y}{\partial z}\Big) - \frac{\partial}{\partial y}\Big(\frac{\partial B_x}{\partial z}\Big) \tag{2.20}$$

and to integrate this set of equations upwards in z from the knowledge of $\boldsymbol{B}(x, y, 0)$ and its vertical derivatives on the lower boundary $z = 0$. It is a Cauchy or initial value problem with the vertical coordinate z playing the role of time. However, this initial value problem is mathematically ill-posed[2], since the solutions do not depend continuously on the photospheric initial values (Wu et al. 1990, Demoulin et al. 1992, Amari et al. 1997) and therefore small changes or inaccuracies in the measured boundary data lead to a divergent extrapolated field (Low and Lou 1990). In particular one finds that exponential growth of the magnetic field with increasing height is a typical behavior.

The upward integration method has been recently reexamined by Song et al. (2006) who developed a new formulation of this approach. The new implementation uses smooth

[2]The errors in the solution grow up as one goes higher up from the lower boundary.

continuous functions and the equations are solved in asymptotic manner iteratively. The original upward integration equations are reformulated into a set of ordinary differential equations and uniqueness of the solution seems to be guaranteed at least locally.

2.2.3.2 Grad-Rubin methods

This method dates back to the classical work by Grad and Rubin (1958), in which it was first presented (of course not for use in coronal magnetic field extrapolation). The method reformulates the nonlinear force-free equations in such a way, that one has to solve two well posed boundary value problems. This makes this approach also interesting for a mathematical investigation of the structure of the nonlinear force-free equations. It solves either for the magnetic field, the electric current density or the magnetic vector potential. At first, a potential field is computed only from the line-of-sight photospheric magnetic field whose transversal components are then used to compute the photospheric α distribution for one polarity. The field is then iteratively updated in the computational volume until the recalculation does not yield a change in the configuration anymore and thus can be regarded as a stationary state.

The Grad & Rubin method as implemented by Wheatland (2004, 2006) is similar to that of Sakurai (1981) where the current distribution is modelled in terms of cylindrical current elements between nodal points on a small number of calculated field lines. The magnetic force is calculated at each nodal point due to all current elements using an exact integral solution of the Ampere's law. In Wheatland (2004), the magnetic field due to the currents is calculated at each grid points instead of only at nodal points.

The more frequently used form of the Grad-Rubin method is the one given by Amari et al. (1997, 1999). This approach decomposes equations (2.1)-(2.3) into a 1st order hyperbolic part for evolving α along the magnetic field lines and an elliptic one to iterate the updated magnetic field from Amperes law. For every iteration step k one has to solve iteratively for

$$\boldsymbol{B}^k \cdot \nabla \alpha^k = 0 \tag{2.21}$$

$$\nabla \times \boldsymbol{B}^{k+1} = \alpha^k \boldsymbol{B}^k \tag{2.22}$$

$$\nabla \cdot \boldsymbol{B}^{k+1} = 0 \tag{2.23}$$

which evolves α in the volume. Amari et al. (2006) have improved the numerical scheme in many ways, e.g. by injecting the current density only in one step, by ensuring the $\nabla \cdot \boldsymbol{J} = 0$ at a high level of accuracy, or by improving the determination of the boundary values of the transverse component of the vector potential.

Inhester and Wiegelmann (2006) implemented a Grad-Rubin code on a finite element grid with staggered field components. The method first propagates the α value along field lines and then updates the magnetic field using a residual vector potential and also ensuring the condition $\nabla \cdot \boldsymbol{J} = 0$. Since Eq. (2.21) is 1st order, only one boundary condition is needed. This leads to conflicts on field lines which have both foot points anchored in the photosphere. A balancing scheme between the two boundary values was introduced by Inhester and Wiegelmann (2006) and later by Wheatland and Régnier (2009).

2.2.3.3 MHD relaxation methods

These methods do not make use of the NLFF equations directly, rather the magnetohydrodynamic (MHD) equations are simulated in a simplified or modified form (Chodura and Schlueter 1981). The idea is to start with a suitable magnetic field which is not in equilibrium and to relax it into a force-free state. This is done by using the MHD equations in the following form:

$$\upsilon \boldsymbol{v} = (\nabla \times \boldsymbol{B}) \times \boldsymbol{B} \tag{2.24}$$

$$\boldsymbol{E} + \boldsymbol{v} \times \boldsymbol{B} = 0 \tag{2.25}$$

$$\frac{\partial \boldsymbol{B}}{\partial t} = -\nabla \times \boldsymbol{E} \tag{2.26}$$

$$\nabla \cdot \boldsymbol{B} = 0 \tag{2.27}$$

where υ and $\boldsymbol{E}$ are viscosity and the electric field, respectively. As the MHD relaxation aims for a quasi-physical temporal evolution of the magnetic field from a non-equilibrium toward a (nonlinear force-free) equilibrium this method is also called 'evolutionary method' or 'magneto-frictional method'. The equation of motion (Eq. 2.24) has been modified by eliminating the plasma inertia and introducting viscous friction in such a way that it ensures that the (artificial) velocity field is reduced. Equation (2.25) has no Ohmic resistance included and therefore ensures that the magnetic connectivity remains unchanged during the relaxation except magnetic diffusion due to numerical effect. The artificial viscosity υ plays the role of a relaxation coefficient which can be chosen in such way that it accelerates the approach to the equilibrium state. A typical choice is

$$\upsilon = \frac{1}{\mu}|\boldsymbol{B}|^2 \tag{2.28}$$

with μ=constant. Combining equations (2.24), (2.25), (2.26) and (2.28) we get an equation for the evolution of the magnetic field during the relaxation process,

$$\frac{\partial \boldsymbol{B}}{\partial t} = \mu \boldsymbol{F}_{\mathrm{MHD}} \tag{2.29}$$

with

$$\boldsymbol{F}_{\mathrm{MHD}} = \nabla \times \left(\frac{[(\nabla \times \boldsymbol{B}) \times \boldsymbol{B}] \times \boldsymbol{B}}{B^2} \right) \tag{2.30}$$

This equation is then solved numerically starting with a given initial condition for $\boldsymbol{B}$, usually a potential field. Equation (2.29) ensures that equation (2.27) is satisfied during the relaxation if the initial magnetic field satisfies it.

The MHD evolutionary method as implemented by McClymont and Mikic (1994) follows the time-dependent evolution of the resistive, viscous, MHD equations using changing boundary conditions. An incompressible two-dimensional flow is imposed on the boundary in order to inject the observed current density (due to transverse field) in the magnetic configuration. The stress-and relax method (Roumeliotis 1996) is very similar to the MHD evolutionary technique solving similar MHD equations. But the resistive relaxation is driven by the transverse components of the magnetic field and also includes the uncertainty of the magnetic field measurements. The magnetofrictional method (Yang et al. 1986) uses a dissipative relaxation to drive the MHD equations towards an equilibrium. The boundary conditions are injected by a series a stress-and-relax procedures. This method has been recently implemented by Valori et al. (2005) with a zero plasma β which results in a final state close to a force-free state.

2.2.3.4 Boundary element or Greens function like methods

The boundary integral method has been developed by Yan and Sakurai (2000). The method relates the measured boundary values with the nonlinear force-free field in the entire volume by considering the half-space above the lower boundary with vanishing field at infinity. Following Green's second identity, the solution at a given point i inside a volume V and for a boundary field $\boldsymbol{B}_0$ on $S = \partial V$ is given by:

$$c_i \boldsymbol{B} = \oint_S \left(\boldsymbol{Y} \frac{\partial \boldsymbol{B}}{\partial n} - \frac{\partial \boldsymbol{Y}}{\partial n} \boldsymbol{B}_0 \right) dS \tag{2.31}$$

where $c_i = 1$ for points in the volume and $c_i = 1/2$ for points on the boundary S. $\boldsymbol{Y}$ is an kernel function which depends on $\boldsymbol{B}$ and has to be determined iteratively in a such way that a remaining volume integral vanishes. An iterative scheme has been developed (Yan and Sakurai 2000, Li et al. 2004) to compute the NLFF field at given point in the coronal volume from the boundary conditions given by the three components of the magnetic field. In the work of Yan and Sakurai (2000) a volume integral is needed to determine the auxiliary function at any point. Yan and Li (2006) have recently implemented a new version of the boundary integral method avoiding the volume integral. Different from other method, it allows, however, to evaluate the NLFFF field at every arbitrary point within the domain from the boundary data, without the requirement to compute the field in an entire domain. This is in particular useful if one is interested to compute the NLFFF field only along a given loop.

2.2.3.5 Optimization approach

Wheatland et al. (2000) have proposed an optimization method for the calculation of nonlinear force-free fields and later Wiegelmann (2004) improved the method. Note that another optimization scheme has been implemented by McTiernan (see Schrijver et al. 2006, Inhester and Wiegelmann 2006). The method minimizes a functional $\mathcal{L}$, which is an integral sum of the normalized Lorentz forces and the divergence of the field (each of which should equal zero) throughout the volume of interest, V. The minimization of the global departure of an initial field from a force-free and solenoidal state is realized for a vector field $\boldsymbol{B}(x, t)$ within a volume V by minimizing the quantity $\mathcal{L}$ as:

$$\mathcal{L} = \int_V \left[B^{-2} |(\nabla \times \boldsymbol{B}) \times \boldsymbol{B}|^2 + |\nabla \cdot \boldsymbol{B}|^2 \right] dV \tag{2.32}$$

The minimization of $\mathcal{L}$ constitutes a variational problem and the related Euler-equations directly tell us how to iterate $\boldsymbol{B}$ so as to find the minimum. The detail description of optimization method and the extension of its scheme to spherical geometry is the subject of this thesis and will be presented in the next chapters.

2.2.4 MHD models

Magnetohydrodynamics (MHD) models are also becoming key tools to study time evolution of coronal magnetic field. The idea is to solve MHD equations using photospheric magnetic field boundary as input. The basic equations are:

$$\frac{\partial \rho}{\partial t} + \nabla \cdot (\rho \mathbf{v}) = 0 \tag{2.33}$$

$$\rho\Big(\frac{\partial \mathbf{v}}{\partial t} + \mathbf{v} \cdot \nabla \mathbf{v}\Big) + \nabla p - \boldsymbol{J} \times \boldsymbol{B} + \rho \boldsymbol{g} = 0 \tag{2.34}$$

$$\nabla \times \boldsymbol{B} - 4\pi \boldsymbol{J} = 0 \tag{2.35}$$

$$\frac{\partial \boldsymbol{B}}{\partial t} + \nabla \times \boldsymbol{E} = 0 \tag{2.36}$$

$$\boldsymbol{E} + \mathbf{v} \times \boldsymbol{B} = 0 \tag{2.37}$$

$$\nabla \cdot \boldsymbol{B} = 0 \tag{2.38}$$

where the plasma is subjected to a plasma pressure gradient ∇p, the Lorenz force $\boldsymbol{J} \times \boldsymbol{B}$ per unit volume and gravitational per unit volume. Furthermore, ρ, $\boldsymbol{J}$, $\mathbf{g}$, $\boldsymbol{E}$, and $\boldsymbol{B}$ stand for the plasma density, electric current density, gravitational acceleration, electric field, and magnetic field, respectively.

Global MHD models are a more recent development. Relying on solutions to more complex equations and requiring significantly more computational power, the first global solutions incorporating observed photospheric fields into the boundary conditions were produced by Mikic et al. (1996), Usmanov (1996). Otto et al. (2007) have used a linear force free field extrapolation to generate initial magnetic field $\boldsymbol{B}$ for a time-dependent MHD simulations. In their work, the presented solar magnetic field expansion and simulation model provide a straightforward method which can incorporate observed solar magnetic fields into MHD simulations of the dynamics of magnetic structure. The model uses an extrapolation of the solar fields which is consistent with generic MHD boundary conditions. The model includes the photosphere, chromosphere, and solar transition region and results indicate that this transition region may be important for the dynamics of solar magnetic structure.

2.3 Alternatives

The measurement of magnetic fields throughout the coronal volume is an intrinsically more difficult problem since it requires three dimensional information, whereas photospheric fields are measured on a two dimensional surface. The techniques used to measure magnetic fields in the photosphere rely on Zeeman splitting and Hanle effect. The required Stokes profile measurements and are not as effective in the solar corona, since lines formed at coronal temperatures are intrinsically broader and are scarce in the infrared where Zeeman splitting is (relatively) large. Under exceptional circumstances the measurement techniques applicable to the lower layers of the solar atmosphere can also be applied to measure magnetic fields at somewhat greater heights (e.g., Solanki et al. 2003).When suitable lines exist in the infrared and optical regimes (e.g., Judge 1998, Kuhn et al. 1999, Lin et al. 2000), they can only be used for observations above the limb because of the strong photospheric flux which contaminates the spectra against the solar disk. Coronal lines are prevalent at X-ray and EUV wavelengths and can be used to observe regions on the solar disk, but polarimetry is more difficult at these wavelengths and Zeeman splitting is only a small fraction of the thermal widths of the lines.

High resolution images from the EUV telescopes on the SOHO and TRACE satellites are ideal for tracing magnetic field lines in the solar corona. This is because the line emission processes responsible for coronal lines are proportional to the square of the number density, and thus are very sensitive to density contrasts. In a strongly magnetized plasma the inhibition of transport perpendicular to the magnetic field naturally results in such strong density contrasts, but only a subset of the coronal field lines is illuminated by this process.

In principle one can use the polarization of emissions from magnetic sensitive coronal line transitions to draw conclusions about the coronal magnetic field. These lines, however, are very faint so that in the past they have only occasionally been observed (e.g., House 1977, Arnaud and Newkirk 1987). In their study Judge et al. (2001) conclude that several forbidden lines (e.g., of Fe XIII, He I, Mg VIII, and Si IX) may be used to determine the coronal magnetic field. They further concluded that space-born missions are not needed for such kinds of coronal magnetometers but a high, dry mountain site. In their study they propose a focal plane instrument devoted to the $1\mu m$ region. These authors also point out that besides the observational part, a further major problem is the interpretation of the data. Because of the optically thin coronal plasma, direct measurements of the coronal magnetic field have a line-of-sight integrated character and to derive the accurate 3D structure of the coronal magnetic field a vector tomographic inversion is required. Corresponding feasibility studies based on coronal Zeeman and Hanle effect measurements have been done by Kramar et al. (2006) and Kramar and Inhester (2006).

2.4 Summary and conclusions

The magnetic field contains the dominant energy per unit volume in the solar corona and therefore plays an important role in most coronal phenomena. But until now, no direct measurement of the magnetic field vector distribution in the corona could be made. In recent years the accuracy of magnetic field observations in the solar atmosphere has made considerable progress. Models of the coronal magnetic field rely almost entirely on extrapolations of photospheric magnetic field observations. Therefore, numerical methods to estimate the magnetic fields in the upper solar atmosphere have been developed and extensively tested. Based on a number of assumptions about the physical conditions in the mid-and-upper chromosphere and corona its magnetic field can be calculated using force-free field extrapolation methods. The coronal magnetic field can be approximated either by potential (current-free), linear force-free (constant-α) or nonlinear force-free (non-constant-α) fields. While potential and constant-α fields are only capable of reproducing the true coronal magnetic field (and in particular its magnetic energy content) to a certain extent the more general approach of non-constant-α fields is favourable. In contrast to the aforementioned simpler models, these methods need the full photospheric magnetic field vector as the lower boundary condition.

The next chapter, therefore, deals with the application of optimization procedure along with preprocessing boundary data in spherical geometry for modeling nonlinear force-free coronal magnetic field above solar-like model active regions. In particular, mathematical derivations of optimization and preprocessing procedures in spherical geometry are analysed.

3 Optimization and preprocessing procedures in spherical geometry

Routine measurements of the solar magnetic field vector are mainly carried out only in the photosphere. Therefore, we compute the field in the higher layers of the solar atmosphere from the measured photospheric field under the assumption that the corona plasma is force-free. However, the measured photospheric magnetic field vector is inconsistent with the above force-free assumption. Therefore, one has to apply some transformations to these data before nonlinear force-free extrapolation codes can be applied. High noise in the transverse components of the measured field vector, ambiguities regarding the field direction, and non-magnetic forces in the photosphere complicate the task of deriving suitable boundary conditions from measured data. Extrapolation codes in cartesian geometry do not take the curvature of the Sun's surface into account (Wiegelmann 2007, Tadesse et al. 2009). The main emphasis of this chapter (have partly been published in Tadesse et al. (2009)) is to describe a method for nonlinear force-free coronal magnetic field modelling and preprocessing of photospheric vector magnetograms in spherical geometry using the optimization procedure over a restricted area of the Sun.

In the following, the optimization approach to extrapolate the coronal magnetic field for the analysis of solar active regions in spherical geometry as used in the presented thesis is discussed in § 3.1 and the method to provide consistent boundary conditions to this computational method is outlined in § 3.2. Finally, in § 3.3 a short summary is given.

3.1 Optimization procedure in spherical geometry

The optimization procedure is one of several methods that have been developed over the past few decades to compute the most general class of those force-free fields. Optimization methods have the advantage of being conceptually straightforward and are reasonably easy to implement. The optimization approach as implemented by Wheatland et al. (2000) has been used to compute magnetic fields using all six boundaries of a computational box. This causes a serious limitation of the method because such data are only available for model configurations. Potential fields[1] have been used for the five boundaries at the top and lateral directions for which observations usually are not present. However, these assumed boundary data may have a strong influence on the solution. For the reconstruction of the coronal magnetic field it is necessary to develop a method which reconstructs the magnetic field only from photospheric vector magnetograms (the three components

[1]It is a field that we have calculated from vertical component of the surface magnetic field.

of surface field). Vector magnetograms provide boundary conditions only for the bottom boundary of a computational box while the other five boundaries remain unknown. But later on Wiegelmann (2004) extended this method and showed how the coronal magnetic field can be reconstructed only from the bottom boundary, where the boundary conditions are measured with vector magnetographs. It is therefore important to diminish the effect of the top and lateral boundaries on the magnetic field inside the computational box. This can be done either by including a variation of $\boldsymbol{B}$ not only in the interior but also on those boundaries where $\boldsymbol{B}$ is unknown. This approach, however, is numerically difficult because it involves two types of variations. Wiegelmann (2004) showed that it is essentially equivalent to introducing finite size boundary regions on those boundaries where $\boldsymbol{B}$ is unknown with the weighting function $w(x, y, z)$ different from unity. The wieghting function is desirable to move these faces as far away as possible from the region of interest.

In the optimization approach, a functional $\mathcal{L}$ containing force-free equations (2.1) & (2.2) is minimized. The method directly uses the magnetic field vector at the bottom boundary of the computational box and an explicit computation of α is not necessary. In the next subsection We describe how the required boundary conditions can be derived from magnetic field measurements. Another advantage of the method is that the quality of the reconstructed magnetic field (force-free and solenoidal condition) is controlled automatically within the iteration procedure. The good performance of the optimization method, as indicated in Schrijver et al. (2006), encouraged us to develop a spherical version of the optimization code such as in Wiegelmann (2007), Wiegelmann et al. (2007), Tadesse et al. (2009). Wiegelmann (2007) has developed spherical version of the optimization principle for the whole sphere with two boundaries at the photosphere and source surface. In this section of this chapter, we describe a newly developed code that originates from a cartesian force-free optimization method implemented by Wiegelmann (2004). This new code takes the curvature of the Sun's surface into account when modeling the coronal magnetic field in restricted area of the Sun (not the whole sphere but part of it).

Large model volumes at high spatial resolution are required which not only accommodate the connectivity within an active region but also the connectivity to the surrounding. This has become clear already in an earlier application of existing extrapolation codes to Hinode/SOT-SP data by Schrijver et al. (2008) and it has been worked out that a vector magnetogram with a small field-of-view (not containing an entire active region and its surrounding) does not provide the necessary magnetic connectivity for an unbiased nonlinear force-free extrapolation. DeRosa et al. (2009) compared several nonlinear force-free codes in cartesian geometry with stereoscopic reconstructed loops as produced by Aschwanden et al. (2008). The codes used as input vector magnetograms from the Hinode-SOT-SP, which were unfortunately available for only a very small field of view (about 10 percent of the area spanned by STEREO-loops). Outside the Hinode FOV (field of view) line-of-sight magnetograms from SOHO/MDI were used and in the MDI-area, different assumptions about the transversal magnetic field have been made. Unfortunately, the comparison inferred that when different codes were implemented in the region outside the Hinode-FOV in different ways, the resulting coronal magnetic field models produced by the separate codes were not consistent with the STEREO-loops. The recommendations of the authors are that one needs vector magnetograms in larger field of views , the codes need to account for uncertainties in the magnetograms, and one must have a clearer

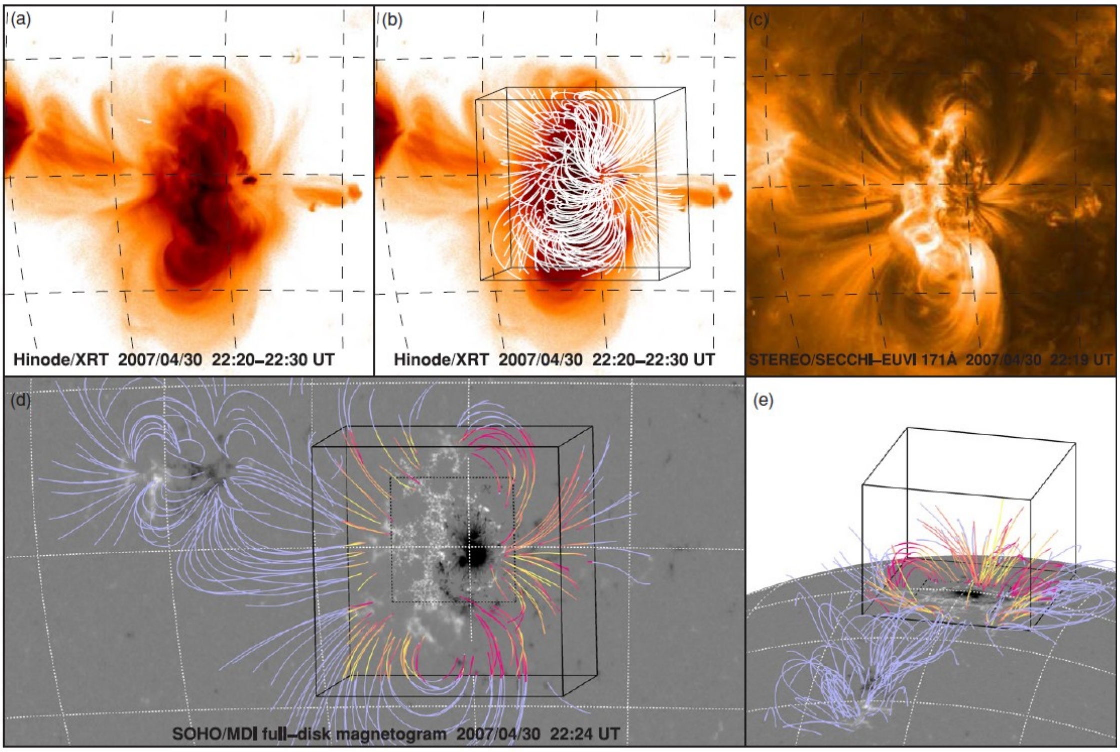

Figure 3.1: Series of co-aligned images of AR 10953 (with the same 10° gridlines drawn on all images for reference). (a) Time-averaged and logarithmically scaled Hinode/XRT soft X-ray image, and (b) with the best-fit Wheatland model field lines overlaid. (c) STEREO-A/SECCHI-EUVI 171 Å image. (d) Trajectories of loops, as viewed from the perspective of an observer located along the Sun-Earth line of sight and determined stereoscopically from contemporaneous pairs of images from the two STEREO spacecraft. (e) Same visualization as panel (d) but viewed from the side. (credit: DeRosa et al. (2009)).

understanding of the photospheric-to-corona interface. For a meaningful application of extrapolation codes on full disc vector magnetograms (i.e., SOLIS/VSM or SDO/HMI), we have to take the curvature of the Sun into account and carry out nonlinear force-free computations in spherical geometry.

In the following, we describe an optimization procedure in spherical geometry and then, we apply it to a known nonlinear force-free test field and calculate some figures of merit for different boundary conditions.

3.1.1 Numerics of the optimization procedure

The force-free magnetic fields Equations (2.1) and (2.2) can be solved with the help of an optimization principle, as proposed by Wheatland et al. (2000) and generalized by Wiegelmann (2004) for cartesian geometry. The method minimizes a joint measure ($\mathcal{L}_\omega$) of the normalized Lorentz forces and the divergence of the field throughout the volume of interest, V. Here we define a functional in spherical geometry (Wiegelmann 2007):

$$\mathcal{L}_\omega = \int_V \omega(r,\theta,\phi) B^{-2}\left(\Omega_a^2 + \Omega_b^2\right) r^2 \sin\theta \, dr \, d\theta \, d\phi \tag{3.1}$$

with

$$\Omega_a = B^{-2}(\nabla \times \boldsymbol{B}) \times \boldsymbol{B}\,, \tag{3.2}$$

$$\Omega_b = B^{-2}(\nabla \cdot \boldsymbol{B})\boldsymbol{B} \tag{3.3}$$

where $\boldsymbol{B}$ is the discrete vector of all magnetic field components which we split into those of the interior, $\bar{\boldsymbol{B}}$, and those on the boundary $\tilde{\boldsymbol{B}}$. $\omega(r,\theta,\phi)$ is a positive weighting function and V is computational volume.

It is obvious that the force-free Eqs. (2.1) and (2.2) are fulfilled when $\mathcal{L}_\omega$ equals zero. We minimize Equation (3.1) with respect to an iterative parameter t (see the Appendix for details) and obtain an iterative equation for the magnetic field:

$$\frac{1}{2}\frac{d\mathcal{L}_\omega}{dt} = -\int_V \frac{\partial \boldsymbol{B}}{\partial t} \cdot \tilde{\boldsymbol{F}} \; r^2 \sin\theta \, dr \, d\theta \, d\phi - \oint_S \frac{\partial \boldsymbol{B}}{\partial t} \cdot \tilde{\boldsymbol{G}} dS \tag{3.4}$$

where

$$\tilde{\boldsymbol{F}} = \omega \boldsymbol{F} + (\Omega_a \times \boldsymbol{B}) \times \nabla\omega + (\Omega_b \cdot \boldsymbol{B})\nabla\omega\,, \tag{3.5}$$

$$\tilde{\boldsymbol{G}} = \omega \boldsymbol{G} \tag{3.6}$$

$$\boldsymbol{F} = \nabla \times (\Omega_a \times \boldsymbol{B}) - \Omega_a \times (\nabla \times \boldsymbol{B}) + \nabla(\Omega_b \cdot \boldsymbol{B}) - \Omega_b(\nabla \cdot \boldsymbol{B}) + (\Omega_a^2 + \Omega_b^2)\boldsymbol{B}\,, \tag{3.7}$$

$$\boldsymbol{G} = \hat{\boldsymbol{n}} \times (\Omega_a \times \boldsymbol{B}) - \hat{\boldsymbol{n}}(\Omega_b \cdot \boldsymbol{B}) \tag{3.8}$$

and $\hat{\boldsymbol{n}}$ is the inward unit vector on the surface S that is bounding the volume V. The surface integral in Eq. (3.4) vanishes if the magnetic field is not varied on the boundaries of a computational box. The functional $\mathcal{L}_\omega$ in Eq. (3.1) will decrease if $\boldsymbol{B}$ is evolved inside the computational volume according to the iterative equation:

$$\frac{\partial \bar{\boldsymbol{B}}}{\partial t} = \mu \tilde{\boldsymbol{F}}\,, \tag{3.9}$$

with a sufficiently small constant $\mu > 0$, and if the magnetic field vector is kept constant on the boundaries during iterations, it leads to:

$$\frac{\partial \tilde{\boldsymbol{B}}}{\partial t} = 0\,, \tag{3.10}$$

on S. One can see that Eqs. (3.9) and (3.10) lead to

$$\frac{d\mathcal{L}_\omega}{dt} = -2\int_V \mu \tilde{F}^2 \; r^2 \sin\theta \, dr \, d\theta \, d\phi \;\leq 0 \tag{3.11}$$

where equality only occurs if $\tilde{\boldsymbol{F}} = 0$. The condition in Eq. (3.10) needs all the three components of the magnetic field on the boundary, which leads to an ill-posed problem, as there are no such measurements on top and lateral boundaries. Relaxing these top and lateral boundaries is possible (Wiegelmann and Neukirch 2003) and leads to an additional

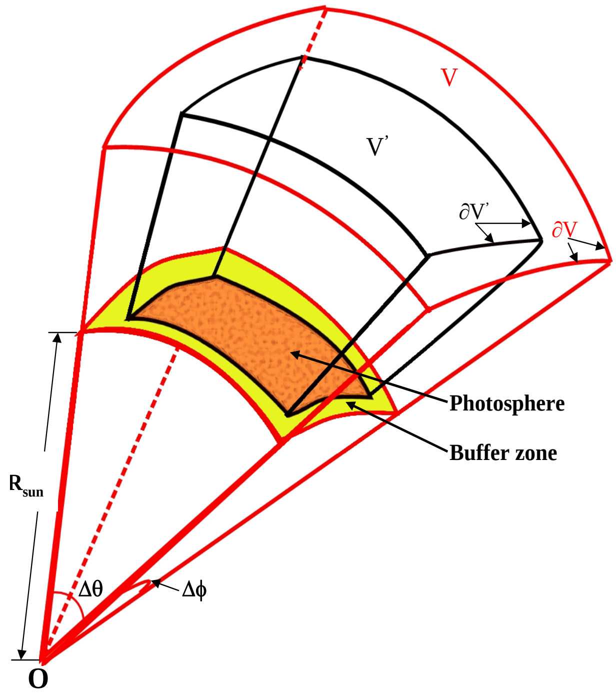

Figure 3.2: Wedge-shaped computational box of volume V with the inner physical domain V' and a buffer zone. O is the center of the Sun.

term in Eq. (3.11).

$$\frac{d\mathcal{L}_\omega}{dt} = -2\int_V \mu\tilde{F}^2\, r^2 \sin\theta\, dr\, d\theta\, d\phi - 2\oint_S \mu\tilde{G}^2\, dS \;\leq 0 \tag{3.12}$$

$$\text{if} \quad \begin{cases} \partial_t\tilde{\boldsymbol{B}} = \mu\tilde{\boldsymbol{F}} & \text{on the interior of } V \\ \partial_t\tilde{\boldsymbol{B}} = \mu\tilde{\boldsymbol{G}} & \text{on } S \end{cases}$$

where equality only occurs in this case if both $\tilde{\boldsymbol{F}} = 0$ and $\tilde{\boldsymbol{G}} = 0$. It is straightforward to extend the iteration by

$$\frac{\partial\tilde{\boldsymbol{B}}}{\partial t} = \mu\tilde{\boldsymbol{G}}, \tag{3.13}$$

on the open boundaries. Equation (3.13) changes the boundary values in such way that $\mathcal{L}_\omega$ decreases. Discretized versions of Eqs. (3.9), together with appropriate boundary conditions, form the basis for the numerical scheme.

In this work, we have used computational box V of wedge-shaped volume, which includes an inner physical domain V' and a buffer zone(the region outside the physical domain) as shown in Fig. 3.2. The physical domain V' is a wedge-shaped volume, with two latitudinal boundaries at $\theta_1 = \theta_{\min}$ and $\theta_2 = \theta_{\max}$, two longitudinal boundaries at $\phi_1 = \phi_{\min}$ and $\phi_2 = \phi_{\max}$, and two radial boundaries at the photosphere ($r = 1R_\odot$) and $r =$

$1.5R_\odot$. The idea is to define an interior physical region V' in which we wish to calculate the magnetic field so that it fulfills the force-free or MHS equations. We define V' to be an inner region of V (including the photosphere) with $\omega = 1$ everywhere including its six inner boundaries $\partial V'$. We use the position-dependent weighting function to introduce a buffer boundary of nd grid points towards the side and top boundaries of the computational box, V. The weighting function, ω declines from unity at the boundary ∂V to 0 at the boundary $\partial V'$ with a cosine profile in the buffer boundary region.

For $\omega(r, \theta, \phi) = 1$, the optimization method requires that the magnetic field is given on all six boundaries of V'. This causes a serious limitation of the method because these data are only available for model configurations. For the reconstruction of the coronal magnetic field, it is necessary to develop a method that reconstructs the magnetic field only from data on the bottom boundary (Wiegelmann 2004). Since only the bottom boundary is measured, one has to make assumptions about the lateral and top boundaries, e.g., assume a potential field. This may lead to inconsistent boundary conditions (see Aly 1989, regarding the compatibility of photospheric vector magnetograph data). With the help of the weighting function, the five inconsistent boundaries are replaced by boundary layers and we consequently obtain more flexible boundaries around the physical domain that will be adjusted automatically during the iteration. This diminishes the effect of the top and lateral boundaries on the magnetic field solution inside the computational box. Additionally, the influence of the boundaries is diminished, the farther we move them away from the region of interest.

The theoretical deviation of the iterative Eq. (3.9) as outlined by Wheatland et al. (2000) does not depend on the use of a specific coordinate system. Previous numerical implementations of the optimization procedure in spherical geometry were demonstrated by Wiegelmann (2007) for the full sphere. Within this work, we use a spherical geometry, but for only a limited part of the sphere, e.g., large active regions, several (magnetically connected) active regions and full disc computations. Full disc vector magnetograms are available from SDO/HMI and SOLIS/VSM. Larger computational box will become necessary when the observed photospheric vector magnetogram becomes available for only parts of the photosphere.

3.1.2 Discretizing and implementing the method

The code uses non-uniform spherical grid r, θ, ϕ with n_r, n_θ, n_ϕ grid points in the direction of radius, latitude, and longitude, respectively. A finite difference scheme has been used to discetize the problem over discrete nodal points [see, the details of the finite difference scheme used in this work in Appendix A.2]. We normalize the magnetic field with the average radial magnetic field on the photosphere and the length scale with a solar radius.

The method works as follows:

- ✪ Compute an initial source surface potential field in the computational domain from $r = 1R_\odot$ to S_s using B_r in the photosphere at $r = 1R_\odot$ as input. The computation is performed by assuming that a currentless ($\boldsymbol{J} = 0$ or $\nabla \times \boldsymbol{B} = 0$) approximation holds between the photosphere and some spherical surface S_s (source surface where the magnetic field vector is assumed radial). We computed the solution of this boundary-value problem in a standard form of harmonic expansion in terms of eigen-solutions of the Laplace equation written in a spherical coordinate system, (r, θ, ϕ) [see section 2.2 of this thesis].

- The code replaces B_θ and B_ϕ at the bottom photospheric boundary at $r = 1R_\odot$ with bottom boundary vector magnetogram. The outer radial and lateral boundaries are unchanged from the initial potential field model. For the purpose of code testing, we also tested different boundary conditions (see next section).
- Iterate for a force-free magnetic field in the computational box by minimizing the functional $\mathcal{L}_\omega$ of Eq.(3.1) by applying Eq.(3.9). For each iteration step (k), the vector field $\tilde{\boldsymbol{F}}^{(k)}$ is calculated from the known field $\boldsymbol{B}^{(k)}$, and a new field may simply be computed as $\boldsymbol{B}^{(k+1)} = \boldsymbol{B}^{(k)} + \mu\tilde{\boldsymbol{F}}^{(k)}\Delta t$ for sufficiently small Δt and μ.
- The continuous form of Eq.(3.9) ensures a monotonically decreasing functional $\mathcal{L}_\omega$. For finite time steps, this is also ensured if the iteration time step dt is sufficiently small. If $\mathcal{L}_\omega(t + dt) \geq \mathcal{L}_\omega(t)$, this step is rejected and we repeat this step with dt reduced by a factor of 2.
- After each successful iteration step, the code increase dt by a factor of 1.01 to ensure a time step as large as possible within the stability criteria. This ensures an iteration time step close to its optimum.
- The iteration stops if dt becomes too small. As a stopping criteria, we use $dt \leq 10^{-6}$.

3.1.3 Test case and application to ideal boundary conditions

3.1.3.1 Test case

To test the method, a known semi-analytic nonlinear solution is used. Low and Lou (1990) presented a class of axisymmetric nonlinear force-free fields with a multipolar character. The authors solved the Grad-Shafranov equation for axisymmetric force-free fields in spherical coordinates r, θ, and ϕ. The magnetic field can be written in the form

$$\boldsymbol{B} = \frac{1}{r\sin\theta}\left(\frac{1}{r}\frac{\partial A}{\partial\theta}\hat{\boldsymbol{e}}_r - \frac{\partial A}{\partial r}\hat{\boldsymbol{e}}_\theta + Q\hat{\boldsymbol{e}}_\phi\right), \tag{3.14}$$

where A is a flux function independent of ϕ and Q represents the ϕ-component of $\boldsymbol{B}$, here assumed to depend only on A. The flux function A satisfies the Grad-Shafranov equation

$$\frac{\partial^2 A}{\partial r^2} + \frac{1-\mu^2}{r^2}\frac{\partial^2 A}{\partial\mu^2} + Q\frac{dQ}{dA} = 0\,, \tag{3.15}$$

where $\mu = \cos\theta$. Low and Lou (1990) derive solutions for

$$\frac{dQ}{dA} = \alpha, \tag{3.16}$$

by looking for separable solutions of the form

$$A(r, \theta) = \frac{P(\mu)}{r^n} \tag{3.17}$$

$$Q(A) = aA^{1+1/n} \tag{3.18}$$

where a and n are constants and the scalar function P satisfies the nonlinear differential equation:

$$(1-\mu^2)\frac{d^2P}{d\mu^2} + n(n+1)P + a^2\frac{1+n}{n}P^{1+2/n} = 0 \tag{3.19}$$

Equation (3.19) is not exactly the Legendre differential equation because of the third term which is not derivative of P with respect to μ. Let us demand that the magnetic field vanishes at $r' \to \infty$, which is ensured by the forms of A and Q given by Eqs. (3.17) and (3.18) with n taken as positive, and is well behaved along the axis of symmetry except at the origin. The latter condition requires the B_θ and B_ϕ vanish along the axis $\mu = 1, -1$, which by equations (3.14), (3.17) and (3.18) implies that

$$P = 0 \quad \text{at} \quad \mu = -1,\ 1 \tag{3.20}$$

The solution to the boundary-value problem posed by equations (3.19) and (3.20) generate the force-free fields we seek (see Low and Lou 1990, for detailed description). Not all prescriptions of the free constants a and n lead to a solution of equation (3.19) satisfy the boundary condition (3.20) we have an eigenvalue problem to which we now turn our attention. For instance, the case $a = 0$ corresponds to a potential field with $\alpha = 0$, which we are not interested in.

Low and Lou (1990) suggested that these field solutions are ideal solution for testing methods of reconstructing force-free fields from boundary values. They have become a standard test for nonlinear force-free extrapolation codes in cartesian geometry (Amari et al. 1999, 2006, Wheatland et al. 2000, Wiegelmann and Neukirch 2003, Yan and Li 2006, Inhester and Wiegelmann 2006, Schrijver et al. 2006). For that purpose, the origion of the spherical coordinate system is placed outside the computational box to avoid the singularity of the solution and the symmetry axis is tilted obliquely by $\Phi = \pi/10$ to the edges of the computational box.

Here we use the Low and Lou solution for $n = 1$ and $m = 1$ where $P_{1,1}$ is the associate Legendre function of the first kind. The original equilibrium is invariant in ϕ (azimuth angle the coordinate system), but we can produce a Φ-variation in our coordinate system by placing the origin of the solution at $l = 0.25$ solar radii from the Sun centre (see Low and Lou 1990, for detailed equations of transformation). The corresponding configuration is then no longer symmetric in ϕ with respect to the solar surface, as seen in the magnetic field map in the top row of Fig. 3.5, which shows the three components B_r, B_θ, and B_ϕ in the photosphere, respectively. Fig. 3.3a) shows the magnetic field configuration that has been generated using this method. We remark that we use the solution only for the purpose of testing our code and the equilibrium is not assumed to be a realistic model for the coronal magnetic field. We do the test runs on spherical grids (r, θ, ϕ) of $20 \times 48 \times 62$ and $40 \times 96 \times 124$ grid points.

3.1.3.2 Figures of merit

In order to judge the accuracy of an extrapolation method, we apply it to the above test case. The comparison between the calculated field and the reference field will give information about the quality of the extrapolation method. To quantify the degree of agreement between the vector field $\boldsymbol{B}$ (for the model field, which is used as a reference to test the code) and $\boldsymbol{b}$ (the NLFF model solutions derived from boundary field extracted from $\boldsymbol{B}$) specified on identical sets of grid points, we use five metrics that compare either local characteristics (e.g., vector magnitudes and directions at each point) or the global energy content in addition to the force and divergence integrals as defined in Schrijver et al. (2006). The vector correlation ($C_{\rm vec}$) metric generalizes the standard correlation coefficient for scalar functions given by

$$C_{\rm vec} = \frac{\sum_i \boldsymbol{B}_i \cdot \boldsymbol{b}_i}{\sqrt{\sum_i |\boldsymbol{B}_i|^2}\sqrt{\sum_i |\boldsymbol{b}_i|^2}}, \tag{3.21}$$

where $\boldsymbol{B}_i$ and $\boldsymbol{b}_i$ are the vectors at each point grid i. If the vector fields are identical, then $C_{\rm vec} = 1$; if $\boldsymbol{B}_i \perp \boldsymbol{b}_i$, then $C_{\rm vec} = 0$.

The second metric, $C_{\rm CS}$ is based on the Cauchy-Schwarz inequality($|\boldsymbol{a} \cdot \boldsymbol{b}| \leq |\boldsymbol{a}||\boldsymbol{b}|$ for any vector $\boldsymbol{a}$ and $\boldsymbol{b}$)

$$C_{\rm CS} = \frac{1}{N}\sum_i \frac{\boldsymbol{B}_i \cdot \boldsymbol{b}_i}{|\boldsymbol{B}_i||\boldsymbol{b}_i|}, \tag{3.22}$$

where N is the number of vectors in the field. This metric is mostly a measure of the angular differences between the vector fields: $C_{\rm CS} = 1$, when $\boldsymbol{B}$ and $\boldsymbol{b}$ are parallel, and $C_{\rm CS} = -1$, if they are anti-parallel; $C_{\rm CS} = 0$, if $\boldsymbol{B}_i \perp \boldsymbol{b}_i$ at each point.

We use two measures of the vector errors, one normalized to the average vector norm, one averaging over relative differences. The normalized vector error E_N is defined as

$$E_{\rm N} = \sum_i |\boldsymbol{b}_i - \boldsymbol{B}_i| / \sum_i |\boldsymbol{B}_i|, \tag{3.23}$$

The mean vector error E_M is defined as

$$E_{\rm M} = \frac{1}{N}\sum_i \frac{|\boldsymbol{b}_i - \boldsymbol{B}_i|}{|\boldsymbol{B}_i|}, \tag{3.24}$$

Unlike the first two metrics, perfect agreement between the two vector fields results in $E_M = E_N = 0$.
Since we are also interested in determining how well the models estimate the energy contained in the field, we use the total magnetic energy in the model field normalized to the total magnetic energy in the reference field as a global measure of the quality of the fit

$$\epsilon = \frac{\sum_i |\boldsymbol{b}_i|^2}{\sum_i |\boldsymbol{B}_i|^2}, \tag{3.25}$$

where $\epsilon = 1$ for closest agreement between the model field and the nonlinear force-free model solutions.

3.1.3.3 Application to ideal boundary conditions

The code has been used for different kind of boundary conditions extracted from the Low and Lou model magnetic field.

- Case 1: The boundary fields are specified on V'(all the six boundaries $\partial V'$ of V').

- Case 2: The boundary fields are only specified on the photosphere (the lower boundary of the physical domain V') and V & V' are identical (no buffer zone, see Fig. 3.2).

- Case 3: The boundary fields are only specified on the photosphere (the lower boundary of the physical domain V') and with boundary layers (at the buffer zone) of $nd = 6$ grid points toward top and lateral boundaries of the computational box V (see Fig. 3.2).

For the boundary conditions in case 1, the field line plot (as shown in Fig. 3.3) agrees with original Low and Lou reference field because the optimization method is constrained by boundary conditions on all boundaries of the computational volume. This shows that the code was technically correct in returning the right answer if fed by consistent and complete boundary conditions.

For the boundary conditions in case 2, we used an optimization code without a weighting function ($nd = 0$) and with a photospheric boundary. Here the boundaries of the physical domain coincide with the computational boundaries. The lateral and top boundaries assume the value of the initial potential field during the iteration. Some low-lying field lines are represented quite well (right-hand picture in Fig. 3.3 second row). The (observed) bottom boundary has a higher influence on these fields here than the lateral and top boundary. Other field lines, especially high-reaching field lines, deviate from the analytic solution because they feel the influence of the lateral and top boundaries which were fixed to the wrong potential field values.

For the boundary condition in case 3, we implemented an optimization code with a weighting function of $nd = 6$ grid points outside the physical domain. This reduces the effect of top and lateral boundaries where $\boldsymbol{B}$ is unknown as ω drops from 1 to 0 outward across the boundary layer around the physical domain. In this work, our physical domain V' is a wedge-shaped volume, with two latitudinal boundaries at $\theta_{\min} = 20°$ and $\theta_{\max} = 160°$, two longitudinal boundaries at $\phi_{\min} = 90°$ and $\phi_{\max} = 270°$, and two radial boundaries at the photosphere ($r = 1R_{\odot}$) and $r = 2R_{\odot}$.

The comparison of the field lines of the Low & Lou model field with the reconstructed field of case 3 (the last picture in Fig. 3.3) shows that the quality of the reconstruction improves significantly with the use of the weighting function. Additionally, the size and shape of a boundary layer influences the quality of the reconstruction (Wiegelmann 2004) for cartesian geometry. The larger computational box displaces the lateral and top boundary further away from the physical domain and its influence on the solution consequently decreases. As a result, the magnetic field in the physical domain is dominated by the vector magnetogram data, which is exactly what is required for application to measured vector magnetograms. A potential field reconstruction obviously does not agree with the reference field. In particular, we are unable to compute the magnetic energy content of the coronal magnetic field to be approximately correct. The figures of merit show that the potential field is far away from the true solutions and contains only 67.6% of the magnetic energy. The degree of convergence towards a force-free and divergence-free model solution can be quantified by the integral measures of the Lorentz force and divergence terms

Table 3.1: Quality of our reconstructions with several figures of merit as explained in section 3.2. We compute the figures for the three different cases along with the model reference field and potential field.

Model	$\mathcal{L}_\omega$	$\mathcal{L}_\mathrm{f}$	$\mathcal{L}_\mathrm{d}$	$\Vert \nabla \cdot \boldsymbol{B} \Vert_\infty$	$\Vert \boldsymbol{J} \times \boldsymbol{B} \Vert_\infty$	C_vec	C_CS	E_N	E_M	ϵ	Steps	Time
	Spherical grid (r, θ, ϕ) $20 \times 48 \times 62$											
Original	0.029	0.015	0.014	1.180	1.355	1	1	0	0	1		
Potential	0.020	0.007	0.014	1.706	1.091	0.736	0.688	0.573	0.535	0.676		
Case 1	0.006	0.004	0.002	0.454	0.774	0.999	0.983	0.012	0.016	1.005	10000	7.14 min
Case 2	33.236	7.806	25.430	47.843	24.135	0.757	0.726	0.397	0.451	0.745	110	1.28 min
Case 3	0.009	0.006	0.03	0.367	0.787	0.994	0.967	0.187	0.097	0.989	12011	17.54 min
	Spherical grid (r, θ, ϕ) $40 \times 96 \times 124$											
Original	0.005	0.003	0.002	0.38	0.71	1	1	0	0	1		
Potential	0.30	0.0003	0.30	0.44	0.23	0.67	0.77	0.70	0.67	0.75		
Case 1	0.002	0.001	0.0006	0.38	0.32	0.998	0.999	0.004	0.007	1.001	12522	1h 21min
Case 2	26.27	10.20	16.07	20.40	30.53	0.799	0.759	0.411	0.456	0.798	5673	1h 1min
Case 3	0.24	0.20	0.04	0.630	0.747	0.996	0.971	0.186	0.112	0.996	12143	4h 57min

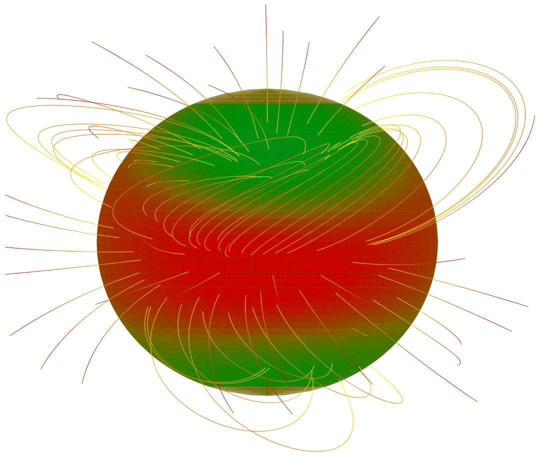

(a) Original

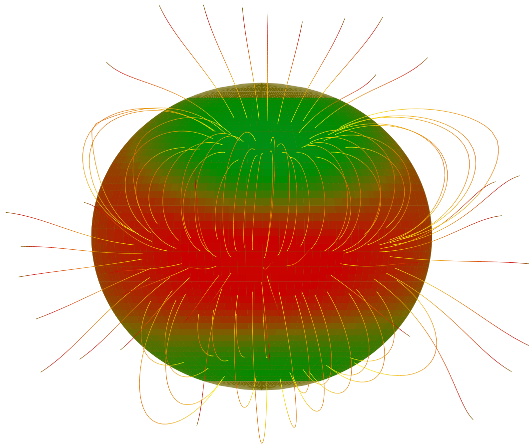

(b) Potential

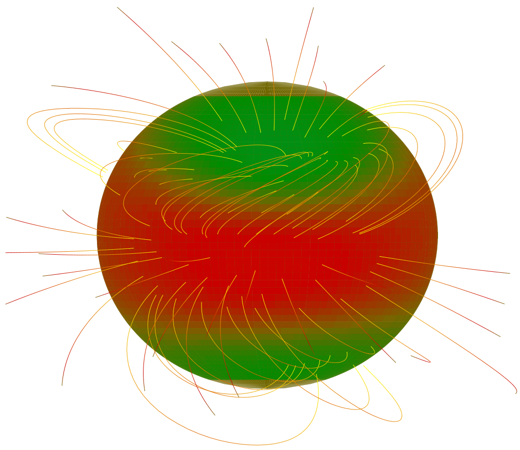

(c) Case 1

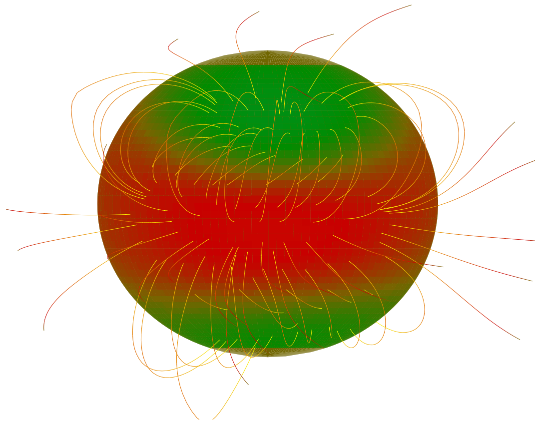

(d) Case 2

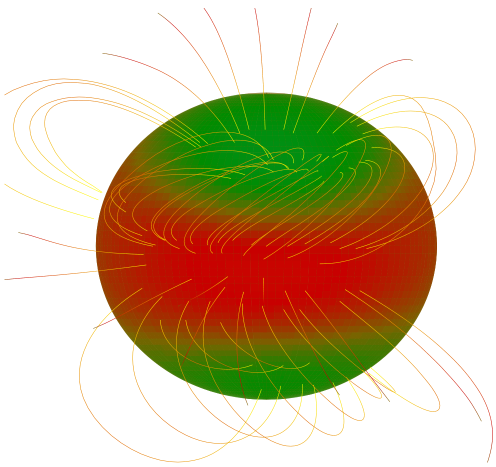

(e) Case 3

Figure 3.3: The figure shows the original reference field, a potential field, and the results of a nonlinear force-free reconstruction with different boundary conditions (case 1-3, see text). The color coding shows B_r on the photosphere and the disc centre corresponds to 180° longitude.

in the minimization functional in Eq. (3.1), computed over the entire model volume V:

$$\mathcal{L}_{\rm f} = \int_V \omega(r,\theta,\phi) B^{-2} \left|(\nabla \times \boldsymbol{B}) \times \boldsymbol{B}\right|^2 r^2 \sin\theta \, dr \, d\theta \, d\phi,$$

$$\mathcal{L}_{\rm d} = \int_V \omega(r,\theta,\phi) \left|\nabla \cdot \boldsymbol{B}\right|^2 r^2 \sin\theta \, dr \, d\theta \, d\phi,$$

$$\mathcal{L}_\omega = \mathcal{L}_{\rm f} + \mathcal{L}_{\rm d},$$

where $\mathcal{L}_{\rm f}$ and $\mathcal{L}_{\rm d}$ measure how well the force-free and divergence-free conditions are fulfilled, respectively. In Table 3.1, we list the figures of merit for our extrapolation results as introduced in previous section. Column 1 indicates the corresponding test case. Columns 2 – 4 show how well the force and solenoidal condition are fulfilled, where Col. 2 contains the value of the functional $\mathcal{L}_\omega$ as defined in Eq.(3) and $\mathcal{L}_{\rm f}$ and $\mathcal{L}_{\rm d}$ in Cols. 3 and 4 correspond to the first (force-free) and second (solenoidal free) part of $\mathcal{L}_\omega$. The evolution of the functional $\mathcal{L}_\omega$, $|\boldsymbol{J}\times\boldsymbol{B}|$, and $|\nabla\cdot\boldsymbol{B}|$ during the optimization process is shown in Fig. 3.4. One can see from this figure that the calculation does not converge for case 2, because of the problematic top and lateral boundary values which were set to the values of the equivalent potential field. Column 5 contains the $\mathcal{L}^\infty$ norm of the divergence of the magnetic field

$$\| \nabla \cdot \boldsymbol{B} \|_\infty = \sup_{\mathbf{x}\in V} |\nabla \cdot \boldsymbol{B}|$$

and Col. 6 lists the $\mathcal{L}^\infty$ norm of the Lorentz force of the magnetic field

$$\| \boldsymbol{J} \times \boldsymbol{B} \|_\infty = \sup_{\mathbf{x}\in V} |\boldsymbol{J} \times \boldsymbol{B}|.$$

The next five columns of Table 3.1 contain different measurements comparing our reconstructed field with the semi-analytic reference field. The two vector fields agree perfectly if $C_{\rm vec}$, $C_{\rm CS}$, and ϵ are unity and if $E_{\rm N}$ and $E_{\rm M}$ are zero. Column 12 contains the number of iteration steps until convergence, and Col. 13 shows the computing time on 1 processor.

A comparison of the original reference field (Fig. 3.3(a)) with our nonlinear force-free reconstructions (cases 1-3) shows that the magnetic field line plots agree with the original for case 1 and case 3 within the plotting precision. Case 2 shows some deviations from the original, but the reconstructed field lines are much closer to the reference field than the initial potential field. The visual inspection of Fig. 3.3 is supported by the quantitative criteria shown in Table 3.1. For case 1 and case 3 the formal force-free criteria ($\mathcal{L}_\omega$, $\mathcal{L}_{\rm f}$, $\mathcal{L}_{\rm d}$) are smaller than the discretization error (see Column 2 of Table 3.1) of the analytic solution and the comparison metrics show almost perfect agreement with the reference field. The comparison metrics (of Table 3.1) show that there is a discrepancy between the reference field and case 2 as the magnetic field solution is affected by the nearby problematic top and lateral boundaries. In Fig. 3.3 we compare magnetic field line plots of the original model field with a corresponding potential field and nonlinear force-free reconstructions with different boundary conditions (case 1 - case 3). The colour coding shows the radial magnetic field in the photosphere, as also shown in the magnetogram in Fig. 3.5(a). The images show the results of the computation on the $20 \times 48 \times 62$ grid.

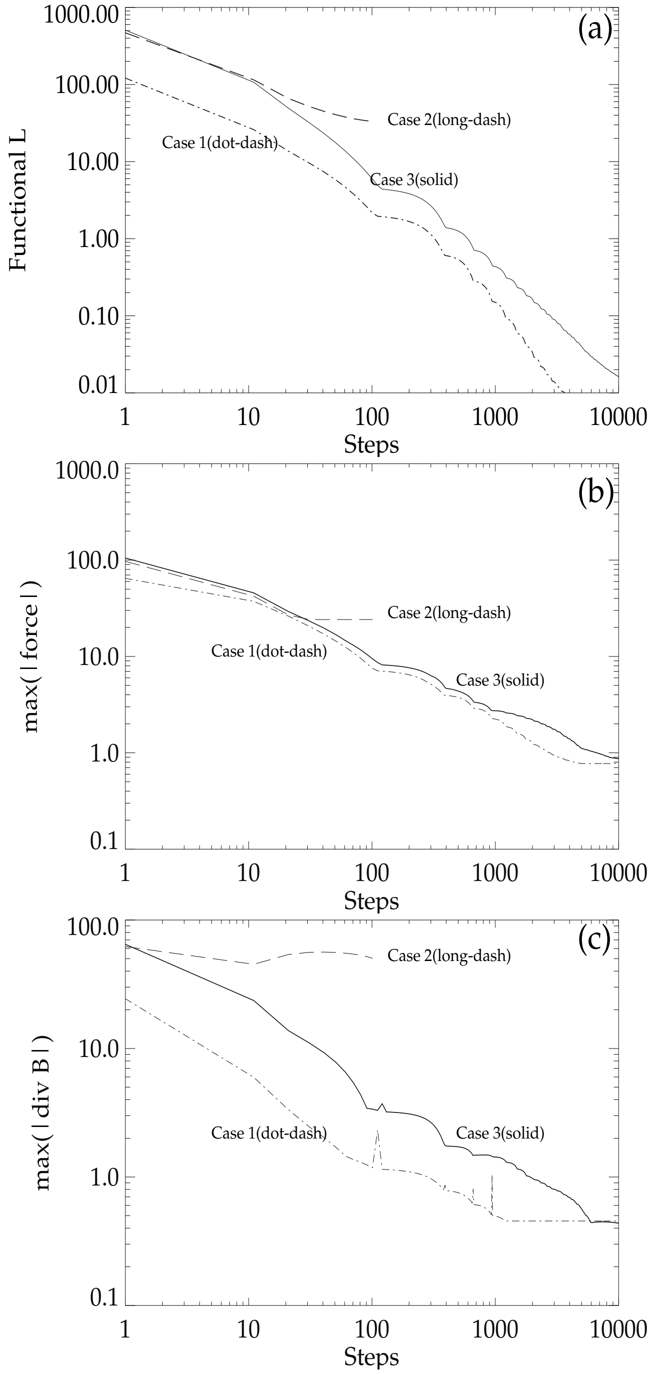

Figure 3.4: Evolution of $\mathcal{L}_\omega$ (as defined in Eq. 3), max(|force|), and max(|div B|) during the optimization process. The solid line corresponds to case 3, the dash-dotted line to case 1, the long-dashed line to case 2.

3.2 Preprocessing procedure in spherical geometry

It has been already mentioned that the magnetic field is not force-free in either the photosphere or the lower chromosphere (with the possible exception of sunspot areas, where the field is exceptionally strong). Furthermore, measurement errors, in particular for the transverse field components (eg. perpendicular to the line of sight of the observer), will destroy the compatibility of a magnetogram with the condition of being force-free. One way to ease these problems is to preprocess the magnetograph data as suggested by Wiegelmann et al. (2006). The vector components of the total magnetic force and the total magnetic torque on the volume considered are given by six boundary integrals that must vanish if the magnetic field is force-free in the full volume (Molodensky 1969, Aly 1984, 1989, Low 1985). The preprocessing changes the boundary values of $\boldsymbol{B}$ within the error margins of the measurement in such a way that the moduli of the six boundary integrals are minimized. The resulting boundary values are expected to be more suitable for an extrapolation into a force-free field than the original values. In the practical calculations, the convergence properties of the preprocessing iterations, as well as the calculated fields themselves, are very sensitive to small-scale noise and apparent discontinuities in the photospheric magnetograph data. This problem should, in principle, disappear if small spatial scales were sufficiently resolved. However, the numerical effort for that would be enormous. The small-scale fluctuations in the magnetograms are also presumed to affect the solutions only in a very thin boundary layer close to the photosphere (Fuhrmann et al. 2007). Therefore, smoothing of the data is included in the preprocessing.

In this work, we develop a spherical version of both the preprocessing and the optimization code for restricted parts of the Sun (not full sphere, but relatively larger area which could accommodate multi-active regions). We follow the suggestion of Wiegelmann et al. (2006) and generalize their method of preprocessing photospheric vector magnetograms to spherical geometry just by considering the curvature of the Sun's surface for larger fields of view. We derive force-free consistency criteria and describe the preprocessing procedure in spherical geometry in next subsections. For testing, we use a known semi-analytic force-free model and apply the method to different noise models. We also investigate first ideal model data and later data that contain artificial noise. To deal with noisy data and data with other uncertainties, we developed a preprocessing routine in spherical geometry. While preprocessing does not model the details of the interface between the forced photosphere and the force-free base of the solar corona the procedure helps us to find suitable boundary conditions for a force-free modelling from measurements with inconsistencies.

3.2.1 Boundary consistency criteria in spherical geometry

A more fundamental requirement of the boundary data is its consistency with the force-free field approximation. As shown by Molodensky (1969) and Aly (1989), a balance between the total momentum and angular momentum exerted onto the numerical box in cartesian geometry by the magnetic field leads to a set of boundary integral constraints on the magnetic field. These constraints should also be satisfied on the solar surface for the field at the coronal base in the vicinity of a sufficiently isolated magnetic region and in a situation where there is no rapid dynamical development. As explained in detail in

Molodensky (1974), the sense of these relations is that on average a force-free field cannot exert a net tangential force on the boundary or shear stresses along axes lying along the boundary. In summary, the boundary data for the force-free extrapolation should fulfill the following conditions:

1. The boundary data should coincide with the photospheric observations within measurement errors.

2. The boundary data should be consistent with the assumption of a force-free magnetic field in the corona above the photosphere where the magnetic field is measured.

3. For computational reasons (finite differences), the boundary data should be sufficiently smooth.

Additional a-priori assumption is about the photospheric data are that the magnetic flux from the photosphere is sufficiently distant from the boundaries of the observational domain and that the net flux is balanced[2], i.e.,

$$\int_S B_r(r = 1R_s, \theta, \phi) d\Omega = 0, \tag{3.26}$$

where S is the area of a bottom boundary of the physical domain on the photosphere.

Generally, the flux balance criterion must be applied to the entire, closed surface of the numerical box. However, we can only measure the magnetic field vector on the bottom photospheric boundary and the contributions of the lateral and top boundary remain unspecified. However, if a major part of the known flux from the bottom boundary is uncompensated, the final force-free magnetic field solution will depend markedly on how the uncompensated flux is distributed over the other five boundaries. This will result in a major uncertainty on the final force free magnetic field configuration. We therefore demand that the flux balance is satisfied with the bottom data alone (Wiegelmann and Inhester 2006). If this is not the case, we classify the reconstruction problem as not being uniquely solvable within the given box. Aly (1989) used the virial theorem to define the conditions that a vector magnetogram must fulfill to be consistent with the assumption of a force-free field above in cartesian geometry. Let us formulate the force-free and torque-free conditions for spherical geometry as in Sakurai (1994).

Integrated forms of the equation for the free-force magnetic fields were summarized by Aly (1989, 1988). The Lorentz force is

$$\boldsymbol{F} = \frac{1}{4\pi}(\nabla \times \boldsymbol{B}) \times \boldsymbol{B} \tag{3.27}$$

[2]The positive and negative flux within the domain should be balanced so that the net flux is zero. The need for flux balance is not mathematical requirement but, imbalance of flux in a region implies the existence of compensating flux outside. Therefore, the flux imbalance means that the spatial coverage of the data itself is incomplete for the problem to be solved, and it will necessarily lead to an incorrect results.

where $\boldsymbol{B}$ is the magnetic field vector. By integrating Eq. (3.27) over a volume V surrounded by a surface S one can obtain a global force-balance equation.

$$\int_V \boldsymbol{F} dV = \int_V (\nabla \times \boldsymbol{B}) \times \boldsymbol{B} dV = 0 \tag{3.28}$$

But using the vector identity

$$\nabla(\boldsymbol{A} \cdot \boldsymbol{B}) = \boldsymbol{A} \times (\nabla \times \boldsymbol{B}) + \boldsymbol{B} \times (\nabla \times \boldsymbol{A}) + (\boldsymbol{A} \cdot \nabla)\boldsymbol{B} + (\boldsymbol{B} \cdot \nabla)\boldsymbol{A} \tag{3.29}$$

Where if $\boldsymbol{A} = \boldsymbol{B}$, the identity reduces to

$$(\nabla \times \boldsymbol{B}) \times \boldsymbol{B} = -\nabla(\frac{1}{2}B^2) + (\boldsymbol{B} \cdot \nabla)\boldsymbol{B} \tag{3.30}$$

Substituting equation (3.30) into equation (3.28) and using Gauss divergence theorem one can find,

$$\frac{1}{2}\int_S B^2 d\boldsymbol{S} - \int_S (\boldsymbol{B} \cdot d\boldsymbol{S})\boldsymbol{B} = 0 \tag{3.31}$$

The vector $d\boldsymbol{S}$ is directed into the volume V. We will consider the equation described above in spherical polar coordinates (r, θ, ϕ), with usual axes. The volume V is space outside of a sphere of radius $R_\odot$ and the origin of the vector $\boldsymbol{r}$ is at the center of the sphere (Sun). With $d\boldsymbol{S} = ds\hat{\boldsymbol{e}}_r$ and $ds = R_\odot^2 \sin\theta d\theta d\phi$
The force balance equation (3.31) is still valid if S is spherical surface. For magnetic field vector,

$$\boldsymbol{B} = B_r\hat{\boldsymbol{e}}_r + B_\theta\hat{\boldsymbol{e}}_\theta + B_\phi\hat{\boldsymbol{e}}_\phi$$

with

$$\boldsymbol{B} \cdot d\boldsymbol{S} = B_r ds$$

equation (3.31) can be written as

$$\int_S \frac{1}{2}(B_r^2 + B_\theta^2 + B_\phi^2)d\boldsymbol{S} - \int_S B_r ds(B_r\hat{\boldsymbol{e}}_r + B_\theta\hat{\boldsymbol{e}}_\theta + B_\phi\hat{\boldsymbol{e}}_\phi) = 0 \tag{3.32}$$

Notice that the spherical unit vectors vary over S. For the numerical evaluation, we therefore calculate the cartesian components of Eq. (3.32). One can derive the force and torque balance equations for the three components as the following: For force-balance condition along x-axis, we have

$$\int_{r>R_\odot} F_x dV = 0$$

Multiplying equation (3.32) by $\hat{\boldsymbol{e}}_x$

$$\hat{\boldsymbol{e}}_x \cdot \Big[\int_S \frac{1}{2}(B_r^2 + B_\theta^2 + B_\phi^2)d\boldsymbol{S} - \int_S B_r ds(B_r\hat{\boldsymbol{e}}_r + B_\theta\hat{\boldsymbol{e}}_\theta + B_\phi\hat{\boldsymbol{e}}_\phi)\Big] = 0$$

With the spherical unit vectors

$$\hat{\boldsymbol{e}}_r = \sin\theta\cos\phi\hat{\boldsymbol{e}}_x + \sin\theta\sin\phi\hat{\boldsymbol{e}}_y + \cos\theta\hat{\boldsymbol{e}}_z$$

$$\hat{\boldsymbol{e}}_\theta = \cos\theta\cos\phi\hat{\boldsymbol{e}}_x + \cos\theta\sin\phi\hat{\boldsymbol{e}}_y - \sin\theta\hat{\boldsymbol{e}}_z$$

$$\hat{\boldsymbol{e}}_\phi = -\sin\phi\,\hat{\boldsymbol{e}}_x + \cos\phi\hat{\boldsymbol{e}}_y$$

, and hence

$$\hat{\boldsymbol{e}}_x \cdot \hat{\boldsymbol{e}}_r = \sin\theta\cos\phi$$

$$\hat{\boldsymbol{e}}_x \cdot \hat{\boldsymbol{e}}_\theta = \cos\theta\cos\phi$$

$$\hat{\boldsymbol{e}}_x \cdot \hat{\boldsymbol{e}}_\phi = -\sin\phi$$

Using those conditions one can arrive at

$$\int_S \Big[\frac{1}{2}(B_\theta^2 + B_\phi^2 - B_r^2)\sin\theta\cos\phi - B_rB_\theta\cos\theta\cos\phi + B_rB_\phi\sin\phi\Big]d\Omega = 0 \tag{3.33}$$

Similarly for force-balance condition along y-component

$$\int_{r>R_\odot} F_y dV = 0$$

$$\hat{\boldsymbol{e}}_y \cdot \Big[\int_S \frac{1}{2}(B_r^2 + B_\theta^2 + B_\phi^2)d\boldsymbol{S} - \int_S B_r ds(B_r\hat{\boldsymbol{e}}_r + B_\theta\hat{\boldsymbol{e}}_\theta + B_\phi\hat{\boldsymbol{e}}_\phi)\Big] = 0$$

where

$$\hat{\boldsymbol{e}}_y \cdot \hat{\boldsymbol{e}}_r = \sin\theta\sin\phi$$

$$\hat{\boldsymbol{e}}_y \cdot \hat{\boldsymbol{e}}_\theta = \cos\theta\sin\phi$$

$$\hat{\boldsymbol{e}}_y \cdot \hat{\boldsymbol{e}}_\phi = \cos\phi$$

Using those conditions one can arrive at

$$\int_S \Big[\frac{1}{2}(B_\theta^2 + B_\phi^2 - B_r^2)\sin\theta\sin\phi - B_rB_\theta\cos\theta\sin\phi - B_rB_\phi\cos\phi\Big]d\Omega = 0 \tag{3.34}$$

For force-balance condition along z-axis

$$\int_{r>R_\odot} F_z dV = 0$$

where

$$\hat{\boldsymbol{e}}_z \cdot \hat{\boldsymbol{e}}_r = \cos\theta$$

$$\hat{\boldsymbol{e}}_z \cdot \hat{\boldsymbol{e}}_\theta = -\sin\theta$$

$$\hat{\boldsymbol{e}}_z \cdot \hat{\boldsymbol{e}}_\phi = 0$$

$$\int_S \Big[\frac{1}{2}(B_\theta^2 + B_\phi^2 - B_r^2)\cos\theta + B_rB_\theta\sin\theta\Big]d\Omega = 0 \tag{3.35}$$

These equations (3.33), (3.34) and (3.35) are in terms of Cartesian components of force.

For the torque balance equations, the volume integral of torque in the box must vanish.

$$\int_V (\boldsymbol{r} \times \boldsymbol{F}) dV = 0$$

Using Gauss divergence theorem this will reduce to

$$\int_V (\boldsymbol{r} \times \boldsymbol{F}) dV = \frac{1}{2} \int_S B^2 (\boldsymbol{r} \times d\boldsymbol{S}) - \int_S (\boldsymbol{r} \times \boldsymbol{B})(\boldsymbol{B} \cdot d\boldsymbol{S}) = 0$$

We have $\boldsymbol{r} = R_\odot \hat{\boldsymbol{e}}_r$, $(\boldsymbol{r} \times d\boldsymbol{S}) = 0$ and $(\boldsymbol{B} \cdot d\boldsymbol{S}) = B_r d\Omega$
The above equation reduces to

$$\int_S (\boldsymbol{r} \times \boldsymbol{B}) B_r d\Omega = 0 \tag{3.36}$$

Using the cross product

$$\boldsymbol{r} \times \boldsymbol{B} = 0\hat{\boldsymbol{e}}_r - R_\odot B_\phi \hat{\boldsymbol{e}}_\theta + R_\odot B_\theta \hat{\boldsymbol{e}}_\phi$$

then equation (3.36) can be written as

$$\int_S [-R_\odot B_\phi \hat{\boldsymbol{e}}_\theta + R_\odot B_\theta \hat{\boldsymbol{e}}_\phi] B_r d\Omega = 0 \tag{3.37}$$

Hence the torque balance along each components will be

$$\hat{\boldsymbol{e}}_x \cdot [\int_S (-R_\odot B_\phi \hat{\boldsymbol{e}}_\theta + R_\odot B_\theta \hat{\boldsymbol{e}}_\phi) B_r d\Omega] = 0$$

Which is actually reducing to

$$\int_S B_r (B_\phi \cos\theta \cos\phi + B_\theta \sin\phi) d\Omega = 0 \tag{3.38}$$

Similarly

$$\hat{\boldsymbol{e}}_y \cdot [\int_S (-R_\odot B_\phi \hat{\boldsymbol{e}}_\theta + R_\odot B_\theta \hat{\boldsymbol{e}}_\phi) B_r d\Omega] = 0$$

One can find

$$\int_S B_r (B_\phi \cos\theta \sin\phi - B_\theta \cos\phi) d\Omega = 0 \tag{3.39}$$

Finally

$$\hat{\boldsymbol{e}}_z \cdot [\int_S (-R_\odot B_\phi \hat{\boldsymbol{e}}_\theta + R_\odot B_\theta \hat{\boldsymbol{e}}_\phi) B_r d\Omega] = 0$$

One can find

$$\int_S B_r B_\phi \sin\theta d\Omega = 0 \tag{3.40}$$

1. The total force on the boundary has to vanish because force-free fields can, on average, not exert pressure on the photospheric boundary S and cannot induce shear stresses along axes parallel to the boundaries, i.e.

$$\mathcal{F}_1 = \int_S \Big[\frac{1}{2}(B_\theta^2 + B_\phi^2 - B_r^2)\sin\theta\cos\phi - B_r B_\theta \cos\theta\cos\phi + B_r B_\phi \sin\phi\Big] d\Omega = 0, \quad (3.41)$$

$$\mathcal{F}_2 = \int_S \Big[\frac{1}{2}(B_\theta^2 + B_\phi^2 - B_r^2)\sin\theta\sin\phi - B_r B_\theta \cos\theta\sin\phi - B_r B_\phi \cos\phi\Big] d\Omega = 0, \quad (3.42)$$

$$\mathcal{F}_3 = \int_S \Big[\frac{1}{2}(B_\theta^2 + B_\phi^2 - B_r^2)\cos\theta + B_r B_\theta \sin\theta\Big] d\Omega = 0 \quad (3.43)$$

2. The total torque on the boundary vanishes or force-free fields cannot induce rotational moments along the boundary

$$\mathcal{T}_1 = \int_S B_r(B_\phi \cos\theta\cos\phi + B_\theta \sin\phi) d\Omega = 0, \quad (3.44)$$

$$\mathcal{T}_2 = \int_S B_r(B_\phi \cos\theta\sin\phi - B_\theta \cos\phi) d\Omega = 0, \quad (3.45)$$

$$\mathcal{T}_3 = \int_S B_r B_\phi \sin\theta d\Omega = 0 \quad (3.46)$$

The relations (3.41) - (3.46) are always fulfilled for potential magnetic fields because of the vanishing electric currents ($\boldsymbol{J} = 0$) which could be created, e.g., by currents at one side of the plane S . However, if currents flow on either side of S both impulse and momentum can be transferred from one side to the other and the distribution of the field in the plane may not satisfy these relations (Molodensky 1974).

As with the flux balance, these criteria must in general, be applied to the entire surface of the numerical box. Since we assumed that the photospheric flux is sufficiently concentrated in the center and the net flux is in balance, we can expect the magnetic field on the lateral and top boundaries to remain weak and hence these surfaces do not represent a significant contribution to the integrals of the constraints above. We therefore impose the criteria on the bottom boundary alone. From this beginning, we use the following notation for simplicity:

$$E_B^- = \frac{1}{2}(B_\theta^2 + B_\phi^2 - B_r^2)\,,\ E_B = \int_S (B_r^2 + B_\theta^2 + B_\phi^2) d\Omega\,,$$

$$B_1 = B_\theta \cos\theta\cos\phi - B_\phi \sin\phi\,,\ B_2 = B_\theta \cos\theta\sin\phi + B_\phi \cos\phi\,,$$

$$B_3 = B_\phi \cos\theta\cos\phi + B_\theta \sin\phi\,,\ B_4 = B_\phi \cos\theta\sin\phi - B_\theta \cos\phi$$

To quantify the quality of the vector magnetograms with respect to the above criteria, we introduce three dimensionless parameters similar to those in Wiegelmann et al. (2006), but now for spherical geometry:

1. The flux balance parameter

$$\varepsilon_{\text{flux}} = \frac{\int_S B_r d\Omega}{\int_S |B_r| d\Omega}$$

2. The force balance parameter

$$\begin{aligned}\varepsilon_{\text{force}} &= \frac{|\mathcal{F}_1| + |\mathcal{F}_2| + |\mathcal{F}_2|}{E_B} \\ &= \Big(\Big|\int_S [E_B^- \sin\theta\cos\phi - B_r B_1]d\Omega\Big| + \Big|\int_S [E_B^- \sin\theta\sin\phi - B_r B_2]d\Omega\Big| \\ &\quad + \Big|\int_S [E_B^- \cos\theta + B_r B_\theta \sin\theta]d\Omega\Big|\Big)\Big/E_B\end{aligned}$$

3. The torque balance parameter

$$\begin{aligned}\varepsilon_{\text{torque}} &= \frac{|\mathcal{T}_1| + |\mathcal{T}_2| + |\mathcal{T}_2|}{E_B} \\ &= \Big(\Big|\int_S B_r B_3 d\Omega\Big| + \Big|\int_S B_r B_4 d\Omega\Big| + \Big|\int_S B_r B_\phi \sin\theta d\Omega\Big|\Big)\Big/E_B\end{aligned}$$

An observed vector magnetogram is then flux-balanced and consistent with the force-free assumption if: $\varepsilon_{\text{flux}} \ll 1$, $\varepsilon_{\text{force}} \ll 1$ and $\varepsilon_{\text{torque}} \ll 1$.

3.2.2 Numerics of the preprocessing procedure

The strategy of preprocessing is to define a functional L of the boundary values of $\boldsymbol{B}$, such that on minimizing L the total magnetic force and the total magnetic torque on the considered volume, as well as a quantity measuring the degree of small-scale noise in the boundary data, simultaneously become small. Each of the quantities to be made small is measured by an appropriately defined subfunctional included in L. The different subfunctionals are weighted to control their relative importance. Even if we choose a sufficiently flux balanced isolated active region ($\varepsilon_{\text{flux}} \ll 1$), we find that the force-free conditions $\varepsilon_{\text{force}} \ll 1$ and $\varepsilon_{\text{torque}} \ll 1$ are not usually fulfilled for measured vector magnetograms. We therefore conclude, that force-free extrapolation methods should not be used directly on observed vector magnetograms (see Gary (2001) for $\beta > 1$ in photosphere), particularly not on very noisy transverse photospheric magnetic field measurements. The large noise in the transverse components of the photospheric field vector, which is one order of magnitude higher than on the LOS-field (~the transverse B_θ and B_ϕ at the bottom boundary), provides us freedom to adjust these data within the noise level. We use this freedom to drive the data towards being more consistent with Aly's force-free and torque-free conditions.

The preprocessing scheme of Wiegelmann et al. (2006) involves minimizing a two-dimensional functional of quadratic form similar to the following:

$$L = \mu_1 L_1 + \mu_2 L_2 + \mu_3 L_3 + \mu_4 L_4 \tag{3.47}$$

Here we write the individual terms in spherical co-ordinates as:

$$
\begin{aligned}
L_1 &= \mathcal{F}_1^2 + \mathcal{F}_2^2 + \mathcal{F}_3^2 \\
&= \Big(\sum_p [E_B^- \sin\theta\cos\phi - B_r B_1]\sin\theta\Big)^2 + \Big(\sum_p [E_B^- \sin\theta\sin\phi \qquad (3.48)\\
&\quad - B_r B_2]\sin\theta\Big)^2 + \Big(\sum_p \big[E_B^- \cos\theta + B_r B_\theta \sin\theta\big]\sin\theta\Big)^2, \qquad (3.49)
\end{aligned}
$$

$$
\begin{aligned}
L_2 &= \mathcal{T}_1^2 + \mathcal{T}_2^2 + \mathcal{T}_3^2 \\
&= \Big(\sum_p B_r B_3 \sin\theta\Big)^2 + \Big(\sum_p B_r B_4 \sin\theta\Big)^2 + \Big(\sum_p B_r B_\phi \sin^2\theta\Big)^2, \qquad (3.50)
\end{aligned}
$$

$$L_3 = \sum_p (B_r - B_{r\mathrm{obs}})^2 + \sum_p (B_\theta - B_{\theta\mathrm{obs}})^2 + \sum_p (B_\phi - B_{\phi\mathrm{obs}})^2, \qquad (3.51)$$

$$L_4 = \sum_p \left[(\Delta B_r)^2 + (\Delta B_\theta)^2 + (\Delta B_\phi)^2\right] \qquad (3.52)$$

The surface integrals are replaced by a summation $\Big(\int_S d\Omega \to \Sigma_p \sin\theta\Delta\theta\Delta\phi$, omitting the constant $\Delta\theta\Delta\phi$ over all p grid nodes of the bottom surface grid, with an elementary surface of $\sin\theta\Delta\phi \times \Delta\theta\Big)$. The differentiation in the smoothing term (L_4) is achieved by the usual five-point stencil for the 2D-Laplace operator. Each of the constraints L_n is weighted by a yet undetermined factor μ_n. The first term ($n = 1$) corresponds to the force-balance condition, and the next ($n = 2$) to the torque-free condition. The following term ($n = 3$) ensures that the optimized boundary condition agrees with the measured photospheric data, and that the last term ($n = 4$) controls the smoothing. The 2D-Laplace operator is designated by Δ.

The aim of our preprocessing procedure is to minimize L so that all terms L_n, if possible, become small simultaneously. This will yield a surface magnetic field:

$$\boldsymbol{B}_{\mathrm{min}} = \mathrm{argmin}(L) \qquad (3.53)$$

Besides a dependence on the observed magnetogram, the solution in Eq.(3.47) now also depends on the coefficients μ_n. These coefficients are formaly necessary because the terms L_n represent different quantities. By means of these coefficients, however, we can also give more or less weight to the individual terms in the case where a reduction in one term opposes a reduction in another. This competition obviously exists between the observation term ($n = 3$) and the smoothing term ($n = 4$). The smoothing is performed consistently for all three magnetic field components.

To obtain Eq. (3.53) by iteration, we need the derivative of L with respect to each of the three field components at every node (q) of the bottom boundary grid. We have, however, taken into account that B_r is measured with much higher accuracy than B_θ and B_ϕ. This is achieved by assuming that the vertical component is invariable compared to horizontal components in all terms where mixed products of the vertical and horizontal field components occur, e.g., within the constraints (Wiegelmann et al. 2006). The relevant functional derivatives of L are therefore[3]

$$\begin{aligned}
\frac{\partial L}{\partial (B_\theta)_q} =& 2\mu_1 (B_\theta \sin^2\theta\cos\phi - B_r \sin\theta\cos\theta\cos\phi)_q \times \\
& \sum_p [E_B^- \sin\theta\cos\phi - B_r B_1] \sin\theta \\
& + 2\mu_1 (B_\theta \sin^2\theta\sin\phi - B_r\sin\theta\cos\theta\sin\phi)_q \times \\
& \sum_p [E_B^- \sin\theta\sin\phi - B_r B_2] \sin\theta \\
& + 2\mu_1 (B_\theta \sin\theta\cos\theta + B_r \sin^2\theta)_q \times \\
& \sum_p [E_B^- \cos\theta + B_r B_\theta \sin\theta] \sin\theta \\
& + 2\mu_2 \Big[(B_r \sin\theta\sin\phi)_q \sum_p B_r B_3 \sin\theta \\
& - (B_r \sin\theta\cos\phi)_q \sum_p B_r B_4 \sin\theta \Big] \\
& + 2\mu_3 (B_\theta - B_{\theta\mathrm{obs}})_q + 2\mu_4 (\Delta(\Delta B_\theta))_q,
\end{aligned} \tag{3.54}$$

$$\begin{aligned}
\frac{\partial L}{\partial (B_\phi)_q} =& 2\mu_1 (B_\phi \sin^2\theta\cos\phi + B_r \sin\theta\sin\phi)_q \times \\
& \sum_p [E_B^- \sin\theta\cos\phi - B_r B_1] \sin\theta \\
& + 2\mu_1 (B_\phi \sin^2\theta\sin\phi - B_r \sin\theta\cos\phi)_q \times \\
& \sum_p [E_B^- \sin\theta\sin\phi - B_r B_2] \sin\theta \\
& + 2\mu_1 (B_\phi \sin\theta\cos\theta)_q \sum_p [E_B^- \cos\theta + B_r B_\theta \sin\theta] \sin\theta \\
& + 2\mu_2 \Big[(B_r \cos\theta\cos\phi\sin\theta)_q \sum_p B_r B_3 \sin\theta \\
& + (B_r \cos\theta\sin\phi\sin\theta)_q \sum_p B_r B_4 \sin\theta \\
& + (B_r \sin^2\theta)_q \sum_p B_r B_\phi \sin^2\theta \Big] + 2\mu_3 (B_\phi - B_{\phi\mathrm{obs}})_q \\
& + 2\mu_4 (\Delta(\Delta B_\phi))_q,
\end{aligned} \tag{3.55}$$

$$\frac{\partial L}{\partial (B_r)_q} = 2\mu_3 (B_r - B_{r\mathrm{obs}})_q + 2\mu_4 (\Delta(\Delta B_r))_q \tag{3.56}$$

The optimization is performed iteratively by a simple Landweber iteration[4], which re-

[3] See Appendix A.2 for partial derivative of L_4 with respect to each of the three field components.

[4] Landweber iteration is the method used for finding successively better approximations to the zeroes (or roots) of a real-valued function.

places

$$(B_r)_q \longleftarrow (B_r)_q - \mu \frac{\partial L}{\partial (B_r)_q}, \tag{3.57}$$

$$(B_\theta)_q \longleftarrow (B_\theta)_q - \mu \frac{\partial L}{\partial (B_\theta)_q}, \tag{3.58}$$

$$(B_\phi)_q \longleftarrow (B_\phi)_q - \mu \frac{\partial L}{\partial (B_\phi)_q}, \tag{3.59}$$

at every step. The convergence of this scheme towards a solution of Eq. (3.47) is obvious: L has to decrease monotonically at every step as long as Eqs. (3.49)-(3.51) have a nonzero component and if μ is sufficiently small. These terms vanish only if an extremum of L is reached. Since L is fourth order in B, this may not necessarily be a global minimum; in rare cases, if the step size is handled carelessly, it may even be a local maximum. In practical calculation, this should not, however, be a problem and from our experience we rapidly obtain a minimum $\boldsymbol{B}_{\text{min}}$ of L, once the parameters μ_n are specified (Wiegelmann et al. 2006).

3.2.3 Tests with different noise-models

We extract the bottom boundary of the Low and Lou equilibrium and use it as input for our extrapolation code (see Wiegelmann 2004). This artificial vector magnetogram (see first row of Fig. 3.5) derived from a semi-analytical solution is of course in perfect agreement with the assumption of a force-free field above (Aly-criteria) and the result of our extrapolation code was in reasonable agreement with the original. Truely measured vector magnetograms are not ideal (and smooth) of course, and we simulate this effect by adding noise to the Low and Lou magnetogram (Wiegelmann et al. 2006). We add noise to this ideal solution in the form:

Noise model I:
$\delta B_i = n_l \cdot r_n \cdot \sqrt{B_i}$, where n_l is the noise level and r_n a random number in the range $-1....1$ with typical $B_i = 50$ Gauss. The noise level was chosen to be $n_l = 10.0$ for the transverse magnetic field (B_θ, B_ϕ) and $n_l = 0.5$ for B_r. This mimics a real magnetogram (see the middle row of Fig. 3.5) with Gaussian noise and significantly higher noise in the transverse components of the magnetic field.

Noise model II:
$\delta B_i = n_l \cdot r_n$, where n_l is the noise level and r_n a random number in the range $-1....1$. The noise level was chosen to be $n_l = 20.0$ for the transverse magnetic field (B_θ, B_ϕ) and $n_l = 1.0$ for B_r). This noise model adds noise, independent of the local magnetic field strength.

Noise model III:
$\delta B_r = \text{constant}$, $\delta B_t = \frac{\delta B_{t\min}^2}{\sqrt{B_t^2 + B_{t\min}^2}}$, where we choose a constant noise level δB_r of 1 and a minimum detection level $\delta B_{t\min} = 20$. This noise model mimics the effect in which the transverse noise level is higher in regions of low magnetic field strength (Wiegelmann et al. 2006).

The bottom row of Fig. 3.5 shows the preprocessed vector magnetogram (for noise model I) after applying our procedure. The aim of the preprocessing is to use the result-

Table 3.2: Figures of merit for the three different nonlinear force-free magnetic field extrapolations from noisy magnetograms from the three noise models with and without preprocessing along with model reference field and potential field. (Prepro stands for preprocessed.)

Model	Prepro	$\mathcal{L}_\omega$	$\mathcal{L}_\mathrm{f}$	$\mathcal{L}_\mathrm{d}$	$\Vert \nabla \cdot \mathbf{B} \Vert_\infty$	$\Vert \mathbf{j} \times \mathbf{B} \Vert_\infty$	C_vec	C_CS	E_N	E_M	ϵ	Steps
Original		0.029	0.015	0.014	1.180	1.355	1	1	0	0	1	
Potential		0.020	0.007	0.014	1.706	1.091	0.736	0.688	0.573	0.535	0.676	
Noise mod. I	No	22.015	8.612	13.403	25.531	11.671	0.819	0.767	0.337	0.421	0.861	1337
Noise mod. I	Yes	0.105	0.066	0.039	1.746	1.806	0.951	0.947	0.197	0.105	0.964	12191
Noise mod. II	No	18.957	7.915	11.042	23.089	9.871	0.828	0.774	0.321	0.417	0.869	1484
Noise mod. II	Yes	0.097	0.057	0.040	1.533	1.617	0.963	0.951	0.191	0.099	0.971	11423
Noise mod. III	No	17.718	7.615	10.103	20.763	8.992	0.859	0.781	0.310	0.402	0.873	1497
Noise mod. III	Yes	0.081	0.043	0.038	1.382	1.407	0.979	0.957	0.189	0.098	0.982	10378

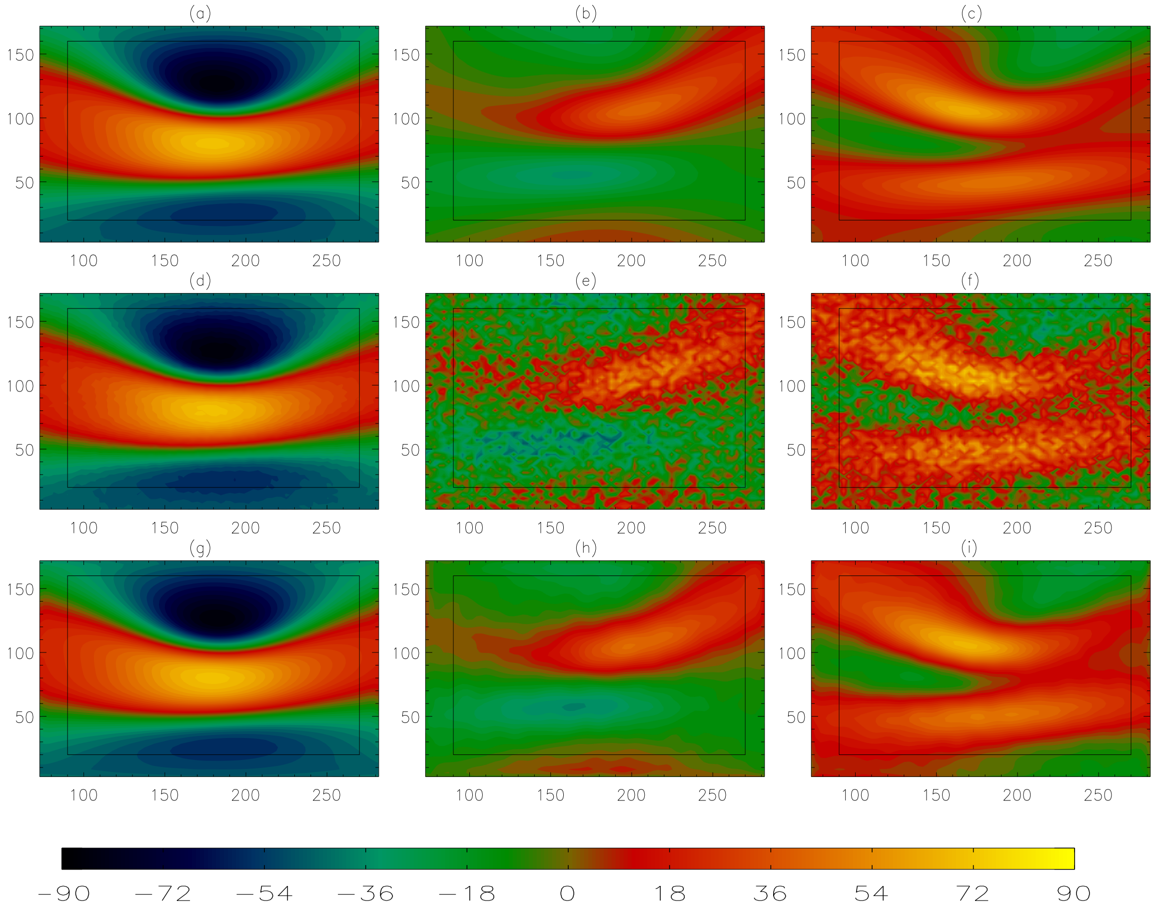

Figure 3.5: **Top row:** vector magnetogram derived from the Low and Lou solution. From left to right the three components B_r, B_θ & B_ϕ are shown). **Middle row:** the same magnetogram as in the first row, but with noise added (noise model I). **Bottom row:** magnetogram resulting from preprocessing of the disturbed magnetogram shown in the second row. The magnetic fields are measured in gauss. The vertical and horizontal axes show latitude, θ and longitude, ϕ on the photosphere respectively.

ing magnetogram as input for a nonlinear force-free magnetic field extrapolation. During the iterative proccess the force-balance parameter $\varepsilon_{\text{force}}$ and the torque-balance parameter $\varepsilon_{\text{torque}}$ decrease to zero for vector magnetogram with noise model I as shown in Fig. 3.7. Figure 3.6 shows in panel a) the original Low and Lou solution and in panel b) a corresponding potential field reconstruction. In Fig. 3.6 we present only the inner region of the whole magnetogram (marked with black rectangular box in Fig. 3.5(a)) because the surrounding magnetogram is used as a boundary layer (6 grid points) for our nonlinear force-free code. The computation was done on a $26 \times 60 \times 74$ grid including a 6 pixel boundary layer towards the lateral and top boundary of the computational box V. In the remaining panels of Fig. 3.6, we demonstrate the effect of the noise model (I) on the reconstruction. The noise levels were chosen so that the mean noise was similar for all three noise models. Fig. 3.6 (c) shows a nonlinear force-free reconstruction with noisy data (noise model I, magnetogram shown in the central panel of Fig. 3.5), and Fig. 3.6 (d) presents a nonlinear force-free reconstruction after preprocessing (magnetogram shown

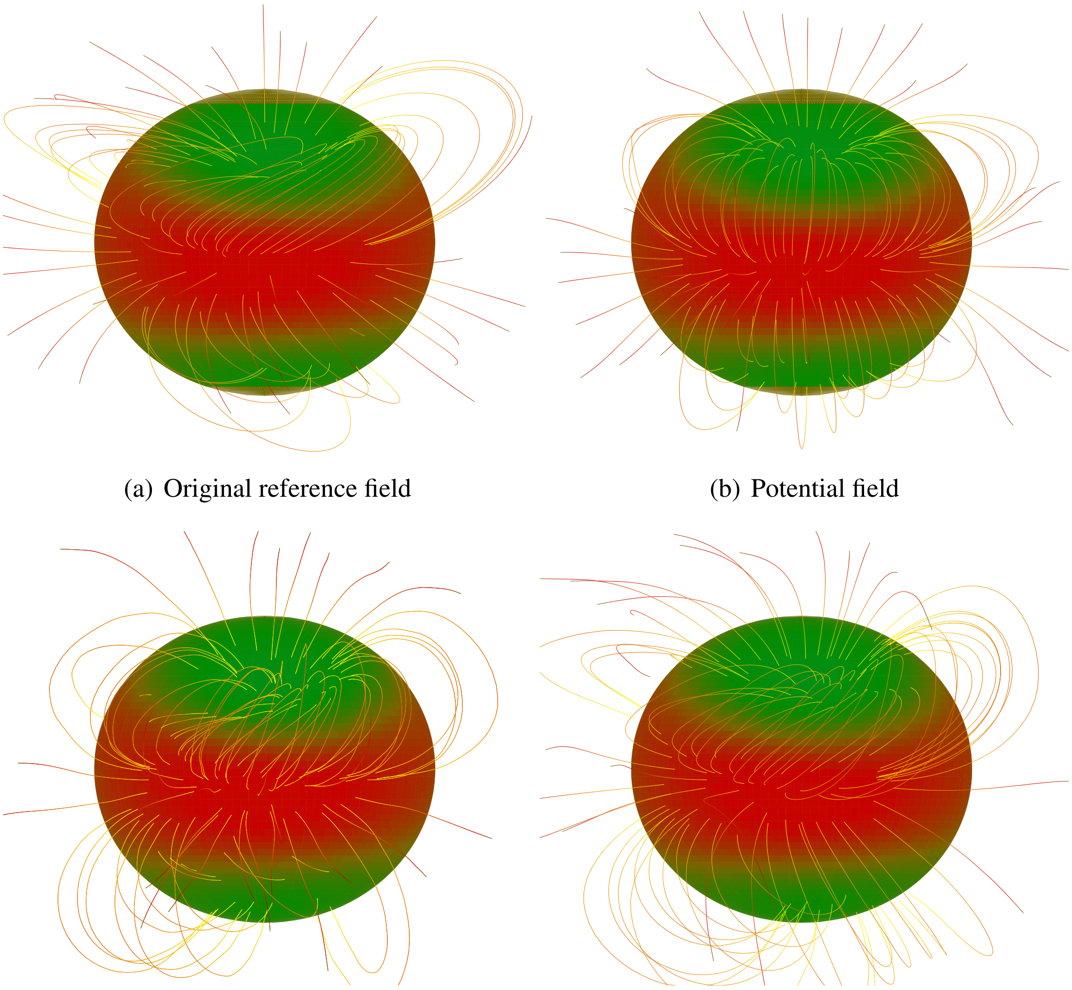

(a) Original reference field (b) Potential field

(c) Field from unpreprocessed noisy data (d) Field from preprocessed noisy data

Figure 3.6: a) Some field lines for the original Low and Lou solution. b) Potential field reconstruction. c) Nonlinear force-free reconstruction from noisy data (noise model I) without preprocessing. d) Nonlinear force-free reconstruction from noisy data (noise model I) after preprocessing the vector magnetogram with our newly developed spherical code.

in the bottom panel of Fig. 3.5). After preprocessing(see Fig. 3.6 d), we achieve a far closer agreement with the original solution (Fig. 3.6 a). Field lines are plotted from the same photospheric footpoints in the positive polarity region of the magnetogram.

For the other noise models II and III, we find that the preprocessed data agree more closely with the original Fig. 3.6 (a). We check the correlation of the original solution with our reconstruction with help of the vector correlation function as defined in (3.21).

Table 3.2 confirms the visual inspection of Fig. 3.6. The correlation of the reconstructed magnetic field with the original improves significantly after preprocessing of the data for all noise models. We knew already from previous studies (Wiegelmann and Neukirch 2003, Wiegelmann 2004) that noise and inconsistencies in vector magnetograms have a negative influence on the nonlinear force-free reconstruction, and the preprocessing routine described in this work shows how to overcome these difficulties in the case of spherical geometry. As indicated by Fig. 3.8, the higher the noise level we add to

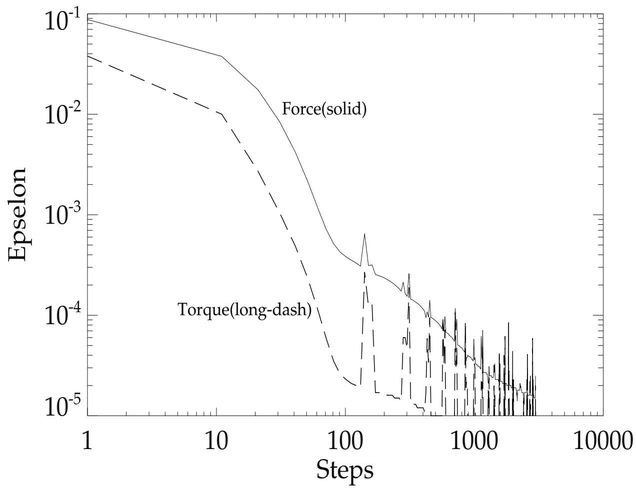

Figure 3.7: Graph of force-balance parameter $\varepsilon_{\text{force}}$ and the torque-balance parameter $\varepsilon_{\text{torque}}$ for vector magnetogram with noise model I against iterative steps.

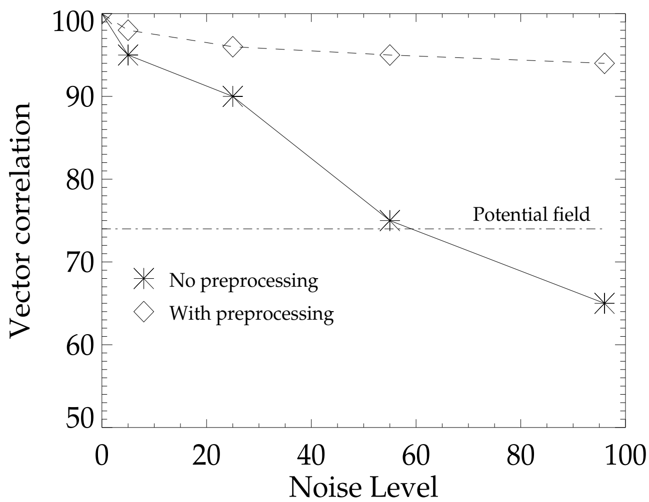

Figure 3.8: Vector correlation plotted against noise level for noise model I.

the original magnetogram, the smaller the vector correlation will be for the field reconstructed from the magnetogram with noise, compared with the reference field. However, the corresponding vector correlations for the field reconstructed from the preprocessed magnetogram has no significant change as the code largely removes the noise we have added to the original magnetogram with different noise levels.

3.3 Summary and conclusions

In this work, we have developed and tested the optimization method for the reconstruction of nonlinear force-free coronal magnetic fields in spherical geometry by restricting the code to limited parts of the Sun, as suggested by Wiegelmann (2007). The optimization method minimizes a functional consisting of a quadratic form of the force balance and the solenoidal condition. Without a weighting function, all the six boundaries are equally likely to influence the solution. The effect of top and lateral boundaries can be reduced by introducing a boundary layer around the physical domain (Wiegelmann 2004). The physical domain is a wedge-shaped area within which we reconstruct the coronal magnetic field that is consistent with the photospheric vector magnetogram data. The boundary layer replaces the hard lateral and top boundary used previously. In the physical domain, the weighting function is unity. It drops monotonically inside the boundary layer and reaches zero at the boundary of the computational box. At the boundary of the computational box, we set the field to have the value of the potential field computed from B_r at the bottom boundary. Our test calculations show that a finite-sized weighted boundary yields far more reliable results. The depth nd of this buffer boundary influences the quality of reconstruction, since the magnetic flux in these test cases is not concentrated well inside the interior of the box.

In this work, we have presented a method for preprocessing vector magnetogram data with help of an optimization code in spherical geometry. The preprocessing result is used as input for a nonlinear force-free magnetic field extrapolation. We extended the preprocessing routine developed by Wiegelmann et al. (2006) to spherical geometry. As a first test of the method, we use the Low and Lou solution with noise from different noise models added. A direct use of the noisy photospheric data for a nonlinear force-free extrapolation showed no good agreement with the original Low and Lou solution, but after applying our newly developed preprocessing method we obtained a reasonable agreement with the original. The preprocessing method changes the boundary data within their noise limits to drive the magnetogram towards boundary conditions that are more consistent with the assumption of a force-free field above. The transverse field components with higher noise level are modified more than the radial components.

To carry out the preprocessing, we use a minimization principle. On the one hand, we control the final boundary data to be as close as possible (within the noise level) to the original measured data, and the data are forced to fulfill the consistency criteria and be sufficiently smooth. Smoothness of the boundary data is required by the nonlinear force-free extrapolation code, but also necessary physically because the magnetic field at the basis of the corona should be smoother than in the photosphere, where it is measured. In addition to these, we found that adding a larger amount of noise to the magnetogram decreases its vector correlation with the model reference field whenever we reconstruct it without preprocessing.

4 Treatment of measurement errors and missing data in vector magnetograms

In a recent joint study by DeRosa et al. (2009) which deals with an observed data-set (vector magnetogram taken with Hinode/SOT embedded in a line-of-sight magnetogram from SOHO/MDI) different force-free codes did not find consistent solutions with stereoscopically reconstructed loop shapes of the same region. A major problem in this study was that only for a part of the model region vector magnetograms were observed (in the Hinode field-of-view, FOV) and the transverse magnetic field component B_{trans} was unknown in the remaining photospheric area. In the study, the missing field components were replaced by zeros, which was insufficient way to treat the missin data. In view of the inconsistency of the results DeRosa et al. (2009) concluded that a successful nonlinear force-free reconstruction requires: (1.) a large computational domain with a high resolution, which accommodates most of the connectivity within the coronal region under study, (2.) to take into account the measurement uncertainties, in particular for the transverse field components, and (3.) preprocessing of the observed vector field that approximates the physics of the photosphere-to-chromosphere interface as it transforms the observed, forced, photospheric field to a more realistic approximation of the near force-free field in the upper chromosphere. The problem of preprocessing (3) has already been addressed in several works (Wiegelmann et al. 2006, Fuhrmann et al. 2007, Wiegelmann et al. 2008, Tadesse et al. 2009). The main emphasis of this chapter (partly published in Tadesse et al. (2011a,b)) is to describe how to improve the algorithm for computing the nonlinear force-free coronal magnetic field and how to incorporate measurement errors and how to handle missing data in the boundary conditions. Finally, we describe the generalization to spherical geometry.

In this work, we use a large computational domain which accommodates most of the connectivity within the coronal region. This requires a spherical version of the optimization procedure. We take uncertainties of measurements in vector magnetograms into account and add a term to treat the measurement errors, similar to the one that has been implemented in cartesian geometry in Wiegelmann and Inhester (2010). In the following, the updated optimization approach for extrapolating the coronal magnetic field in spherical geometry will be discussed in § 4.1 and the method to provide consistent boundary conditions for missing data points is outlined in § 4.2. More emphasis will be given how to use these methods on magnetograms taken from the Synoptic Optical Long-term Investigations of the Sun (SOLIS) in § 4.3. We apply the code to two neighbouring active regions and analyze the resulting coronal magnetic fields in § 4.4. We also apply the code to more larger field of views with three neighbouring active regions and analyze the resulting coronal magnetic fieldsin § 4.5. Finally, in § 4.6 a short summary is given.

4.1 Optimization procedure for missing data points and measurement errors

The equilibrium structure of the coronal magnetic field when non-magnetic forces are negligible, the force-free assumption is formulated as:

$$(\nabla \times \boldsymbol{B}) \times \boldsymbol{B} = 0 \tag{4.1}$$

$$\nabla \cdot \boldsymbol{B} = 0 \tag{4.2}$$

$$\boldsymbol{B} = \tilde{\boldsymbol{B}}_{\rm obs} \quad \text{on photosphere} \tag{4.3}$$

where $\boldsymbol{B}$ is the magnetic field and $\tilde{\boldsymbol{B}}_{\rm obs}$ is 2D observed surface magnetic field on photosphere. Equations (4.1) and (4.2) can be solved with the help of an optimization principle, as proposed by Wheatland et al. (2000) and generalized by Wiegelmann (2004) for cartesian geometry for fixed boundary data. The method minimizes a joint measure of the normalized Lorentz forces and the divergence of the field throughout the volume of interest, V as described in Chapter 3 of this thesis. Throughout this minimization, the photospheric boundary of the model field $\boldsymbol{B}$ is exactly matched to the observed $\tilde{\boldsymbol{B}}_{\rm obs}$ and possibly preprocessed magnetogram values $\tilde{\boldsymbol{B}}$. Here in this work, we use the optimization approach for functional ($\mathcal{L}_\omega$) in spherical geometry (Wiegelmann 2007, Tadesse et al. 2009) along with the new method which instead of an exact match enforces a minimal deviations between the photospheric boundary of the model field $\boldsymbol{B}$ and the magnetogram field $\tilde{\boldsymbol{B}}_{\rm obs}$ by adding an appropriate surface integral term $\mathcal{L}_{\rm photo}$ (Wiegelmann and Inhester 2010).

Assume the Lagrangian to be minimized can be written as:

$$\boldsymbol{B} = \text{argmin}(\mathcal{L}_\omega)$$

$$\mathcal{L}_\omega(\boldsymbol{B}) = \mathcal{L}_f + \mathcal{L}_d + \nu\mathcal{L}_{\rm photo} \tag{4.4}$$

$$\mathcal{L}_f(\boldsymbol{B}) = \int_V \omega_f(r,\theta,\phi)B^{-2}\big|(\nabla \times \boldsymbol{B}) \times \boldsymbol{B}\big|^2 r^2 \sin\theta\, dr\, d\theta\, d\phi$$

$$\mathcal{L}_d(\boldsymbol{B}) = \int_V \omega_d(r,\theta,\phi)\big|\nabla \cdot \boldsymbol{B}\big|^2 r^2 \sin\theta\, dr\, d\theta\, d\phi$$

$$\mathcal{L}_{\rm photo}(\tilde{\boldsymbol{B}}) = \int_S (\tilde{\boldsymbol{B}} - \tilde{\boldsymbol{B}}_{\rm obs}) \cdot \boldsymbol{W}(\theta,\phi) \cdot (\tilde{\boldsymbol{B}} - \tilde{\boldsymbol{B}}_{\rm obs}) r^2 \sin\theta\, d\theta\, d\phi$$

where $\boldsymbol{B}$ is the discrete vector of all magnetic field components. $\mathcal{L}_{\rm f}$ and $\mathcal{L}_{\rm d}$ measure how well the force-free Eqs. (4.1) and divergence-free (4.2) conditions are fulfilled, respectively. $\omega_f(r,\theta,\phi)$ and $\omega_d(r,\theta,\phi)$ are weighting functions. The third integral, $\mathcal{L}_{\rm photo}$, is surface integral over the photosphere which allows us to relax the field on the photosphere towards force-free solution without too much deviation from the original surface field data. $\boldsymbol{W}(\theta,\phi) = \mathrm{diag}(\sigma_i^{-2})$ is a diagonal matrix of size $\bar{m}\times\tilde{m}$ where for each element $i = 1,\bar{m}$, and σ_i^{-2} is the inverse variance of the respective field component. It may be zero where no measurement was made or large where a measurement value is dead certain. Typically, σ_i^{-2} is larger for the normal components than for the horizontal boundary field components. $\boldsymbol{W}(\theta,\phi)$ is the diagonal matrix defined as follows:

$$\boldsymbol{W}(\theta,\phi) = \begin{pmatrix} \mathrm{w}_{\mathrm{radial}} & 0 & 0 \\ 0 & \mathrm{w}_{\mathrm{trans}} & 0 \\ 0 & 0 & \mathrm{w}_{\mathrm{trans}} \end{pmatrix}$$

Finally, this yields the iterative Landweber steps as

$$\boldsymbol{B}^{(k+1)} = \boldsymbol{B}^{(k)} + dt\mu(\nabla_{\boldsymbol{B}}\mathcal{L}_\omega)(\boldsymbol{B}^{(n)}) + 2dt\nu\boldsymbol{W}(\theta,\phi)(\tilde{\boldsymbol{B}} - \tilde{\boldsymbol{B}}_{\mathrm{obs}}) \tag{4.5}$$

where μ is constant and ν is Lagragian multiplier. Hence, the inner field values are modified as before except that the boundary field values are not the observed but the currently iterated ones. In addition there is the iteration of the boundary values in the last term of Eq. (4.5).

Numerical tests of the effect of the new term $\mathcal{L}_{\mathrm{photo}}$ were performed by Wiegelmann and Inhester (2010) in cartesian geometry for a synthetic magnetic field vector generated from Low & Lou model (Low and Lou 1990). They showed that this new method to incorporate the observed boundary field allows to cope with data gaps as they are present in SOLIS and other vector magnetogram data. Within this work, we use a spherical geometry for the full disk data from SOLIS. We use a spherical grid r, θ, ϕ with n_r, n_θ, n_ϕ grid points in the direction of radius, latitude, and longitude, respectively.

4.2 Preprocessing for missing data points

The preprocessing scheme of Tadesse et al. (2009)(as presented in section 3.2.2) involves minimizing a two-dimensional functional of quadratic form in spherical geometry as follows:

$$\tilde{\boldsymbol{B}} = \mathrm{argmin}(L_p)$$

$$L_p = \mu_1 L_1 + \mu_2 L_2 + \mu_3 L_3 + \mu_4 L_4 \tag{4.6}$$

where $\tilde{\boldsymbol{B}}$ is preprocessed surface magnetic field from the input observed field $\tilde{\boldsymbol{B}}_{\mathrm{obs}}$. Each of the constraints L_n is weighted by a yet undetermined factor μ_n. The first term ($n = 1$) corresponds to the force-balance condition, the next ($n = 2$) to the torque-free condition, and the last term ($n = 4$) controls the smoothing. The explicit form of L_1, L_2, and L_4 can be found in Tadesse et al. (2009). The term ($n = 3$) ensures that the optimized boundary condition agrees with the measured photospheric data. In the case of missing data points (i.e., SOLIS/VSM) we modified L_3 with respect to the one in Eq. (3.52) as follows, to treat those data gaps.

$$L_3 = \sum_p (\tilde{\boldsymbol{B}} - \tilde{\boldsymbol{B}}_{\mathrm{obs}}) \cdot \boldsymbol{W}(\theta,\phi) \cdot (\tilde{\boldsymbol{B}} - \tilde{\boldsymbol{B}}_{\mathrm{obs}}), \tag{4.7}$$

In this integral, $\boldsymbol{W}(\theta, \phi)$ is a diagonal matrix which gives different weights to the different observed surface field components depending on their relative measurement accuracy. A careful choice of the preprocessing parameters μ_n ensures that the preprocessed magnetic field $\tilde{\boldsymbol{B}}$ does not deviate from the original observed field $\tilde{\boldsymbol{B}}_{\rm obs}$ by more than the measurement errors. As the result of a parameter study in this work, we found $\mu_1 = \mu_2 = 1.0$, $\mu_3 = 0.03$ and $\mu_4 = 0.45$ as optimal value for particular data set of vector magnetogram observed on 15 May 2009 by SOLIS/VSM. We also found $\mu_1 = \mu_2 = 1.0$, $\mu_3 = 0.3$ and $\mu_4 = 0.65$ as optimal values for the observations on March 28, 29, and 30 2008(for detailed descriptions of those parameters, see section 3.2 of this thesis).

4.3 The SOLIS/VSM instrument

In this study, we use vector magnetogram observations from the Vector Spectromagnetograph (VSM; see Jones et al. 2002), which is part of the Synoptic Optical Long-term Investigations of the Sun (SOLIS) synoptic facility (SOLIS; see Keller et al. 2003). VSM/SOLIS currently operates at the Kitt Peak National Observatory, Arizona, and it has provided magnetic field observations of the Sun almost continuously since August 2003.

VSM is a full disk Stokes Polarimeter. As part of daily synoptic observations, it takes four different observations in three spectral lines: Stokes I(intensity), V (circular polarization, Q, and U (linear polarization) in photospheric spectral lines Fe I 630.15 nm and Fe I 630.25 nm , Stokes I and V in Fe I 630.15 nm and Fe I 630.25 nm, similar observations in chromospheric spectral line Ca II 854.2 nm, and Stokes I in the He I 1083.0 nm line and the near-by Si I spectral line. Observations of I, Q, U, and V are used to construct a full disk vector magnetograms, while $I - V$ observations are employed to create separate full disk longitudinal magnetograms in the photosphere and the chromosphere.

In this study, we use a vector magnetogram observed on 15 May 2009. The data were taken with 1.125 arcsec pixel size and 2.71pm spectral sampling. (In December 2009, SOLIS/VSM cameras has been upgraded from Rockwell (90 Hz, 18 micron pixels) to Sarnoff (300 Hz, 16 micron pixels). This camera upgrade has resulted in improved spatial and spectral sampling). The noise level for line-of-sight component is about 1 Gauss. However, noise due to atmospheric seeing may be much larger, and the final measurement error depends on the measured flux, its spatial distribution as well as the seeing conditions. A rough estimate suggests a noise level of a few tens of Gauss for areas with a strong horizontal gradient of magnetic field and about 1 arcsec atmospheric seeing.

To create a single magnetogram, the solar disk is scanned from terrestrial South to North; it takes about 20 minutes to complete one vector magnetogram. After the scan is done, the data are sent to an automatic data reduction pipeline that includes dark and flat field correction. Once the spectra are properly calibrated, full disk vector (magnetic field strength, inclination, and azimuth) magnetograms are created using two different approaches. Quick-look (QL) vector magnetograms are generated based on an algorithm by Auer et al. (1977). The algorithm uses the Milne-Eddington model of solar atmosphere, which assumes that the magnetic field is uniform throughout the layer of spectral line formation (Unno 1956). It also assumes symmetric line profiles, disregards magneto-optical effects (e.g., Faraday rotation), and does not separate contributions of magnetic

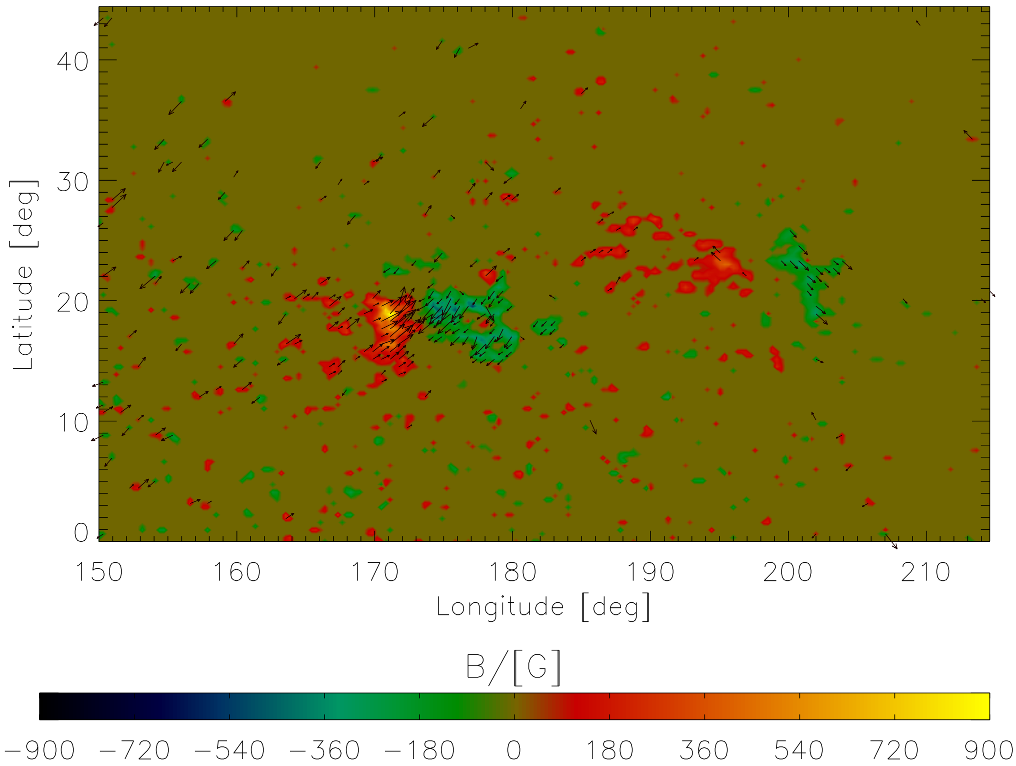

Figure 4.1: Surface contour plot of radial magnetic field vector and vector field plot of transverse field with black arrows.

and non-magnetic components in spectral line profile (i.e., magnetic filling factor is set to unity). A more sophisticated inversion of the spectral data is performed later using a technique developed by Skumanich and Lites (1987). This latter inversion (called ME magnetogram) also employs the Milne-Eddington model of atmosphere, but it solves for magneto-optical effects and determines magnetic filling factor (fractional contribution of magnetic and non-magnetic components to each pixel). The ME inversion is only performed for pixels with spectral line profiles above the noise level. For pixels below the polarimetric noise threshold, magnetic field parameters are set to zero.

The 180° ambiguity (see chapter one section 1.2) is resolved using the Non-Potential Field Calculation (NPFC; see Georgoulis 2005). The NPFC method was selected on the basis of comparative investigation of several methods for 180-degree ambiguity resolution (Metcalf et al. 2006). Both QL and ME magnetograms can be used for potential and/or force-free field extrapolation. However, in strong fields inside sunspots, the QL field strengths may exhibit erroneous decrease inside sunspot umbra due to, so called magnetic saturation. For this study we choose to use fully inverted ME magnetograms. Fig. 4.1 shows a map of the radial component of the field as a contour plot with the transverse magnetic field depicted as black arrows. For this particular dataset, about 80% of the data pixels are undetermined and as a result the ratio of data gaps to total number of pixels is large.

4.3.1 Implementing the method to SOLIS data

The method has been implemented to SOLIS data as follows:

- We compute an initial source surface potential field in the computational domain from $\tilde{\boldsymbol{B}}_{robs}$, the normal component of the surface field at the photosphere at $r = 1R_{\odot}$.

- We minimize $\mathcal{L}_{\omega}$(Eqs. 4.4) iteratively without constraining $\tilde{\boldsymbol{B}}_{\text{obs}}$ at the photosphere boundary as in previous version of Wheatland algorithm (Wheatland et al. 2000). The model magnetic field $\boldsymbol{B}$ at the surface is gradually driven towards the observations while the field in the volume V relaxes to force-free. If the observed field is inconsistent, the difference $\boldsymbol{B} - \tilde{\boldsymbol{B}}_{\text{obs}}$ or $\boldsymbol{B} - \tilde{\boldsymbol{B}}$ (for preprocessed data) remains finite depending in the control parameter ν. At data gaps in $\tilde{\boldsymbol{B}}_{\text{obs}}$, we set $\mathrm{w}_{\text{radial}} = 0$ and $\mathrm{w}_{\text{trans}} = 0$ and respective field value is automatically ignored.

- The state $\mathcal{L}_{\omega} = 0$ corresponds to a perfect force-free and divergence-free state and exact agreement of the boundary values $\boldsymbol{B}$ with observations $\tilde{\boldsymbol{B}}_{\text{obs}}$ in regions where $\mathrm{w}_{\text{radial}}$ and $\mathrm{w}_{\text{trans}}$ are greater than zero. For inconsistent boundary data the force-free and solenoidal conditions can still be fulfilled, but the surface term $\mathcal{L}_{\text{photo}}$ will remain finite. This results in some deviation of the bottom boundary data from the observations, especially in regions where $\mathrm{w}_{\text{radial}}$ and $\mathrm{w}_{\text{trans}}$ are small. The parameter ν is tuned so that these deviations do not exceed the local estimated measurement error.

- The iteration stops when $\mathcal{L}_{\omega}$ becomes stationary as $\Delta\mathcal{L}_{\omega}/\mathcal{L}_{\omega} < 10^{-4}$.

4.4 Application to two neighbouring active regions

We use the vector magnetograph data from the Synoptic Optical Long-term Investigations of the Sun survey (SOLIS) to model the coronal magnetic field. We extrapolate by means of Eq. (4.4) both the observed field $\tilde{\boldsymbol{B}}_{\text{obs}}$ measured above two active regions observed on May 15 2009 and preprocessed surface field ($\tilde{\boldsymbol{B}}$, obtained from $\tilde{\boldsymbol{B}}_{\text{obs}}$ applying our preprocessing procedure). We compute 3D magnetic field in a wedge-shaped computational box V, which includes an inner physical domain V' and the buffer zone (the region outside the physical domain), as shown in Fig. 4.3 of the bottom boundary on the photosphere. The wedge-shaped physical domain V' has its latitudinal boundaries at $\theta_{\min} = 3°$ and $\theta_{\max} = 42°$, longitudinal boundaries at $\phi_{\min} = 153°$ and $\phi_{\max} = 212°$, and radial boundaries at the photosphere ($r = 1R_{\odot}$) and $r = 1.75R_{\odot}$.

4.4.1 Analysis of the result

The weighting function ω_f and ω_d in $\mathcal{L}_f$ and $\mathcal{L}_d$ in Eq. (4.4) are chosen to be unity within the inner physical domain V' and decline with a cosine profile in the buffer boundary region (Wiegelmann 2004, Tadesse et al. 2009, see also chapter 3 of this thesis). They reach a zero value at the boundary of the outer volume V. The distance between the boundaries of V' and V is chosen to be $nd = 10$ grid points wide. The framed region in Figs. 4.3.(a-i) corresponds to the lower boundary of the physical domain V' with a resolution

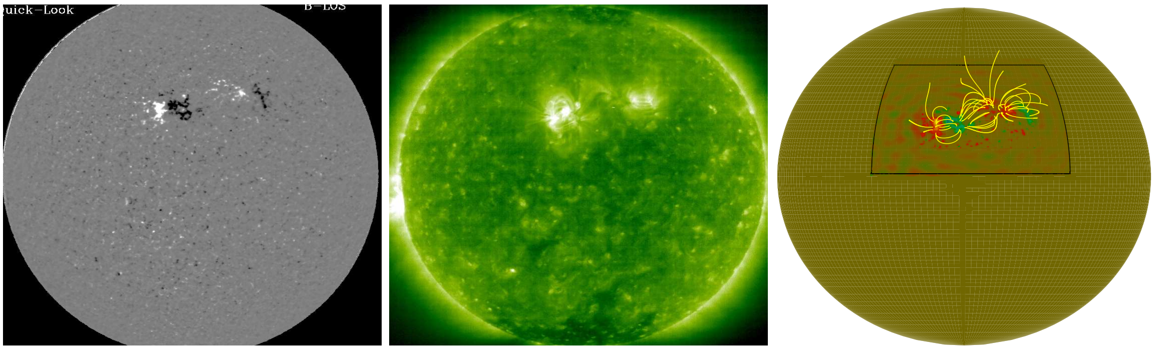

Figure 4.2: **Left:** Full disc vector magnetogram of May 15 2009 at 16:02UT. **Middle:** SOHO/EIT image of the Sun on the same day at 16:00UT. **Right:** potential magnetic field line plot of SOLIS vector magnetogram at16:02UT, that has been computed from the observed radial component.

of 132×196 pixels in the photosphere. The original full disc vector magnetogram has a resolution of 1788×1788 pixels out of which we extracted 142×206 pixels for the lower boundary of the computational domain V, which corresponds to $550Mm \times 720Mm$ on the photosphere.

The main reason for the implementation of the new term $\mathcal{L}_{\rm photo}$ in Eq. (4.4) is that we need to deal with boundary data of different noise levels and qualities or even lack some data points completely. SOLIS/VSM provides full-disk vector-magnetograms, but for some individual pixels the inversion from line profiles to field values may not have been successful and field data there will be missing for these pixels. Since the previous code described in chapter 3 of this thesis without the term $\mathcal{L}_{\rm photo}$ requires complete boundary information, it can not be applied to this set of SOLIS/VSM data. In our new code, these data gaps are treated by setting $W = 0$ for these pixels in Eqs. (4.4). For those pixels, for which $\tilde{\boldsymbol{B}}_{\rm obs}$ was successfully inverted, we allow deviations between the model field $\boldsymbol{B}$ and the input fields either observed $\tilde{\boldsymbol{B}}_{\rm obs}$ or preprocessed surface field $\tilde{\boldsymbol{B}}$ using Eqs. (4.4) and so that the model field can be iterated closer to a force-free solution even if the observations are inconsistent. This balance is controlled by the Lagrangian multiplier ν as explained in Wiegelmann and Inhester (2010). In this work we used $\mathrm{w}_{\rm radial} = 100\mathrm{w}_{\rm trans}$ for the surface fields both from data with and without preprocessing.

Figure 4.2. shows the position of the active region on the solar disk both for SOLIS full-disk magnetogram [1], SOHO/EIT image of the Sun observed at 195Å on the same day at 16:00UT.[2] As stated in section 2.3, the potential field is used as initial condition for iterative minimization required in Eq. 4.4. The respective potential field is shown in the rightmost panel of Fig. 4.2. During the iteration, the code forces the photospheric boundary of $\boldsymbol{B}$ towards observed field values $\tilde{\boldsymbol{B}}_{\rm obs}$ or $\tilde{\boldsymbol{B}}$ (for preprocessed data) and ignores data gaps in the magnetogram. A deviation between surface vector field from model $\boldsymbol{B}$ and $\tilde{\boldsymbol{B}}_{\rm obs}$ or $\tilde{\boldsymbol{B}}$ (for preprocessed data) occurs where $\tilde{\boldsymbol{B}}_{\rm obs}$ is not consistent with a force-free field. In this sense, the term $\mathcal{L}_{photo}$ in Eq. (4.4) acts on $\tilde{\boldsymbol{B}}_{\rm obs}$ similarly as the preprocessing, it generates a surface field $\boldsymbol{B}$ instead of $\tilde{\boldsymbol{B}}$ from $\tilde{\boldsymbol{B}}_{\rm obs}$ which is close to $\tilde{\boldsymbol{B}}_{\rm obs}$, but consistent

[1] http://solis.nso.edu/solis data.html
[2] http://sohowww.nascom.nasa.gov/data/archive

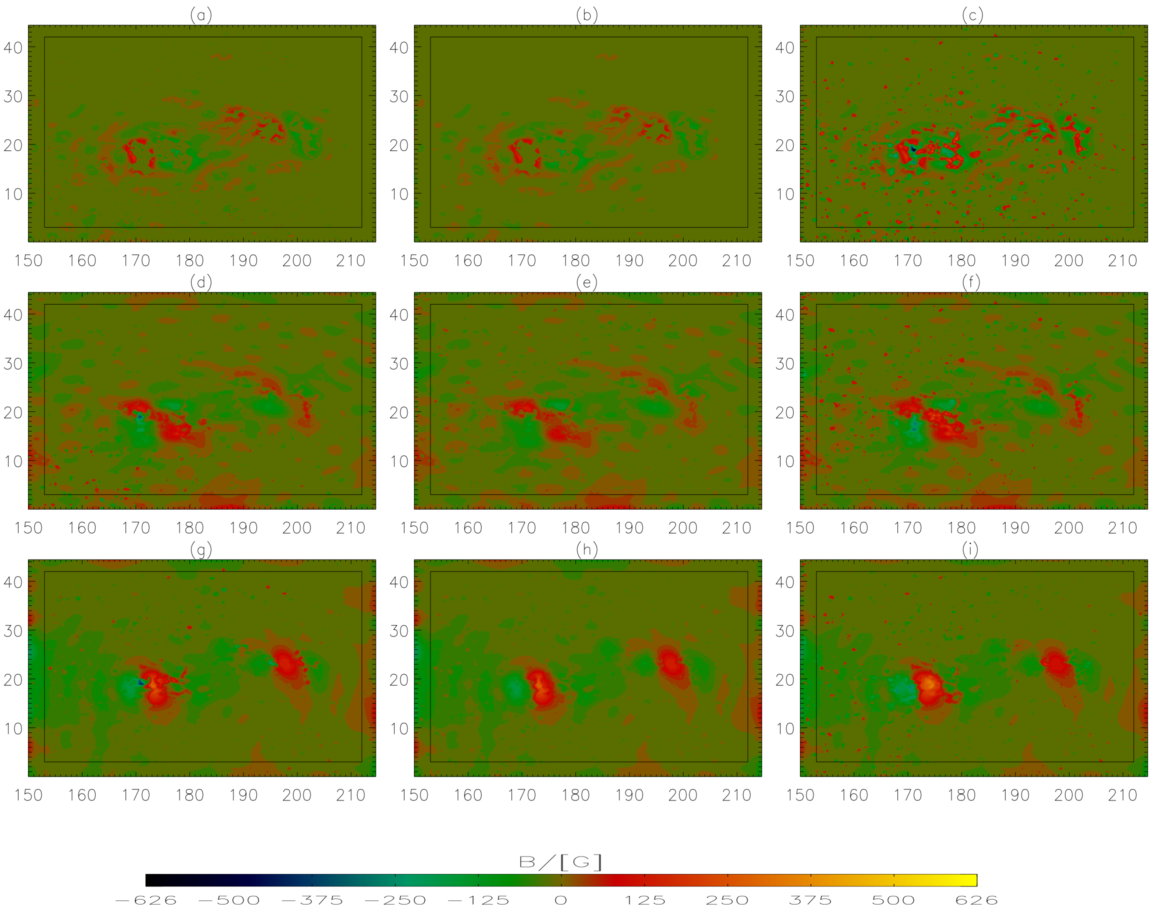

Figure 4.3: **Top row:** Radial surface vector field difference of a). modelled $\boldsymbol{B}$ without preprocessing and $\tilde{\boldsymbol{B}}_{\rm obs}$ b). modelled $\boldsymbol{B}^{\rm pre}$ and $\tilde{\boldsymbol{B}}_{\rm obs}$ c). initial potential and $\tilde{\boldsymbol{B}}_{\rm obs}$. **Middle row:**Latitudinal surface vector field difference of d). modelled $\boldsymbol{B}$ without preprocessing and $\tilde{\boldsymbol{B}}_{\rm obs}$ e). modelled $\boldsymbol{B}^{\rm pre}$ and $\tilde{\boldsymbol{B}}_{\rm obs}$ f). initial potential and $\tilde{\boldsymbol{B}}_{\rm obs}$. **Bottom row:**Longitudinal surface vector field difference of g). modelled $\boldsymbol{B}$ without preprocessing and $\tilde{\boldsymbol{B}}_{\rm obs}$ h). modelled $\boldsymbol{B}^{\rm pre}$ and $\tilde{\boldsymbol{B}}_{\rm obs}$ i). initial potential and $\tilde{\boldsymbol{B}}_{\rm obs}$. The vertical and horizontal axes show latitude, θ and longitude, ϕ on the photosphere respectively.

with a force-free field above the surface. In Fig. 4.3 we therefore compare the option of the preprocessing and the new extrapolation code (Eq. 4.4) on $\tilde{\boldsymbol{B}}_{\rm obs}$. The figure shows the surface magnetic field differences of the preprocessed, un-preprocessed and the potential surface fields.

In order to determime the similarity of vector components on the bottom surface, we calculate their pixel-wise correlations. The correlation were calculated from:

$$C_{\rm vec} = \frac{\sum_i \mathbf{v}_i \cdot \mathbf{u}_i}{\sqrt{\sum_i |\mathbf{v}_i|^2}\sqrt{\sum_i |\mathbf{u}_i|^2}} \tag{4.8}$$

where $\mathbf{v}_i$ and $\mathbf{u}_i$ are the vectors at each grid point i on the bottom surface. If the vector fields are identical, then $C_{\rm vec} = 1$; if $\mathbf{v}_i \perp \mathbf{u}_i$, then $C_{\rm vec} = 0$. Table 4.1 shows correlations of the surface fields from $\mathbf{B}^{\rm pre} - \tilde{\boldsymbol{B}}_{\rm obs}$ (where $\boldsymbol{B}^{\rm pre}$ is the model field obtained from

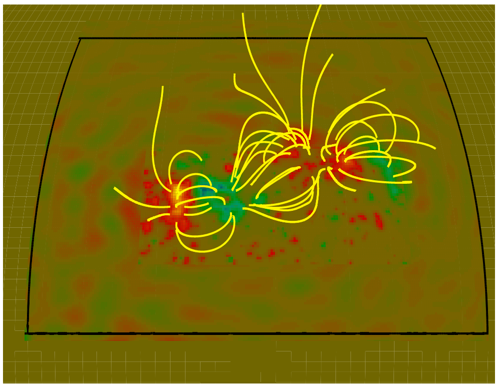

(a) Potential field

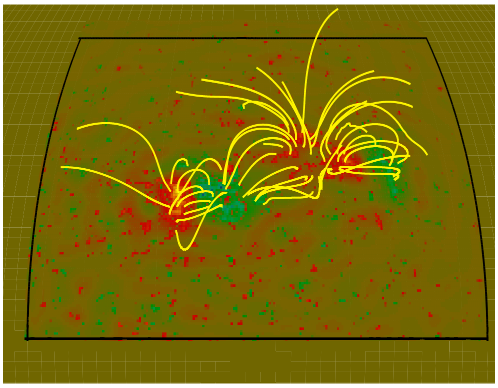

(b) Field from data before preprocessing

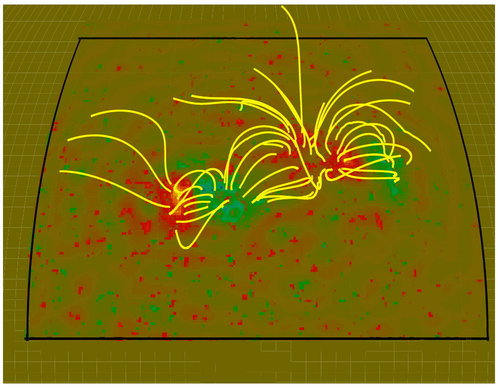

(c) Field from preprocessed data

Figure 4.4: a) Some field lines for the Potential field reconstruction. b) Nonlinear force-free reconstruction from SOLIS data without preprocessing. c) Nonlinear force-free reconstruction from preprocessed SOLIS data.

preprocessed surface field $\tilde{\boldsymbol{B}}$ using Eq. (4.4)) and $\boldsymbol{B}^{\text{unpre}} - \tilde{\boldsymbol{B}}_{\text{obs}}$ (where $\boldsymbol{B}^{\text{unpre}}$ is the model field obtained from observed surface field $\tilde{\boldsymbol{B}}_{\text{obs}}$ using Eq. (4.4)). We have computed the vector correlations of the two surface vector fields for the three components at each grid points to compare how well they are aligned along each directions. From those values in Table 4.1 one can see that the preprocessing and extrapolation with Eq. (4.4) act on $\tilde{\boldsymbol{B}}_{\text{obs}}$ in a similar way. Table 4.1 shows vector correlations of the surface fields from $\boldsymbol{B}^{\text{pre}} - \tilde{\boldsymbol{B}}_{\text{obs}}$ (where $\boldsymbol{B}^{\text{pre}}$ is the model field obtained from preprocessed surface field $\tilde{\boldsymbol{B}}$ using Eq. (4.4)) and $\boldsymbol{B}^{\text{unpre}} - \tilde{\boldsymbol{B}}_{\text{obs}}$ (where $\boldsymbol{B}^{\text{unpre}}$ is the model field obtained from observed surface field $\tilde{\boldsymbol{B}}_{\text{obs}}$ using Eq. (4.4)). From those values one can see that the preprocessing and extrapolation with Eq. (4.4) act on $\tilde{\boldsymbol{B}}_{\text{obs}}$ in a similar way.

In Fig.4.4. we plot magnetic field lines for the two configurations and in addition the field lines of a corresponding potential field for comparison. The vector correlations of potential field lines in 3D box to both the extrapolated NLFF with and without preprocessing data are 0.741 and 0.793, respectively.

Table 4.1: The vector correlations between the components of surface fields from $(\boldsymbol{B}^{\mathrm{pre}} - \tilde{\boldsymbol{B}}_{\mathrm{obs}})$ and $(\boldsymbol{B}^{\mathrm{unpre}} - \tilde{\boldsymbol{B}}_{\mathrm{obs}})$.

v	u	C_{vec}
$(\boldsymbol{B}^{\mathrm{unpre}} - \tilde{\boldsymbol{B}}_{\mathrm{obs}})_r$	$(\boldsymbol{B}^{\mathrm{pre}} - \tilde{\boldsymbol{B}}_{\mathrm{obs}})_r$	0.930
$(\boldsymbol{B}^{\mathrm{unpre}} - \tilde{\boldsymbol{B}}_{\mathrm{obs}})_\theta$	$(\boldsymbol{B}^{\mathrm{pre}} - \tilde{\boldsymbol{B}}_{\mathrm{obs}})_\theta$	0.897
$(\boldsymbol{B}^{\mathrm{unpre}} - \tilde{\boldsymbol{B}}_{\mathrm{obs}})_\phi$	$(\boldsymbol{B}^{\mathrm{pre}} - \tilde{\boldsymbol{B}}_{\mathrm{obs}})_\phi$	0.875

Table 4.2: The magnetic energy associated with extrapolated NLFF field configurations with and without preprocessing.

Model	$E_{\mathrm{nlff}}(10^{32}\mathrm{erg})$	$E_{\mathrm{free}}(10^{32}\mathrm{erg})$
No preprocessing	37.456	4.915
Preprocessed	37.341	4.800

4.4.2 Magnetic energy and electric current density

To understand the physics of solar flares, including the local reorganization of the magnetic field and the acceleration of energetic particles, one has to estimate the free magnetic energy available for such phenomena. This is the free energy that can be converted into kinetic and thermal energy. From the energy budget and the observed magnetic activity in the active region, Régnier and Priest (2007a) and Thalmann et al. (2008) investigated the free energy above the minimum-energy state for the flare process. We estimate the free magnetic energy to be the difference of the extrapolated force-free fields and the potential field with the same normal boundary conditions in the photosphere. We therefore estimate the upper limit to the free magnetic energy associated with coronal currents of the form

$$E_{\mathrm{free}} = \frac{1}{8\pi} \int_V \left(B_{\mathrm{nlff}}^2 - B_{\mathrm{pot}}^2\right) r^2 \sin\theta \, dr \, d\theta \, d\phi, \tag{4.9}$$

where B_{pot} and B_{nlff} represent the potential and NLFF magnetic field, respectively. The free energy for active regions in Fig.4.4 is about 5×10^{32}erg. The magnetic energy associated with the potential field configuration is found to be 32.541×10^{32}erg. Hence, E_{nlff} exceeds E_{pot} by 15%. Table 4.2 shows the magnetic energy associated with extrapolated NLFF field configurations with and without preprocessing. The magnetic energy of the NLFF field configuration obtained from the data without preprocessing is slightly larger than for the preprocessed boundary field, as the preprocessing procedure removes small scale structures.

The electric current density calculated from Ampére's law, $\boldsymbol{J} = \nabla \times \boldsymbol{B}/4\pi$, on the basis of spatially sampled transverse magnetic fields varies widely over an active region. In order to investigate how errors in the vector magnetograph measurements produce errors in the vertical electric current densities, Liang et al. (2009) have numerically simulated the effects of random noise on a standard photospheric magnetic configuration produced

Table 4.3: The currents and average α calculated from those pixels which are magnetically connected. The currents are given in Ampère (A).

	Inside left active region	Between left and right ARs	Inside right active region
Magnetic flux (10^{19}Gcm^2)	3.32	4.61	2.08
Total current (10^6A)	49.6	1.58	32.17
Average α (Mm^{-1})	2.49	0.08	1.62

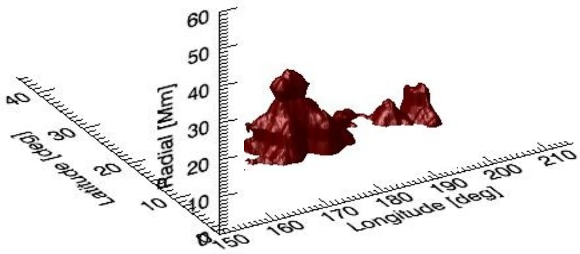

Figure 4.5: Iso-surfaces (ISs) of the absolute current density vector $|J| = 100\text{mA} \cdot \text{m}^{-2}$ computed above the active regions. Units of the axes are in pixel.

by electric currents satisfying the force-free field conditions. Even if the current density can be estimated in the photosphere, it is not intuitively clear how the change in the current density distribution affects a coronal magnetic configuration. Régnier and Priest (2007b) studied such modifications in terms of the geometry of field lines, the storage of magnetic energy and the amount of magnetic helicity. Fig. 4.5. shows Iso-surface plots of the current density above the volume of the active region studied in Figs. 4.3 and 4.4. There are strong current configurations above each active regions. This becomes clear if we compare the total current in between each active region with the current from the left to the right active region. These currents were added up from the surface normal currents emanating from those pixels which are magnetically connected inside or across active regions respectively. The result is shown in table 4.3. The active regions share a decent amount of magnetic flux compared to their internal flux from one polarity to the other. In terms of the electric current they are much more isolated. The ratio of shared to the intrinsic magnetic flux is order of unity, while for the electric current those ratios are much less, 1.58/49.6 and 1.58/32.17, respectively. Similarly we can calculate the average value of α on the field lines with the respective magnetic connectivity. The averages are shown in the second row of table 4.3. The two active regions are magnetically connected but much less by electric currents.

4.5 Application to three neighbouring active regions

We use vector magnetograph data from the Synoptic Optical Long-term Investigations of the Sun survey (SOLIS) measured on March 28, 29, and 30 2008. As a first step for our work we remove non-magnetic forces from observed surface magnetic field using our

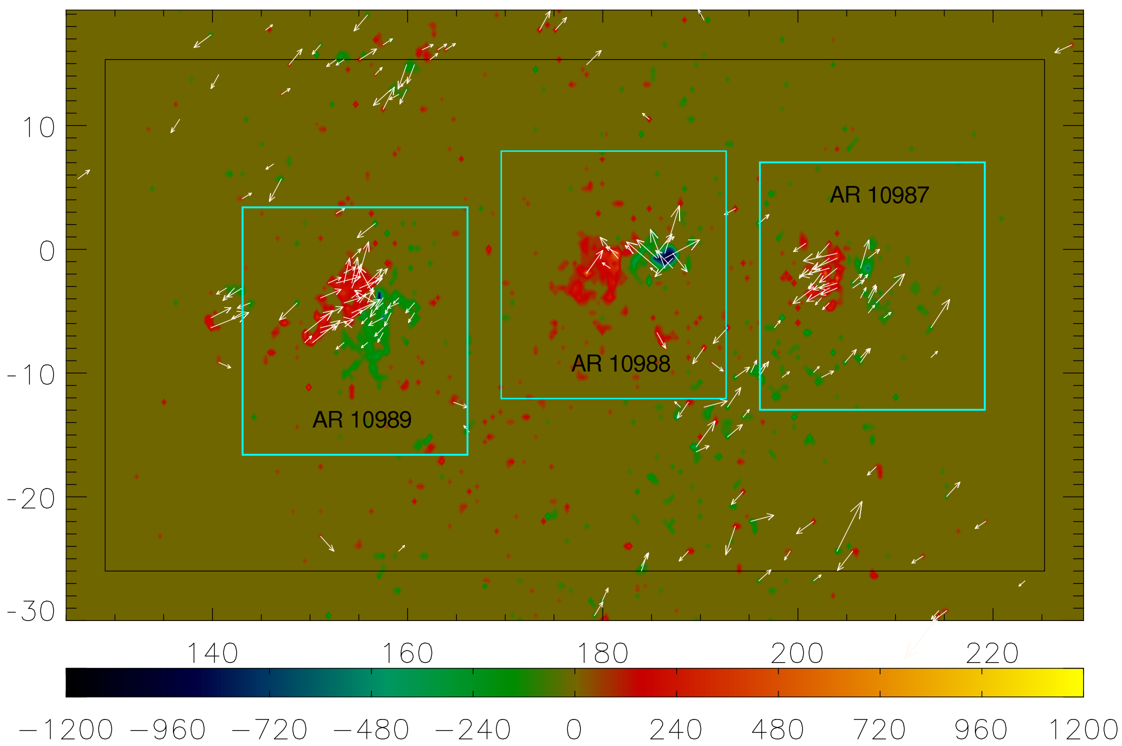

Figure 4.6: Surface contour plot of radial magnetic field vector and vector field plot of transverse field with white arrows. The color coding shows B_r on the photosphere. The magnetic fields are measured in gauss. The vertical and horizontal axes show latitude, θ (in degree) and longitude, ϕ(in degree) on the photosphere.

spherical preprocessing procedure. For this data set, as indicated in Fig. 4.6, for some individual pixels the inversion from line profiles to field values have not been successful inverted. We treat these data gaps by setting $W = 0$ for these pixels in Eqs. (4.4). For those pixels, for which $\tilde{\mathbf{B}}_{\text{obs}}$ was successfully inverted, we allow deviations between the model field $\mathbf{B}$ and the input fields (preprocessed surface field $\tilde{\mathbf{B}}$) using Eqs. (4.4) and so that the model field can be iterated closer to a force-free solution even if the observations are inconsistent. This balance is controlled by the Lagrangian multiplier ν as explained in Wiegelmann and Inhester (2010). In this work we used $\mathrm{w}_{\text{radial}} = 20\mathrm{w}_{\text{trans}}$ for the surface preprocessed fields.

4.5.1 Analysis of the result

We compute the 3D magnetic field above the observed surface region inside wedge-shaped computational box of volume V, which includes an inner physical domain V' and a buffer zone (the region outside the physical domain). The physical domain V' is a wedge-shaped volume, with two latitudinal boundaries at $\theta_{\min} = -26°$ and $\theta_{\max} = 16°$, two longitudinal boundaries at $\phi_{\min} = 129°$ and $\phi_{\max} = 226°$, and two radial boundaries at the photosphere ($r = 1R_\odot$) and $r = 1.75R_\odot$ for the observation on March 29 2008. We define V' to be the inner region of V (including the photospheric boundary) with $\omega = 1$ everywhere including its six inner boundaries $\delta V'$. We use a position-dependent weight-

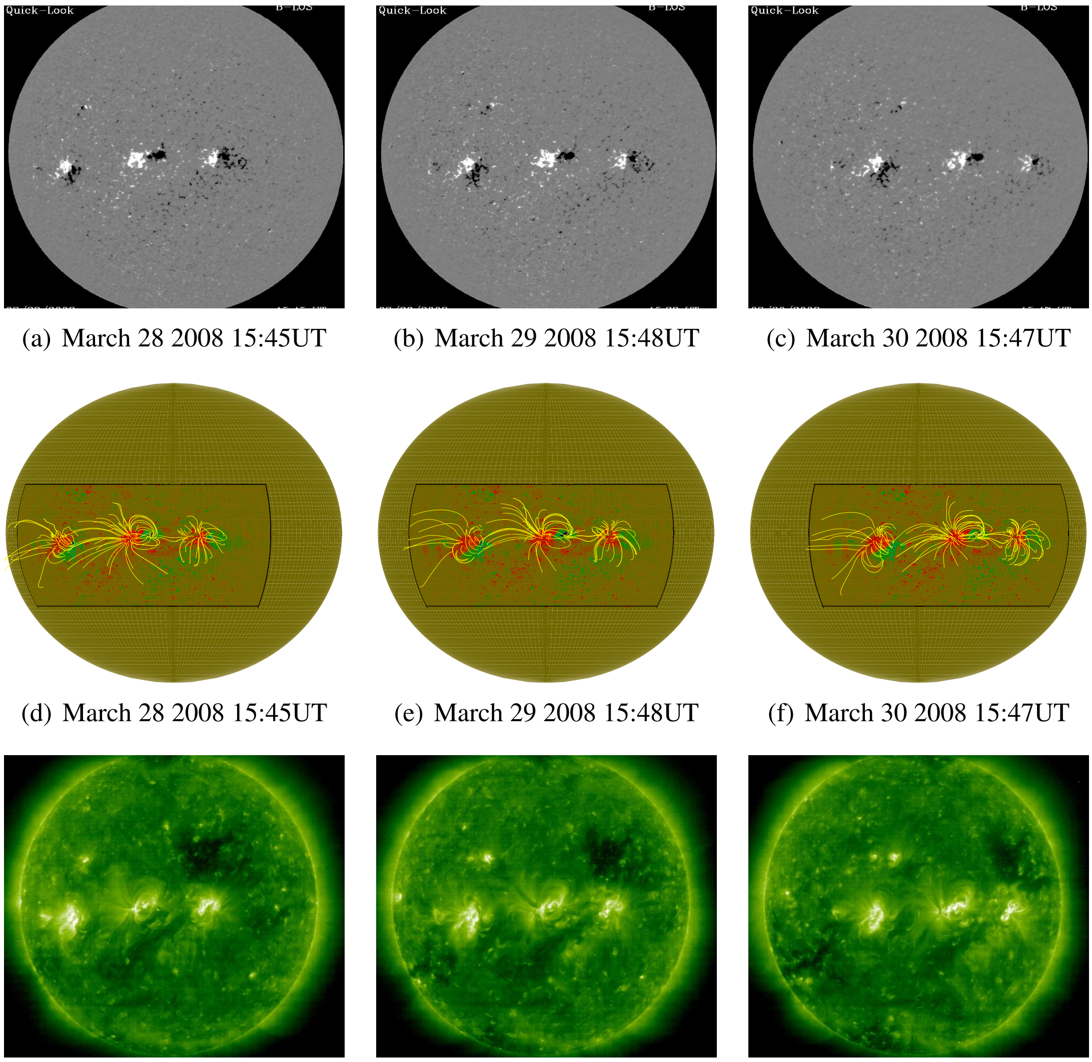

(a) March 28 2008 15:45UT (b) March 29 2008 15:48UT (c) March 30 2008 15:47UT

(d) March 28 2008 15:45UT (e) March 29 2008 15:48UT (f) March 30 2008 15:47UT

(g) March 28 2008 16:00UT (h) March 29 2008 15:48UT (i) March 30 2008 15:48UT

Figure 4.7: **Top row:** SOLIS/VSM magnetograms of respective dates. **Middle row:** Magnetic field lines reconstructed from magnetograms on the top panel. **Bottom row:** EIT image of the Sun at 195Å on indicated dates.

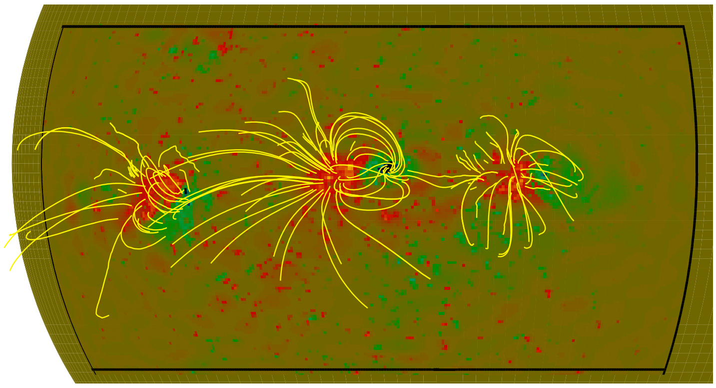

(a) March 28 2008 15:45UT

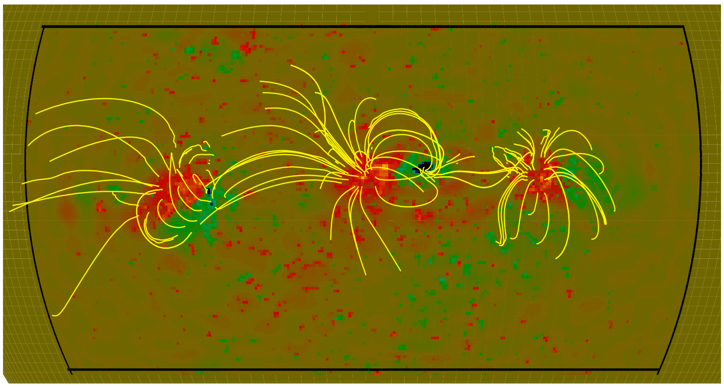

(b) March 29 2008 15:48UT

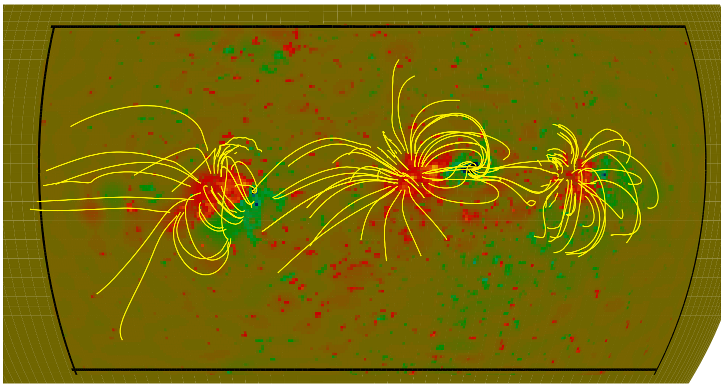

(c) March 30 2008 15:47UT

Figure 4.8: Some magnetic field lines plots reconstructed from SOLIS magnetograms using nonlinear force-free modelling. The color coding shows B_r on the photosphere.

Table 4.4: The magnetic energy associated with extrapolated NLFF field configurations for the three particular dates.

Date	$E_{nlff}(10^{32}\text{erg})$	$E_{\text{pot}}(10^{32}\text{erg})$	$E_{\text{free}}(10^{32}\text{erg})$
March 28 2008	57.34	53.89	3.45
March 29 2008	57.48	54.07	3.41
March 30 2008	57.37	53.93	3.44

ing function to introduce a buffer boundary of $nd = 10$ grid points towards the side and top boundaries of the computational box, V. The weighting function, ω is chosen to be unity within the inner physical domain V' and declines to 0 with a cosine profile in the buffer boundary region (Wiegelmann 2004, Tadesse et al. 2009). The framed region(in black) in Figs. 4.6 corresponds to the lower boundary of the physical domain V' with a resolution of 114×251 pixels in the photosphere.

The middle panel of Fig. 4.7 shows magnetic field lines overplotted on the magnetograms for three consecutive dates. The top and bottom panels of Fig. 4.7 show the position of the three active regions on the solar disk both for SOLIS full-disk magnetogram[3] and SOHO/EIT [4] image of the Sun observed at 195Å on the indicated dates and times. Figure 4.8 shows some selected magnetic field lines from the reconstruction of the SOLIS magnetograms, zoomed in from the middle panels of Fig. 4.7. In each column of Fig. 4.8, the field lines are plotted from the same foot points to compare the change in topology of the magnetic field over the period of the three days of observation. In order to compare the fields at the three consecutive days quantitatively, we compute the vector correlations between the three field configurations using Eq. (4.8). The correlations (C_{vec}) of the 3D magnetic field vectors of March 28 and 30 with respect to the one on March 29 are 0.96 and 0.93 respectively. From these values we can see that there has been no major change in the magnetic field configuration during this period. We also compute the values of the free magnetic energy estimated from the excess energy of the extrapolated field. For the corresponding potential and force-free magnetic field, we can then estimate an upper limit to the free magnetic energy associated with coronal currents using Eq. (4.9). The free energy on all three days is about 3.5×10^{32}erg. The magnetic energy associated with the potential field configuration is about 54×10^{32}erg. Hence E_{nlff} exceeds E_{pot} by only 6%. Table 4.4 shows the magnetic energy associated with potential and extrapolated NLFF field configurations. Fig. 4.9 shows Iso-surface plots of magnetic energy density above the volume of the active regions. There are strong energy concentrations above each active region. There were no major changes in the energy density over the observation period and there was no major eruptive phenomenon during those three days in the region observed.

The three ARs share a decent amount of magnetic flux compared to their internal flux from one polarity to the other (see Fig. 4.8). In terms of the electric current they are much more isolated. In order to quantify these connectivities, we have calculated the magnetic

[3]http://solis.nso.edu/solis data.html
[4]http://sohowww.nascom.nasa.gov/data/archive

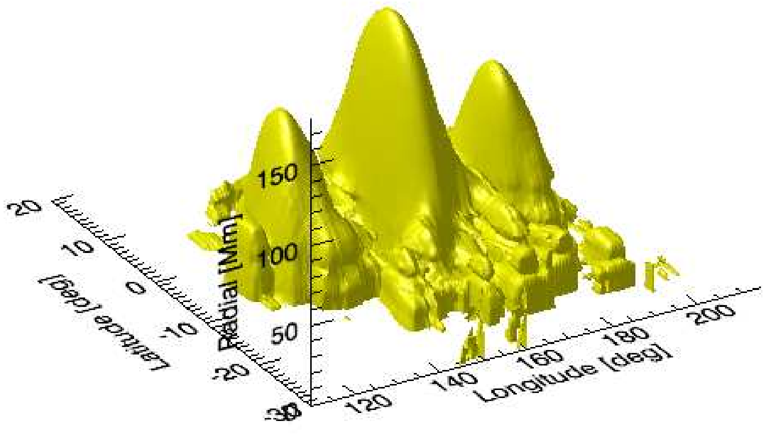

(a) March 28 2008 15:45UT

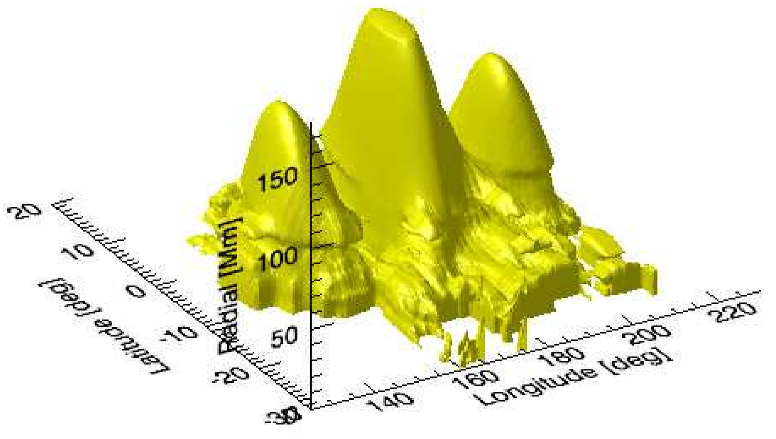

(b) March 29 2008 15:48UT

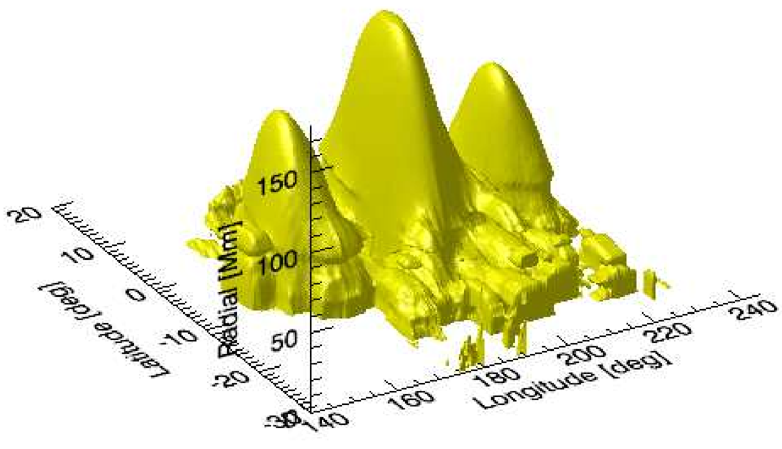

(c) March 30 2008 15:47UT

Figure 4.9: Iso-surfaces (ISs) of the absolute NLFF magnetic energy densities for the three consecutive dates computed within the entire computational domain.

Table 4.5: The percentage of the total magnetic flux shared between the three ARs. Φ_1, Φ_2 & Φ_3 denote magnetic flux of AR 10989(left), AR 10988(middle) & AR 10987(right) of Fig. 4.6, respectively.

	28^{th}			29^{th}			30^{th}		
$\Phi_{\alpha\beta}$	$\alpha = 1$	2	3	$\alpha = 1$	2	3	$\alpha = 1$	2	3
$\beta = 1$	56.37	5.59	0.00	56.50	5.48	0.00	56.50	5.48	0.00
2	13.66	81.12	1.43	13.66	81.22	1.43	13.66	81.22	2.22
3	0.00	0.48	71.47	0.00	0.48	71.80	0.00	0.48	71.80
Elsewhere	29.97	12.82	27.10	29.84	12.82	26.77	29.84	12.82	25.98

Table 4.6: The percentage of the total electric current shared between the three ARs. I_1, I_2, & I_3 denote elecrtic current of AR 10989(left), AR 10988(middle) & AR 10987(right) of Fig. 4.6, respectively.

	28^{th}			29^{th}			30^{th}		
$I_{\alpha\beta}$	$\alpha = 1$	2	3	$\alpha = 1$	2	3	$\alpha = 1$	2	3
$\beta = 1$	82.47	0.19	0.00	86.36	0.19	0.00	94.16	0.19	0.00
2	0.65	85.25	1.42	0.65	85.25	1.42	0.65	85.25	3.55
3	0.00	0.38	82.27	0.00	0.38	82.27	0.00	0.38	82.27
Elsewhere	16.88	14.18	16.31	12.99	14.18	16.31	5.19	14.18	14.18

flux and the electric currents shared between active regions. For the magnetic flux, e.g., we use

$$\Phi_{\alpha\beta} = \sum_i |\mathbf{B}_i \cdot \hat{r}| R_\odot^2 \sin(\theta_i) \Delta\theta_i \Delta\phi_i \tag{4.10}$$

where the summation is over all pixels of AR α from which the field line ends in AR β. For the electric current we replace the magnetic field, B, by the vertical current density $\mathbf{J}_i \cdot \hat{r}$ in equation (4.10). For every pixel in a single active region, we plot the field line and locate its end point. Whenever the end point of a field line falls outside the three ARs, we categorize it as ending elsewhere. Finally, we calculate total magnetic flux and electric currents for those pixels with field lines ending at the same region somewhere (it can be either in the same active region, other ARs or elsewhere). Both table 4.5 and 4.6 show the percentage of the total magnetic flux and electric current shared between the three ARs. The three active regions are magnetically connected but much less by electric currents.

4.6 Summary and conclusions

We have investigated the coronal magnetic field associated with the AR 11017 on 2009 May 15 together with neighbouring active region and three ARs 10987, 10987, 10989, on 2008 March 28, 29 and 30 by analysing SOLIS/VSM data. We have used the optimization method for the reconstruction of nonlinear force-free coronal magnetic fields in spherical geometry by restricting the code to limited parts of the Sun (Wiegelmann 2007, Tadesse et al. 2009). Different from previous implementations our new code allows us to deal with missing data and regions with poor signal-to-noise ratio in the extrapolation in a systematic manner. It produces a field which is closer to a force- and divergence-free field and tries to match the boundary only where it has been reliably measured (adapted from the cartesian version as described in Wiegelmann and Inhester 2010).

With the new $\mathcal{L}_{\text{photo}}$ term extrapolation from $\tilde{\boldsymbol{B}}_{\text{obs}}$ and $\tilde{\boldsymbol{B}}$(preprocessed boundary field) yields almost the same 3D field. However, in the latter case the iteration to minimize Eq. (4.4) converges in fewer iteration steps. At the same time, preprocessing does not affect the overall configuration of magnetic field and its total energy content.

We have studied the time evolution of magnetic field over the period of the three days observed on March 28, 29, and 30 2008 and found no major changes in topologies as there was no major eruption event. The magnetic energies calculated in the large wedge-shaped computational box above the three active regions were not far apart in value. This is the first study which is extrapolated NLFFF from three well separated ARs. This was made possible by the use of spherical coordinates and it allows us to analyse linkage between the ARs. The active regions share a decent amount of magnetic flux compared to their internal flux from one polarity to the other. In terms of the electric current they are much more isolated.

5 Conclusions and outlook

The structure and evolution of the coronal magnetic field (and the associated electric currents) that permeates the solar atmosphere play key roles in a variety of dynamical processes observed to occur on the Sun. Such processes range from the appearance of extreme ultraviolet (EUV) and X-ray bright points, to brightenings associated with nanoflare events, to the confinement and redistribution of coronal loop plasma, to reconnection events, to X-ray flares, to the onset and liftoff of the largest mass ejections. It is believed that many of these observed phenomena depend on the configurations of the magnetic field, and thus knowledge of the field configuration is becoming an increasingly important factor in discriminating between different classes of events. The coronal magnetic field topology is thought to be a critical factor in determining, for example, why some active regions flare, why others do not, how filaments form, and many other topics of interest. Within this thesis, we used a numerical method to extrapolate the magnetic field above solar active regions from vector magnetic field measurements made in the solar photosphere. Our method is based on the force-free assumption, i.e. the adoption that the coronal currents are co-aligned with the magnetic field. Potential (current-free) and nonlinear force-free field models were used to calculate the coronal magnetic field, where the latter represents the currently most sophisticated and most realistic approximation to the true static coronal magnetic field.

A successful application of nonlinear force-free field models to real solar data, in general, requires a number of prerequisites. This was concluded by DeRosa et al. (2009) who applied different existing nonlinear force-free codes to data from the Hinode Solar Optical Telescope-SpectroPolarimeter (Hinode/SOT-SP) and where the resulting models showed remarkable differences in the field line configuration and estimates of the free magnetic energy. In the following, the requirements for a successful application of extrapolation techniques to model the coronal magnetic field are listed along with the effort we have made in this work to incorporate them.

First, large model volumes at high spatial resolution are required to accommodate the magnetic connectivity within an active region and the surrounding environment. This requirement can only be met if the computational box for the field extrapolation is enhanced beyond a size where the solar spherical geometry can be neglected. In this work, we have developed and tested the optimization method for the reconstruction of nonlinear force-free coronal magnetic fields in spherical geometry by restricting the code to limited parts of the Sun, as suggested by Wiegelmann (2007). The optimization method minimizes a functional consisting of a quadratic form of the force balance and the solenoidal condition. Without a weighting function, all the six boundaries are equal likely to influence the solution. The effect of top and lateral boundaries can be reduced by introducing a boundary layer around the physical domain (Wiegelmann 2004). The physical domain is a wedge-shaped area within which we reconstruct the coronal magnetic field that is consistent with the photospheric vector magnetogram data. The boundary layer replaces the hard lateral and top boundary used previously. In the physical domain, the weighting function is unity. It drops monotonically in the boundary layer and reaches zero at the boundary of the computational box. At the boundary of the computational box, we set the field to have the value of the potential field computed from B_r at the bottom boundary. Our test calculations show that a finite-sized weighted boundary yields far more reliable results. The depth *nd* of this buffer boundary influences the quality of reconstruction, since the magnetic flux in these test cases is not concentrated well inside the interior of the box. In this way we will achieve a consistent connectivity of the local active region magnetic field with the global field structure.

Second, the preprocessing of the lower-boundary (photospheric) vector field is necessary in order to gain boundary conditions consistent with the force-free assumption. The assumption of force-free magnetic field models is that the magnetic pressure is considerably higher than the plasma pressure in the solar atmosphere. As this condition is not true for the photosphere, non-magnetic forces can in principle not be neglected and the photospheric magnetic field provides an inconsistent lower boundary condition for the force-free extrapolation codes. The preprocessing ensures the transformation of the observed (not force-free) photospheric field to a (nearly force-free) chromospheric-like field in order to approximate the physics in the solar atmosphere at a chromospheric level. In this work, we have presented a method for preprocessing vector magnetogram data input so that the result is suitable for a nonlinear force-free magnetic field extrapolation with help of an optimization code in spherical geometry. We extended the preprocessing routine developed by Wiegelmann et al. (2006) to spherical geometry for large field of view (Tadesse et al. 2009). As a first test of the method, we use the Low and Lou solution with noise added from different noise models. A direct use of the noisy photospheric data for a nonlinear force-free extrapolation showed no good agreement with the original semi-analytic Low and Lou solution (Low and Lou 1990), but after applying our newly developed preprocessing method we obtained a reasonable agreement with the original. The preprocessing method changes the boundary data within their noise limits to drive the magnetogram towards boundary conditions that are consistent with the assumption of a force-free field above. The transverse field components with higher noise level are modified more than the radial components. To carry out the preprocessing, we use a minimization principle. On the one hand, we control the final boundary data to be as close as possible (within the noise level) to the original measured data, and the data are forced to fulfill the consistency criteria and to be sufficiently smooth. Smoothness of the boundary data is required by the nonlinear force-free extrapolation code, but is also necessary physically because the magnetic field at the basis of the corona should be smoother than in the photosphere, where it is measured. In addition, we found that adding a larger amount of noise to the magnetogram decreases its vector correlation with the model reference field whenever we reconstruct it without preprocessing.

Third, the measurement uncertainties in the lower boundary conditions need to be addressed. This, in particular, concerns the transverse magnetic field measurements which posses a much lower level of accuracy than the longitudinal ones. We solve the nonlinear force-free field equations by minimizing a functional in spherical coordinates over a restricted area of the solar surface. We extend the functional by an additional term, which allows to incorporate measurement errors and treat regions with missing observational data. We have applied our new algorithms to vector magnetograph data from the Synoptic Optical Long-term Investigations of the Sun survey (SOLIS). We study two neighbouring magnetically connected active regions observed on May 15 2009 and three neighbouring active regions observed on March 28-30 2008. For vector magnetograms with variable measurement precision and randomly scattered data gaps (e.g., SOLIS/VSM) the new code yields field models which satisfy the solenoidal and force-free condition significantly better as it allows deviations between the extrapolated boundary field and observed boundary data within measurement errors. Data gaps are assigned to an infinite error. We extend this new scheme to spherical geometry and apply it for the first time to real data. As field of view of observations are getting large, one can use this newly developed spherical code for full-disk data from SDO (Solar Dynamics Observatory)/HMI (Helioseismic and Magnetic Imager) and other ground-based observations.

Further improvement to reasonably approximate the force-free magnetic field at the base of the corona is expected to be achieved by the supplementary incorporation of routinely measured, chromospheric, line-of-sight magnetic field data, e.g., from Synoptic Optical Long-term Investigations of the Sun (SOLIS). Since extrapolation is ill-posed, the reconstructed magnetic field becomes more uncertain at the larger distance from the solar surface. We therefore hope that magnetic field observations in the corona, even if they are indirect, will constrain and stabilize the extrapolation at greater altitudes. This could be achieved by

1. constraining the direction of the magnetic field along stereoscopically reconstructed loops. Even if these additional measurements are sparse, they may influence the computed magnetic field in the whole volume. It is well know, e.g., that for solenoidal fields, the boundary conditions are influential throughout the whole volume of the computational box.

2. constraining the magnetic field by coronal measurements of Stokes vectors of Infrared (IR) lines. These observations are line-of-sight (LOS) integrated and they are not easy to interpret directly, but they could be incorporated in the functional $\mathcal{L}$ (Eq. 3.1) by an additional term $\int_{\mathrm{LOS}} \left(I_{\mathrm{obs}} - I_{\mathrm{theory}}(B, n, T)\right)^2 dl$, where $\boldsymbol{I} = \{Q, U, V\}$ are the Stokes components or line moments thereof. Unfortunately, they are not only sensetive to the magnetic field $\mathbf{B}$ but also depend on the plasma density n, and temperature T. This method requires an a-priori coronal density and temperature model. Alternatively we can slove for some combination of n and T using coronagraph data and the Stokes I-components.

A Appendix

A.1 Derivation of $\tilde{F}$ and $\tilde{G}$ in Eq. (3.4)

$$\mathcal{L}_\omega(\bar{\boldsymbol{B}}, \tilde{\boldsymbol{B}}) = \int_V \omega(r,\theta,\phi) B^{-2}\Big(\Omega_a^2 + \Omega_b^2\Big) r^2 \sin\theta \, dr\, d\theta\, d\phi \tag{A.1}$$

$$\Omega_a = B^{-2}(\nabla \times \boldsymbol{B}) \times \boldsymbol{B}\,, \tag{A.2}$$

$$\Omega_b = B^{-2}(\nabla \cdot \boldsymbol{B})\boldsymbol{B} \tag{A.3}$$

where $\boldsymbol{B}$ is the discrete vector of all magnetic field components which we split into those of the interior, $\bar{\boldsymbol{B}}$, and those on the boundary $\tilde{\boldsymbol{B}}$. Let us vary $\mathcal{L}_\omega$ with respect to an iterative parameter t as:

$$\frac{d\mathcal{L}_\omega(\bar{\boldsymbol{B}}, \tilde{\boldsymbol{B}})}{dt} = \frac{d\mathcal{L}_\omega(\bar{\boldsymbol{B}}, \tilde{\boldsymbol{B}})}{d\overline{B}} \cdot \frac{\partial \bar{\boldsymbol{B}}}{\partial t} + \frac{d\mathcal{L}_\omega(\bar{\boldsymbol{B}}, \tilde{\boldsymbol{B}})}{d\widetilde{B}} \cdot \frac{\partial \tilde{\boldsymbol{B}}}{\partial t} \tag{A.4}$$

Here we have two terms one for inner domain and the second over the boundary and our aim is to separate all terms containing a product with $\partial\bar{\boldsymbol{B}}/\partial t$ and $\partial\tilde{\boldsymbol{B}}/\partial t$. This will allow us to provide explicit evolution equations for $\boldsymbol{B}$ to minimize $\mathcal{L}_\omega$.

$$\begin{aligned}
\frac{1}{2}\frac{d\mathcal{L}_\omega}{dt} = &- \int_V \omega\Omega_a \cdot \frac{\partial}{\partial t}[(\nabla \times \boldsymbol{B}) \times \boldsymbol{B}] r^2 \sin\theta \, dr\, d\theta\, d\phi \\
&+ \int_V \omega\Omega_b \cdot \frac{\partial}{\partial t}[(\nabla \cdot \boldsymbol{B})\boldsymbol{B}] r^2 \sin\theta \, dr\, d\theta\, d\phi \\
&- \int_V \omega(\Omega_a^2 + \Omega_b^2)\boldsymbol{B} \cdot \frac{\partial \boldsymbol{B}}{\partial t} r^2 \sin\theta \, dr\, d\theta\, d\phi
\end{aligned} \tag{A.5}$$

The third term has the correct form we need already. Using the following vector identities and Gauss's Law, one can re-formulate the first and the second term as required. Given three vectors $\boldsymbol{a}$, $\boldsymbol{b}$, and $\boldsymbol{c}$ and scalar function ψ

$$\boldsymbol{a} \cdot (\boldsymbol{b} \times \boldsymbol{c}) = \boldsymbol{b} \cdot (\boldsymbol{c} \times \boldsymbol{a}) = \boldsymbol{c} \cdot (\boldsymbol{a} \times \boldsymbol{b})\,, \tag{A.6}$$

$$(\nabla \times \boldsymbol{a}) \cdot \boldsymbol{b} = \boldsymbol{a} \cdot (\nabla \times \boldsymbol{b}) + \nabla \cdot (\boldsymbol{a} \times \boldsymbol{b})\,, \tag{A.7}$$

$$\psi\nabla \cdot \boldsymbol{a} = \nabla \cdot (\boldsymbol{a}\psi) - \boldsymbol{a} \cdot \nabla\psi\,, \tag{A.8}$$

$$\int_V (\nabla \cdot \boldsymbol{a}) dV = \int_S \boldsymbol{a} \cdot \hat{\boldsymbol{n}} dS\,, \tag{A.9}$$

where $\hat{\boldsymbol{n}}$ a unit vector normal to infinitesimal area dS. Let us expand the first and the second terms of Eq. (A.5), respectively as follows:

$$\int_V \omega\Omega_a \cdot \frac{\partial}{\partial t}[(\nabla\times\boldsymbol{B})\times\boldsymbol{B}]dV = \int_V \omega\Omega_a \cdot \Big[(\nabla\times\frac{\partial\boldsymbol{B}}{\partial t})\times\boldsymbol{B}\Big]r^2\sin\theta\,dr\,d\theta\,d\phi + \int_V \omega\Omega_a \cdot \Big[(\nabla\times\boldsymbol{B})\times\frac{\partial\boldsymbol{B}}{\partial t}\Big]r^2\sin\theta\,dr\,d\theta\,d\phi \tag{A.10}$$

Hence applying Eqs. (A.6)-(A.9), one can simplify Eq. (A.10) to the form:

$$\begin{aligned}\int_V \omega\Omega_a \cdot \frac{\partial}{\partial t}[(\nabla\times\boldsymbol{B})\times\boldsymbol{B}]dV = &-\int_V [\omega\nabla\times(\Omega_a\times\boldsymbol{B})]\cdot\frac{\partial\bar{\boldsymbol{B}}}{\partial t}r^2\sin\theta\,dr\,d\theta\,d\phi\\ &-\int_S [\omega\hat{\boldsymbol{n}}\times(\Omega_a\times\boldsymbol{B})]\cdot\frac{\partial\bar{\boldsymbol{B}}}{\partial t}dS\\ &+\int_V [\nabla\omega\times(\Omega_a\times\boldsymbol{B})]\cdot\frac{\partial\bar{\boldsymbol{B}}}{\partial t}r^2\sin\theta\,dr\,d\theta\,d\phi\\ &+\int_V [\Omega_a\times\nabla\times\boldsymbol{B})]\cdot\frac{\partial\bar{\boldsymbol{B}}}{\partial t}r^2\sin\theta\,dr\,d\theta\,d\phi\end{aligned} \tag{A.11}$$

Similarly we can decouple the second term of Eq. (A.5) as follows:

$$\begin{aligned}\int_V \omega\Omega_b \cdot \frac{\partial}{\partial t}[(\nabla\cdot\boldsymbol{B})\boldsymbol{B}]r^2\sin\theta\,dr\,d\theta\,d\phi = &\\ -\int_V \omega\nabla(\Omega_b\cdot\boldsymbol{B})\cdot\frac{\partial\bar{\boldsymbol{B}}}{\partial t}r^2\sin\theta\,dr\,d\theta\,d\phi &\\ +\int_S \hat{\boldsymbol{n}}(\omega\Omega_b\cdot\boldsymbol{B})\cdot\frac{\partial\bar{\boldsymbol{B}}}{\partial t}dS &\\ -\int_V [(\Omega_b\cdot\boldsymbol{B})\nabla\omega]\cdot\frac{\partial\bar{\boldsymbol{B}}}{\partial t}r^2\sin\theta\,dr\,d\theta\,d\phi &\\ +\int_V \omega[\Omega_b(\nabla\cdot\boldsymbol{B})\cdot\frac{\partial\bar{\boldsymbol{B}}}{\partial t}r^2\sin\theta\,dr\,d\theta\,d\phi &\end{aligned} \tag{A.12}$$

Substituting back Eqs. (A.11) and (A.12) into Eq. (A.5) and collecting the terms under volume and surface intergrals separately we can rearrange Eq. (A.5) as follows:

$$\frac{1}{2}\frac{d\mathcal{L}_\omega}{dt} = -\int_V \frac{\partial\bar{\boldsymbol{B}}}{\partial t}\cdot\tilde{\boldsymbol{F}}\;r^2\sin\theta\,dr\,d\theta\,d\phi - \int_S \frac{\partial\bar{\boldsymbol{B}}}{\partial t}\cdot\tilde{\boldsymbol{G}}dS \tag{A.13}$$

where

$$\tilde{\boldsymbol{F}} = \omega\boldsymbol{F} + (\Omega_a\times\boldsymbol{B})\times\nabla\omega + (\Omega_b\cdot\boldsymbol{B})\nabla\omega\,, \tag{A.14}$$

$$\tilde{\boldsymbol{G}} = \omega\boldsymbol{G} \tag{A.15}$$

$$\boldsymbol{F} = \nabla\times(\Omega_a\times\boldsymbol{B}) - \Omega_a\times(\nabla\times\boldsymbol{B}) + \nabla(\Omega_b\cdot\boldsymbol{B}) - \Omega_b(\nabla\cdot\boldsymbol{B}) + (\Omega_a^2+\Omega_b^2)\boldsymbol{B}\,, \tag{A.16}$$

$$\boldsymbol{G} = \hat{\boldsymbol{n}}\times(\Omega_a\times\boldsymbol{B}) - \hat{\boldsymbol{n}}(\Omega_b\cdot\boldsymbol{B}) \tag{A.17}$$

A.2 Finite difference scheme

A finite-difference approximation is one of the commonly used methods for numerical solution of ordinary and partial differential equations. The approximations most often used have second-order accuracy. The order of accuracy can be increased either by using higher-order finite difference approximations. The goal is to approximate solutions to differential equations, i.e., to find a function (or some discrete approximation to this function) which satisfies a given relationship between various of its derivatives on some given region of space and/or time, along with some boundary conditions along the edges of this domain. A finite difference method proceeds by replacing the derivatives in the differential equations by finite difference approximations. This gives a large algebraic system of equations to be solved in place of the differential equation, something that is easily solved on a computer. Let first consider the more basic question of how we can approximate the derivatives of a known function by finite difference formulas based only on values of the function itself at discrete points.

Let us introduce a non uniform finite-difference mesh for x. Let N be be the number of discretisation points for x. We denote $u(x_i)$ by u_i at the grid point x_i, where $u(x_i)$ is the exact solution of the partial differential equation at this point. h_i is the distance between adjacent grid points where $h_i = x_i - x_{i-1}$. Let $u(x)$ represent a function of one variable that, unless otherwise stated, will always be assumed to be smooth, meaning that we can differentiate the function several times and each derivative is a well-defined bounded function over an interval containing a particular point of interest x. Let us expand $u(x)$ using Taylor expansion as follows:

$$u_{i+1} = u_i + h_{i+1}u'_i + \frac{1}{2}h_{i+1}^2 u''_i + \frac{1}{6}h_{i+1}^3 u'''_i + O(h_{i+1}^4) \tag{A.18}$$

$$u_{i+2} = u_i + (h_{i+1}+h_{i+2})u'_i + \frac{1}{2}(h_{i+1}+h_{i+2})^2 u''_i + \frac{1}{6}(h_{i+1}+h_{i+2})^3 u'''_i + O((h_{i+1}+h_{i+2})^4) \tag{A.19}$$

$$u_{i-1} = u_i - h_i u'_i + \frac{1}{2}h_i^2 u''_i - \frac{1}{6}h_i^3 u'''_i + O(h_i^4) \tag{A.20}$$

$$u_{i-2} = u_i - (h_i + h_{i-1})u'_i + \frac{1}{2}(h_i + h_{i-1})^2 u''_i - \frac{1}{6}(h_i + h_{i-1})^3 u'''_i + O((h_i + h_{i-1})^4) \tag{A.21}$$

Using the first two equations one can find the first derivative of $u(x)$ as:

$$u'_i = \frac{u_{i+1} - u_i}{h_{i+1}} + O(h_{i+1}) \tag{A.22}$$

$$u'_i = \frac{u_i - u_{i-1}}{h_i} + O(h_i) \tag{A.23}$$

where Eqs. (A.22) and (A.23), are termed as forward and backward differences, respectively. In order to find the second order approximation of first derivative of $u(x)$ at node x_i using the points x_{i-1}, x_i, and x_{i+1}, let us write u'_i in the form of

$$u'_i = au_{i-1} + bu_i + cu_{i+1} \tag{A.24}$$

where a,b, and c are constants. By substituting Eqs. (A.18) and (A.20) into Eq. (A.24) and calculating for the constants a,b, and c one one can find:

$$u_i' = \frac{-h_{i+1}^2 u_{i-1} + (h_{i+1}^2 - h_i^2)u_i + h_i^2 u_{i+1}}{h_i h_{i+1}(h_i + h_{i+1})} \tag{A.25}$$

The left-sided, second order approximation of first derivative of $u(x)$ at node x_i using the points x_i, x_{i+1}, and x_{i+2} can calculated by:

$$u_i' = au_i + bu_{i+1} + cu_{i+2} \tag{A.26}$$

Substituting Eqs. (A.18) and (A.19) into Eq. (A.26) and calculating for the constants a,b, and c one one can find:

$$u_i' = \frac{-h_{i+2}(h_{i+2} + 2h_{i+1})u_i + (h_{i+2} + h_{i+1})^2 u_{i+1} - h_{i+1}^2 u_{i+2}}{h_{i+1}h_{i+2}(h_{i+1} + h_{i+2})} \tag{A.27}$$

Similarly one can calculate the right-sided, second order approximation of first derivative of $u(x)$ at node x_i from the points x_i, x_{i-1}, and x_{i-2} using Eqs. (A.20) and (A.21) as

$$u_i' = \frac{h_i^2 u_{i-2} - (h_{i-1} + h_i)^2 u_{i-1} + h_{i-1}(h_{i-1} + 2h_i)u_i}{h_i h_{i-1}(h_{i-1} + h_i)} \tag{A.28}$$

The rightand left-sided approximations of the derivatives help us to find the derivative of a function without consodering points outside the computational domain.

The second order approximation of second derivative of $u(x)$ on a standard 3-points stencil can be found just by adding Eqs. (A.18) and (A.20) and rearranging terms for u_i'' as:

$$u_i'' = \frac{d^2u(x_i)}{dx^2} = 2\frac{h_i(u_{i+1} - u_i) - h_{i+1}(u_i - u_{i-1})}{h_i h_{i+1}(h_i + h_{i+1})} \tag{A.29}$$

A.3 Partial derivative of L_4

We derive the partial derivative of L_4 with respect to each of the three magnetic field components in its discretized form as indicated in Eqs.(3.54)-(3.56). We used a five-point stencil on the photospheric boundary for Laplace in L_4. Those derivatives are carried out at every node (q) of the bottom boundary grid. The partial derivative of Eq. (3.52) with respect to B_r, for instance can be written as

$$\frac{\partial L_4}{\partial (B_r)_q} = 2\sum_p (\Delta B_r)_p \frac{\partial}{\partial (B_r)_q}(\Delta B_r)_p \tag{A.30}$$

We demonstrated the effect of the derivative by using the conventional Laplacian ΔB_r in one dimension using three-point stencil with geometry-dependent coefficients c & a. Then

$$(\Delta B_r)_p = a(B_r)_{p-1} + c(B_r)_p + a(B_r)_{p+1}, \tag{A.31}$$

and after substituting Eq.(A.31) into the derivative term in Eq.(A.30), we find

$$\begin{aligned}\frac{\partial}{\partial(B_r)_q}(\Delta B_r)_p =&\frac{\partial}{\partial(B_r)_q}\left(a(B_r)_{p-1} + c(B_r)_p + a(B_r)_{p+1}\right)\\ =&a\delta_{p-1,q} + c\delta_{p,q} + a\delta_{p+1,q}\end{aligned} \tag{A.32}$$

Therefore, using equation Eq.(A.32), we can reduce Eq.(A.30) to

$$\begin{aligned}\frac{\partial L_4}{\partial(B_r)_q} =&2\sum_p(\Delta B_r)_p(a\delta_{p-1,q} + c\delta_{p,q} + a\delta_{p+1,q})\\ =&2\sum_p\left[a(\Delta B_r)_{q+1} + c(\Delta B_r)_q + a(\Delta B_r)_{q-1}\right]\\ =&2\sum_p\left(\Delta(\Delta B_r)\right)_q.\end{aligned} \tag{A.33}$$

One can similarly derive the partial derivative of L_4 with respect to the other two field components.

Bibliography

Alfven, H., 1950, Cosmical electrodynamics, International Series of Monographs on Physics, Oxford: Clarendon Press

Alissandrakis, C. E., 1981, On the computation of constant alpha force-free magnetic field, A&A, 100, 197–200

Aly, J. J., 1984, On some properties of force-free magnetic fields in infinite regions of space, ApJ, 283, 349–362

Aly, J. J., 1988, Some properties of the solutions of a non-linear boundary value problem for a force-free field in an infinite region of space. I - Energy estimates, A&A, 203, 183–188

Aly, J. J., 1989, On the reconstruction of the nonlinear force-free coronal magnetic field from boundary data, Sol. Phys., 120, 19–48

Aly, J. J., 1992, Some properties of finite energy constant-alpha force-free magnetic fields in a half-space, Sol. Phys., 138, 133–162

Amari, T., Luciani, J. F., Aly, J. J., Tagger, M., 1996, Very Fast Opening of a Three-dimensional Twisted Magnetic Flux Tube, ApJL, 466, L39

Amari, T., Aly, J. J., Luciani, J. F., Boulmezaoud, T. Z., Mikic, Z., 1997, Reconstructing the Solar Coronal Magnetic Field as a Force-Free Magnetic Field, Sol. Phys., 174, 129–149

Amari, T., Boulmezaoud, T. Z., Mikic, Z., 1999, An iterative method for the reconstructionbreak of the solar coronal magnetic field. I. Method for regular solutions, A&A, 350, 1051–1059

Amari, T., Boulmezaoud, T. Z., Aly, J. J., 2006, Well posed reconstruction of the solar coronal magnetic field, A&A, 446, 691–705

Ambrož, P., Schroll, A., 2002, Proper motion of solar filaments, A&A, 381, 300–310

Arnaud, J., Newkirk, Jr., G., 1987, Mean properties of the polarization of the Fe XIII 10747 A coronal emission line, A&A, 178, 263–268

Aschwanden, M. J., 2005, Physics of the Solar Corona. An Introduction with Problems and Solutions (2nd edition), Praxis Publishing, Chichester, UK

Aschwanden, M. J., Newmark, J. S., Delaboudinière, J., Neupert, W. M., Klimchuk, J. A., Gary, G. A., Portier-Fozzani, F., Zucker, A., 1999, Three-dimensional Stereoscopic Analysis of Solar Active Region Loops. I. SOHO/EIT Observations at Temperatures of (1.0-1.5) X 10^6 K, ApJ, 515, 842–867

Aschwanden, M. J., Wülser, J.-P., Nitta, N. V., Lemen, J. R., 2008, First Three-Dimensional Reconstructions of Coronal Loops with the STEREO A and B Spacecraft. I. Geometry, ApJ, 679, 827–842

Auer, L. H., House, L. L., Heasley, J. N., 1977, The determination of vector magnetic fields from Stokes profiles, Sol. Phys., 55, 47–61

Barbosa, D. D., 1978, Linear force-free fields in the lower corona, Sol. Phys., 56, 55–66

Beckers, J. M., 1971, The Measurement of Solar Magnetic Fields, in Solar Magnetic Fields, (Ed.) R. Howard, vol. 43 of IAU Symposium, pp. 3

Benz, A. (Ed.), 2002, Plasma Astrophysics, second edition, vol. 279 of Astrophysics and Space Science Library, Kluwer Academic publishers.

Bhatnagar, A., Livingston, W., 2005, Fundamentals of solar astronomy, *World Scientific Series in Astronomy and Astrophysics*, Vol. 6, New Jersey, London, Singapore: World Scientific. ISBN 981-238-244-5.

Bray, R. J., Cram, L. E., Durrant, C., Loughhead, R. E., 1991, Plasma Loops in the Solar Corona, pp. 522. ISBN 0521351073. Cambridge, UK: Cambridge University Press.

Brekke, P., Kjeldseth-Moe, O., Harrison, R. A., 1997, High-Velocity Flows in an Active Region Loop System Observed with the Coronal Diagnostic Spectrometer (Cds) on SOHO, Sol. Phys., 175, 511–521

Cadez, V. M., 2005, Modeling Static Magnetic Field Structures in Solar Corona, Serbian Astronomical Journal, 171, 1–10

Canfield, R. C., de La Beaujardiere, J., Fan, Y., Leka, K. D., McClymont, A. N., Metcalf, T. R., Mickey, D. L., Wuelser, J., Lites, B. W., 1993, The morphology of flare phenomena, magnetic fields, and electric currents in active regions. I - Introduction and methods, ApJ, 411, 362–369

Chiu, Y. T., Hilton, H. H., 1977, Exact Green's function method of solar force-free magnetic-field computations with constant alpha. I - Theory and basic test cases, ApJ, 212, 873–885

Chodura, R., Schlueter, A., 1981, A 3-D code for MHD equilibrium and stability, J. of comp. phys., 41, 68–88

Clegg, J. R., Browning, P. K., Laurence, P., Bromage, B. J. I., Stredulinsky, E., 2000, The linear force-free field in a spherical shell using a new method to determine the coefficients of the eigenfunction expansion, A&A, 361, 743–758

Condon, E. U., Shortley, G. H., 1970, The theory of atomic spectra, Cambridge: Cambridge University Press.

Crouch, A. D., Barnes, G., 2008, Resolving the Azimuthal Ambiguity in Vector Magnetogram Data with the Divergence-Free Condition: Theoretical Examination, Sol. Phys., 247, 25–37

Cuperman, S., Demoulin, P., Semel, M., 1991, Removal of singularities in the Cauchy problem for the extrapolation of solar force-free magnetic fields, A&A, 245, 285–288

Cuperman, S., Li, J., Semel, M., 1992, Magnetic shear-based removal of the 180-deg ambiguity in the observed transverse photospheric magnetic field - Feasibility and limitations, A&A, 265, 296–307

Cuperman, S., Li, J., Semel, M., 1993, Identification and elimination of the residual ambiguity in the sign of observed photospheric magnetic fields, A&A, 278, 279–287

Demoulin, P., Cuperman, S., Semel, M., 1992, Determination of force-free magnetic fields above the photosphere using three-component boundary conditions. II - Analysis and minimization of scale-related growing modes and of computational induced singularities, A&A, 263, 351–360

DeRosa, M. L., Schrijver, C. J., Barnes, G., Leka, K. D., Lites, B. W., Aschwanden, M. J., Amari, T., Canou, A., McTiernan, J. M., Régnier, S., Thalmann, J. K., Valori, G., Wheatland, M. S., Wiegelmann, T., Cheung, M. C. M., Conlon, P. A., Fuhrmann, M., Inhester, B., Tadesse, T., 2009, A Critical Assessment of Nonlinear Force-Free Field Modeling of the Solar Corona for Active Region 10953, ApJ, 696, 1780–1791

Derouich, M., Auchère, F., Vial, J. C., Zhang, M., 2010, Hanle signatures of the coronal magnetic field in the linear polarization of the hydrogen Lα line, A&A, 511, A7

Domingo, V., 2002, SOHO, Yohkoh, Ulysses and Trace: The four solar missions in perspective, and available resources, Astrophysics and Space Science, 282, 171–188

Fuhrmann, M., Seehafer, N., Valori, G., 2007, Preprocessing of solar vector magnetograms for force-free magnetic field extrapolation, A&A, 476, 349–357

Gary, G. A., 1989, Linear force-free magnetic fields for solar extrapolation and interpretation, Astrophys. Journal Suppl. Ser., 69, 323–348

Gary, G. A., 2001, Plasma Beta above a Solar Active Region: Rethinking the Paradigm, Sol. Phys., 203, 71–86

Gary, G. A., Demoulin, P., 1995, Reduction, analysis, and properties of electric current systems in solar active regions, ApJ, 445, 982–998

Georgoulis, M. K., 2005, A New Technique for a Routine Azimuth Disambiguation of Solar Vector Magnetograms, ApJL, 629, L69–L72

Gold, T., Hoyle, F., 1960, On the origin of solar flares, MNRAS, 120, 89

Grad, H., Rubin, H., 1958, Hydromagnetic equilibria and force-free fields, paper presented at 2nd International Conference on Peaceful Uses of Atomic Energy, Int. At. Energy Agency, Geneva.

Hagyard, M. J., 1985, Measurements of solar vector magnetic fields. Proceedings of a workshop held at the George C. Marshall Space Flight Center, Huntsville, Alabama, USA., NASA Conf. Publ.

Hale, G. E., 1908, On the Probable Existence of a Magnetic Field in Sun-Spots, ApJ, 28, 315

Hanle, W., 1924, Über magnetische Beeinflussung der Polarisation der Resonanzfluoreszenz, Z. Phys., 30, 93

Harvey, J. W., 1969, Magnetic Fields Associated with Solar Active-Region Prominences., Ph.D. thesis, University of Colorado at Boulder.

Henney, M. H., Keller, U. C., Harvey, J. W., 2008, in ASP Conf. Ser. 383., p. 107

Herzberg, G., 1950, Molecular spectra and molecular structure. Vol.1: Spectra of diatomic molecules, New York: Van Nostrand Reinhold, 1950, 2nd ed.

Hoeksema, J. T., 1991, Large-scale solar and heliospheric magnetic fields, Adv. Space Res., 11, 15–24

House, L. L., 1977, Coronal emission-line polarization from the statistical equilibrium of magnetic sublevels. I - Fe XIII, ApJ, 214, 632–652

Ignace, R., Nordsieck, K. H., Cassinelli, J. P., 2004, The Hanle Effect as a Diagnostic of Magnetic Fields in Stellar Envelopes. IV. Application to Polarized P Cygni Wind Lines, ApJ, 609, 1018–1034

Inhester, B., Wiegelmann, T., 2006, Nonlinear Force-Free Magnetic Field Extrapolations: Comparison of the Grad Rubin and Wheatland Sturrock Roumeliotis Algorithm, Sol. Phys., 235, 201–221

Jackson, J. D., 1975, Classical electrodynamics, New York: Wiley, 2nd ed.

Jones, H. P., Harvey, J. W., Henney, C. J., Hill, F., Keller, U. C., 2002, in Magnetic Coupling of the Solar Atmosphere., ESA SP, 505, 15

Judge, P. G., 1998, Spectral Lines for Polarization Measurements of the Coronal Magnetic Field. I. Theoretical Intensities, ApJ, 500, 1009

Judge, P. G., Casini, R., Tomczyk, S., Edwards, D. P., Francis, E., 2001, Coronal Magnetometry: A Feasibility Study, NASA STI/Recon Technical Report N, 2, 27 999

Keller, U. C., Harvey, J. W., Giampapa, M. S., 2003, in Innovative Telescopes and Instrumentation for Solar Astrophysics., 4853, 194

Kramar, M., Inhester, B., 2006, On the tomography reconstruction of coronal force-free magnetic field, AGU Fall Meeting Abstracts, pp. B367

Kramar, M., Inhester, B., Solanki, S. K., 2006, Vector tomography for the coronal magnetic field. I. Longitudinal Zeeman effect measurements, A&A, 456, 665–673

Kuhn, J. R., MacQueen, R. M., Streete, J., Tansey, G., Mann, I., Hillebrand, P., Coulter, R., Lin, H., Edmunds, D., Judge, P., 1999, Probable Detection of a Bright Infrared Coronal Emission Line of Si IX near 3.93 Microns, ApJ, 521, 478–482

Landolfi, M., Landi Degl'Innocenti, E., Arena, P., 1984, On the diagnostic of magnetic fields in sunspots through the interpretation of Stokes parameters profiles, Sol. Phys., 93, 269–287

Lang, K. R., 2001, The Cambridge Encyclopedia of the Sun, The Cambridge Encyclopedia of the Sun, pp. 268. Cambridge, UK: Cambridge University Press.

Leake, J. E., Arber, T. D., 2006, The emergence of magnetic flux through a partially ionised solar atmosphere, A&A, 450, 805–818

Leka, K. D., Barnes, G., Crouch, A. D., Metcalf, T. R., Gary, G. A., Jing, J., Liu, Y., 2009, Resolving the 180deg Ambiguity in Solar Vector Magnetic Field Data: Evaluating the Effects of Noise, Spatial Resolution, and Method Assumptions, Sol. Phys., 260, 83–108

Lenz, D. D., Deluca, E. E., Golub, L., Rosner, R., Bookbinder, J. A., 1999, Temperature and Emission-Measure Profiles along Long-lived Solar Coronal Loops Observed with the Transition Region and Coronal Explorer, ApJL, 517, L155–L158

Leroy, J. L., 1985, The Hanle effect applied to magnetic field measurements, in Measurements of Solar Vector Magnetic Fields, (Ed.) M. J. Hagyard, pp. 121–140

Li, J., Amari, T., Fan, Y., 2007, Resolution of the 180-degree Ambiguity for Inverse Horizontal Magnetic Field Configurations, ApJ, 654, 675–686

Li, Z., Yan, Y., Song, G., 2004, Properties of the boundary integral equation for solar non-constant-α force-free magnetic fields, MNRAS, 347, 1255–1265

Liang, H. F., Ma, L., Zhao, H. J., Xiang, F. Y., 2009, Electric current density calculation and error analysis of solar active regions, New Astronomy, 14, 294–301

Lin, H., Penn, M. J., Tomczyk, S., 2000, A New Precise Measurement of the Coronal Magnetic Field Strength, ApJL, 541, L83–L86

Low, B. C., 1985, Modeling solar magnetic structures., NASA Conference Publication, 2374, 49–65

Low, B. C., Lou, Y. Q., 1990, Modeling solar force-free magnetic fields, ApJ, 352, 343–352

Mariska, J. T., 1993, The Solar Transition Region, Cambridge University press.

McClymont, A. N., Mikic, Z., 1994, Thickness variations along coronal loops inferred from vector magnetograph data, ApJ, 422, 899–905

Metcalf, T. R., 1994, Resolving the 180-degree ambiguity in vector magnetic field measurements: The 'minimum' energy solution, Sol. Phys., 155, 235–242

Metcalf, T. R., Leka, K. D., Barnes, G., Lites, B. W., Georgoulis, M. K., Pevtsov, A. A., Balasubramaniam, K. S., Gary, G. A., Jing, J., Li, J., Liu, Y., Wang, H. N., Abramenko, V., Yurchyshyn, V., Moon, Y., 2006, An Overview of Existing Algorithms for Resolving the 180-degree Ambiguity in Vector Magnetic Fields: Quantitative Tests with Synthetic Data, Sol. Phys., 237, 267–296

Metcalf, T. R., Derosa, M. L., Schrijver, C. J., Barnes, G., van Ballegooijen, A. A., Wiegelmann, T., Wheatland, M. S., Valori, G., McTtiernan, J. M., 2008, Nonlinear Force-Free Modeling of Coronal Magnetic Fields. II. Modeling a Filament Arcade and Simulated Chromospheric and Photospheric Vector Fields, Sol. Phys., 247, 269–299

Mickey, D. L., Canfield, R. C., Labonte, B. J., Leka, K. D., Waterson, M. F., Weber, H. M., 1996, The Imaging Vector Magnetograph at Haleakala, Sol. Phys., 168, 229–250

Mikic, Z., McClymont, A. N., 1994, Deducing Coronal Magnetic Fields from Vector Magnetograms, in Solar Active Region Evolution: Comparing Models with Observations, (Eds.) K. S. Balasubramaniam, G. W. Simon, vol. 68 of Astronomical Society of the Pacific Conference Series, pp. 225

Mikic, Z., Linker, J. A., Schnack, D. D., 1996, Modeling of Active-Region Magnetic Fields, in Solar Drivers of the Interplanetary and Terrestrial Disturbances, (Ed.) K. S. Balasubramaniam, S. L. Keil, & R. N. Smartt, vol. 95 of Astronomical Society of the Pacific Conference Series, pp. 108

Minarovjech, M., Rybansky, M., Rusin, V., 1998, Prominences and the Green Corona Over the Solar Activity Cycle, Sol. Phys., 177, 357–364

Mitchell, A. C. G., Zemansky, M. W., 1934, Resonance Radiation and Excited Atoms, Cambridge: Cambridge Univ. Press

Molodensky, M. M., 1969, Integral properties of force-free fields, Soviet Astron.-AJ, 12, 585–588

Molodensky, M. M., 1974, Equilibrium and stability of force-free magnetic field, Sol. Phys., 39, 393–404

Moon, Y., Wang, H., Spirock, T. J., Goode, P. R., Park, Y. D., 2003, A New Method for Resolving the 180-degree Ambiguity in Solar Vector Magnetograms, Sol. Phys., 217, 79–94

Nakagawa, Y., 1974, Dynamics of the Solar Magnetic Field. I. Method of Examination of Force-Free Magnetic Fields, ApJ, 190, 437–440

Nakagawa, Y., Raadu, M. A., 1972, On Practical Representation of Magnetic Field, Sol. Phys., 25, 127–135

Neukirch, T., 2005, Magnetic Field Extrapolation, in Chromospheric and Coronal Magnetic Fields, (Ed.) D. E. Innes, A. Lagg, & S. A. Solanki, vol. 596 of ESA Special Publication

Ossendrijver, M., 2003, The solar dynamo, Astron. Astrophys. Rev., 11, 287–367

Otto, A., Büchner, J., Nikutowski, B., 2007, Force-free magnetic field extrapolation for MHD boundary conditions in simulations of the solar atmosphere, A&A, 468, 313–321

Parker, E. N., 1979, Cosmical magnetic fields: Their origin and their activity, Oxford, Clarendon Press; New York, Oxford University Press, 1979, 858 p.

Parker, E. N., 2003, Foreword (Dynamic Sun), pp. D15+, Cambridge University press, ISBN 0 521 81057 4

Pevtsov, A. A., Canfield, R. C., Metcalf, T. R., 1994, Patterns of helicity in solar active regions, ApJL, 425, L117–L119

Priest, E. R., 1982a, Solar magneto-hydrodynamics., Geophysics and Astrophysics Monographs, 21

Priest, E. R., 1982b, Solar magneto-hydrodynamics, Kluwer Academic Pub

Raouafi, N., Solanki, S. K., Wiegelmann, T., 2009, Hanle Effect Diagnostics of the Coronal Magnetic Field: A Test Using Realistic Magnetic Field Configurations, vol. 405 of Astronomical Society of the Pacific Conference Series, pp. 429

Régnier, S., 2007, Nonlinear force-free field extrapolation: numerical methods and applications, MmSAI., 78, 126

Régnier, S., Priest, E. R., 2007a, Free Magnetic Energy in Solar Active Regions above the Minimum-Energy Relaxed State, ApJL, 669, L53–L56

Régnier, S., Priest, E. R., 2007b, Nonlinear force-free models for the solar corona. I. Two active regions with very different structure, A&A, 468, 701–709

Roumeliotis, G., 1996, The "Stress-and-Relax" Method for Reconstructing the Coronal Magnetic Field from Vector Magnetograph Data, ApJ, 473, 1095

Ruiz Cobo, B., del Toro Iniesta, J. C., 1992, Inversion of Stokes profiles, ApJ, 398, 375–385

Sahal-Brechot, S., 1981, The Hanle effect applied to magnetic field diagnostics., Space Sci. Rev., 29, 391–401

Sakurai, T., 1979, A New Approach to the Force-Free Field and Its Application to the Mag- netic Field of Solar Active Regions, Publ. Astron. Soc. Japan, 31, 209–230

Sakurai, T., 1981, Calculation of Force-Free Magnetic Field with Non Constant Alpha, Sol. Phys., 69, 343

Sakurai, T., 1989, Computational modeling of magnetic fields in solar active regions, Space Sci. Rev., 51, 11–48

Sakurai, T., 1994, Integrated Force-Balance Equations for the Magnetic Field in Spherical Geometry, in Solar Active Region Evolution: Comparing Models with Observations, (Eds.) K. S. Balasubramaniam, G. W. Simon, vol. 68 of Astronomical Society of the Pacific Conference Series, pp. 307

Sakurai, T., Ichimoto, K., Nishino, Y., Shinoda, K., Noguchi, M., Hiei, E., Li, T., He, F., Mao, W., Lu, H., Ai, G., Zhao, Z., Kawakami, S., Chae, J., 1995, Solar flare telescope at Mitaka, Publ. Astron. Soc. Japan, 47, 81–92

Sankarasubramanian, K., Penn, M., Pevtsov, A. (Eds.), 2005, Large-scale Structures and their Role in Solar Activity, vol. 346 of Astronomical Society of the Pacific Conference Series

Schmidt, H. U., 1964, On the Observable Effects of Magnetic Energy Storage and Release Connected With Solar Flares, in The Physics of Solar Flares, pp. 107

Schrijver, C. J., De Rosa, M. L., 2003, Photospheric and heliospheric magnetic fields, Sol. Phys., 212, 165–200

Schrijver, C. J., De Rosa, M. L., Title, A. M., Metcalf, T. R., 2005, The Nonpotentiality of Active-Region Coronae and the Dynamics of the Photospheric Magnetic Field, ApJ, 628, 501–513

Schrijver, C. J., Derosa, M. L., Metcalf, T. R., Liu, Y., McTiernan, J., Régnier, S., Valori, G., Wheatland, M. S., Wiegelmann, T., 2006, Nonlinear Force-Free Modeling of Coronal Magnetic Fields Part I: A Quantitative Comparison of Methods, Sol. Phys., 235, 161–190

Schrijver, C. J., De Rosa, M. L., Metcalf, T., Barnes, G., Lites, B., Tarbell, T., McTiernan, J., Valori, G., Wiegelmann, T., Wheatland, M. S., Amari, T., Aulanier, G., Démoulin, P., Fuhrmann, M., Kusano, K., Régnier, S., Thalmann, J. K., 2008, Nonlinear Force-free Field Modeling of a Solar Active Region around the Time of a Major Flare and Coronal Mass Ejection, ApJ, 675, 1637–1644

Schwenn, R., Marsch, E., 1990, Physics of the Inner Heliosphere I. Large-Scale Phenomena., Springer-Verlag, New York.

Seehafer, N., 1978, Determination of constant alpha force-free solar magnetic fields from magnetograph data, Sol. Phys., 58, 215–223

Seehafer, N., 1982, A comparison of different solar magnetic field extrapolation procedures, Sol. Phys., 81, 69–80

Semel, M., 1967, Contribution à létude des champs magnétiques dans les régions actives solaires, Annales d'Astrophysique, 30, 513–513

Semel, M., 1988, Extrapolation functions for constant-alpha force-free fields - Green's method for the oblique boundary value, A&A, 198, 293–299

Shapiro, A. I., Fluri, D. M., Berdyugina, S. V., Stenflo, J. O., 2007, Molecular Hanle effect in the Paschen-Back regime, A&A, 461, 339–349

Skumanich, A., Lites, B. W., 1987, Stokes profile analysis and vector magnetic fields. I - Inversion of photospheric lines, ApJ, 322, 473–482

Socas-Navarro, H., 2001, Stokes Inversion Techniques: Recent Achievements and Future Horizons, in Advanced Solar Polarimetry – Theory, Observation, and Instrumentation, (Ed.) M. Sigwarth, vol. 236 of Astronomical Society of the Pacific Conference Series, pp. 487

Solanki, S. K., 2003, Sunspots: An overview, Astron. Astrophys. Rev., 11, 153–286

Solanki, S. K., 2004a, SOHO 13 Workshop: '*Waves, Oscillations and Small-scale Transient Events in Solar Atmosphere: A Joint View from SOHO and TRACE*, ESA SP-547, Compiled by: H. Lacoste, p. 155

Solanki, S. K., 2004b, Structure of the solar chromosphere, in Multi-Wavelength Investigations of Solar Activity, (Ed.) A. V. Stepanov, E. E. Benevolenskaya, & A. G. Kosovichev, vol. 223 of IAU Symposium, pp. 195–202

Solanki, S. K., Lagg, A., Woch, J., Krupp, N., Collados, M., 2003, Three-dimensional magnetic field topology in a region of solar coronal heating, Nature, 425, 692–695

Solanki, S. K., Lagg, A., Aznar Cuadrado, R., Orozco Suárez, D., Collados, M., Wiegelmann, T., Woch, J., Sasso, C., Krupp, N., 2006, Measuring the Magnetic Vector with the He I 10830 Å Line: A Rich New World, vol. 358 of Astronomical Society of the Pacific Conference Series, pp. 431

Song, M. T., Fang, C., Tang, Y. H., Wu, S. T., Zhang, Y. A., 2006, A New and Fast Way to Reconstruct a Nonlinear Force-free Field in the Solar Corona, ApJ, 649, 1084–1092

Stenflo, J. O., 1978, The measurement of solar magnetic fields, Reports on Progress in Physics, 41, 865–907

Stenflo, J. O., 1994, Solar magnetic fields, Kluwer Academic Publishers, The Netherlands.

Stix, M., 2002, The sun: an introduction, – 2nd ed. Berlin : Springer

Sturrock, P. A., 1994, Plasma physics. an introduction to the theory of astrophysical, geophysical, and laboratory plasmas, Cambridge, UK: Cambridge University Press.

Sturrock, P. A., Holzer, T. E., Mihalas, D. M., Ulrich, R. K., 1986, Physics of the Sun. Vol. I: The solar interior. Vol. II: The solar atmosphere. Vol. III: Astrophysics and solar-terrestrial relations., Norwell, MA, U.S.A. Kluwer Academic Publishers.

Tadesse, T., Wiegelmann, T., Inhester, B., 2009, Nonlinear force-free coronal magnetic field modelling and preprocessing of vector magnetograms in spherical geometry, A&A, 508, 421–432

Tadesse, T., Wiegelmann, T., Inhester, B., Pevtsov, A., 2011a, Nonlinear force-free field extrapolation in spherical geometry: improved boundary data treatment applied to a SOLIS/VSM vector magnetogram, A&A, 527, A30

Tadesse, T., Wiegelmann, T., Inhester, B., Pevtsov, A., 2011b, Magnetic connectivity between active regions 10987, 10988, and 10989 by means of nonlinear force-free field extrapolation, Sol. Phys., DOI: 10.1007/s11207-011-9764-z

Thalmann, J. K., Wiegelmann, T., Raouafi, N.-E., 2008, First nonlinear force-free field extrapolations of SOLIS/VSM data, A&A, 488, L71–L74

Thompson, M. J., Christensen-Dalsgaard, J., Miesch, M. S., Toomre, J., 2003, The Internal Rotation of the Sun, Ann. Rev. Astron. Astrophys., 41, 599–643

Trujillo Bueno, J., 2001, Atomic Polarization and the Hanle Effect, in Advanced Solar Polarimetry – Theory, Observation, and Instrumentation, (Ed.) M. Sigwarth, vol. 236 of Astronomical Society of the Pacific Conference Series, pp. 161

Trujillo Bueno, J., Asensio Ramos, A., 2007, Influence of Atomic Polarization and Horizontal Illumination on the Stokes Profiles of the He I 10830 Å Multiplet, ApJ, 655, 642–650

Unno, W., 1956, Line Formation of a Normal Zeeman Triplet, Publ. Astron. Soc. Japan, 8, 108

Usmanov, A. V., 1996, A global 3-D MHD solar wind model with Alfvén waves, vol. 382 of American Institute of Physics Conference Series, pp. 141–144

Valori, G., Kliem, B., Keppens, R., 2005, Extrapolation of a nonlinear force-free field containing a highly twisted magnetic loop, A&A, 433, 335–347

Wang, J., 1993, Analyses of Transverse Field (Invited), in IAU Colloq. 141: The Magnetic and Velocity Fields of Solar Active Regions, (Ed.) H. Zirin, G. Ai, & H. Wang, vol. 46 of Astronomical Society of the Pacific Conference Series, pp. 425

Wang, Y., Sheeley, Jr., N. R., 1990, Magnetic flux transport and the sunspot-cycle evolution of coronal holes and their wind streams, ApJ, 365, 372–386

Wheatland, M. S., 1999, A Better Linear Force-free Field, ApJ, 518, 948–953

Wheatland, M. S., 2004, Parallel Construction of Nonlinear Force-Free Fields, Sol. Phys., 222, 247–264

Wheatland, M. S., 2006, A Fast Current-Field Iteration Method for Calculating Nonlinear Force-Free Fields, Sol. Phys., 238, 29–39

Wheatland, M. S., Régnier, S., 2009, A Self-Consistent Nonlinear Force-Free Solution for a Solar Active Region Magnetic Field, ApJL, 700, L88–L91

Wheatland, M. S., Sturrock, P. A., Roumeliotis, G., 2000, An Optimization Approach to Reconstructing Force-free Fields, ApJ, 540, 1150–1155

Wiegelmann, T., 2004, Optimization code with weighting function for the reconstruction of coronal magnetic fields, Sol. Phys., 219, 87–108

Wiegelmann, T., 2007, Computing Nonlinear Force-Free Coronal Magnetic Fields in Spherical Geometry, Sol. Phys., 240, 227–239

Wiegelmann, T., 2008, Nonlinear force-free modeling of the solar coronal magnetic field, J. Geophys. Res., 113, 3

Wiegelmann, T., Inhester, B., 2006, Magnetic Stereoscopy, Sol. Phys., 236, 25–40

Wiegelmann, T., Inhester, B., 2010, How to deal with measurement errors and lacking data in nonlinear force-free coronal magnetic field modelling?, A&A, 516, A107

Wiegelmann, T., Neukirch, T., 2002, Including stereoscopic information in the reconstruction of coronal magnetic fields, Sol. Phys., 208, 233–251

Wiegelmann, T., Neukirch, T., 2003, Computing nonlinear force free coronal magnetic fields, Nonlinear Processes in Geophysics, 10, 313–322

Wiegelmann, T., Inhester, B., Sakurai, T., 2006, Preprocessing of vector magnetograph data for a nonlinear force-free magnetic field reconstruction., Sol. Phys., 233, 215–232

Wiegelmann, T., Neukirch, T., Ruan, P., Inhester, B., 2007, Optimization approach for the computation of magnetohydrostatic coronal equilibria in spherical geometry, A&A, 475, 701–706

Wiegelmann, T., Thalmann, J. K., Schrijver, C. J., De Rosa, M. L., Metcalf, T. R., 2008, Can We Improve the Preprocessing of Photospheric Vector Magnetograms by the Inclusion of Chromospheric Observations?, Sol. Phys., 247, 249–267

Wilhelm, K., Marsch, E., Dwivedi, B. N., Feldman, U., 2007, Observations of the Sun at Vacuum-Ultraviolet Wavelengths from Space. Part II: Results and Interpretations, Space Science Reviews, 133, 103–179

Woltjer, L., 1958, The Stability of Force-Free Magnetic Fields., ApJ, 128, 384

Wu, S. T., Sun, M. T., Chang, H. M., Hagyard, M. J., Gary, G. A., 1990, On the numerical computation of nonlinear force-free magnetic fields, ApJ, 362, 698–708

Yan, Y., Li, Z., 2006, Direct Boundary Integral Formulation for Solar Non-constant-α Force-free Magnetic Fields, ApJ, 638, 1162–1168

Yan, Y., Sakurai, T., 2000, New Boundary Integral Equation Representation for Finite Energy Force-Free Magnetic Fields in Open Space above the Sun, Sol. Phys., 195, 89–109

Yang, W. H., Sturrock, P. A., Antiochos, S. K., 1986, Force-free magnetic fields - The magneto-frictional method, ApJ, 309, 383–391

Zeeman, P., Winawer, B., 1910, The Magnetic Separation of Absorption Lines in Connection with Sun-Spot Spectra, ApJ, 32, 329

Publications

Refereed publications

❶ *Magnetic connectivity between active regions 10987, 10988, and 10989 by means of nonlinear force-free field extrapolation*,
Tilaye Tadesse, Wiegelmann, T., Inhester, B., and Pevtsov A.,
Solar physics, *DOI: 10.1007/s11207-011-9764-z.*

❷ *Nonlinear force-free field extrapolation in spherical geometry: improved boundary data treatment applied to a SOLIS/VSM vector magnetogram*,
Tilaye Tadesse, Wiegelmann, T., Inhester, B., and Pevtsov A.,
Astronomy & Astrophysics, *Mar 2011, volume **527**, A(30).*

❸ *Nonlinear force-free coronal magnetic field modelling and preprocessing of vector magnetograms in spherical geometry,*
Tilaye Tadesse, Wiegelmann, T., and Inhester, B.,
Astronomy & Astrophysics, *Dec 2009, volume **508**, pp. 421-432.*

❹ *A Critical Assessment of Nonlinear Force-Free Field Modeling of the Solar Corona for Active Region 10953*,
DeRosa, M. L., Schrijver, C. J., Barnes, G., Leka, K. D., Lites, B. W., Aschwanden, M. J., Amari, T., Canou, A., McTiernan, J. M., Régnier, S., Thalmann, J. K., Valori, G., Wheatland, M. S., Wiegelmann, T., Cheung, M. C. M., Conlon, P. A., Fuhrmann, M., Inhester, B. and **Tilaye Tadesse**,
The Astrophysical Journal, *May 2009, volume **696**, pp. 1780-1791.*

Oral presentations

✞ **December 14, 2010**,
Institute for Geophysical and extraterrestrial physics, Technical University of Braunschweig
Braunschweig, Germany,
Nonlinear force-free reconstruction of the coronal magnetic field with advanced numerical methods, by **Tilaye Tadesse**

✞ **July 18-25, 2010**,
38th COSPAR Scientific Assembly,
Bremen, Germany,

Nonlinear force-free field extrapolation in spherical geometry: improved boundary data treatment applied to a SOLIS/VSM vector magnetogram, by **Tilaye Tadesse**, Wiegelmann, T., and Inhester, B.

- **July 7, 2010**,
  Solar System Seminar,
  Katlenburg-Lindau, Germany,
  Nonlinear force-free field extrapolation of a SOLIS/VSM vector magnetogram in spherical geometry, by **Tilaye Tadesse**, Wiegelmann, T., and Inhester, B.

- **July 15, 2009**,
  Solar System Seminar,
  Katlenburg-Lindau, Germany,
  Nonlinear force-free coronal magnetic field modeling and preprocessing of vector magnetograms in spherical geometry, by **Tilaye Tadesse**, Wiegelmann, T., and Inhester, B.

- **Jun. 23-25, 2009**,
  NLFFF Consortium Meeting 6,
  St. Andrews University, Scotland, UK,
  NLFF coronal magnetic field modeling and preprocessing of vector magnetograms in spherical geometry: a test on synthetic data, by **Tilaye Tadesse**, Wiegelmann, T., and Inhester, B.

- **Jan. 14, 2009**,
  Solar System Seminar,
  Katlenburg-Lindau, Germany,
  Nonlinear force-free reconstruction of solar corona magnetic fields in spherical geometry using an optimization method by **Tilaye Tadesse**, Wiegelmann, T., and Inhester, B.

- **Oct. 22 - 23, 2008**,
  A Next Generation Coronal Active Region Model Workshop,
  Drexel University, Philadelphia, USA,
  Nonlinear force-free extrapolation of solar corona magnetic fields in spherical geometry using an optimization method: a case for synthetic magnetogram, by **Tilaye Tadesse**, Wiegelmann, T., and Inhester, B.

- **Jun. 30 - Jul. 2, 2008**,
  NLFFF Consortium Meeting 5,
  Katlenburg-Lindau, Germany,
  NLFF coronal magnetic field extrapolation in spherical coordinates for part of a sphere, by **Tilaye Tadesse**, Wiegelmann, T., and Inhester, B.

- **Sep. 27, 2007**,
  Max-Planck Institute for solar system research,
  Katlenburg-Lindau, Germany,
  Comparison of different numerical algorithms for the determination of potential fields in the solar corona, by **Tilaye Tadesse**, and Wiegelmann, T.

Acknowledgements

Glory be to The Name of The **Lord**, **Jesus Christ**, who gives us all of his blessings, and great peace of heart and mind along with everlasting life. I would like to express my deepest gratitude to my two supervisors at the Max Planck Institute for Solar System Research (MPS) **Dr. Thomas Wiegelmann** and **Dr. Bernd Inhester** for their continuous guidance, motivation and support during my entire PhD research. Special thanks to **Dr. Thomas Wiegelmann** for all his patience, valuable discussions and interest for my work. I am very grateful for his great support and efforts throughout my PhD time, for helping me with IDL, C and Unix problems and for always being in a good temper. Thanks to him I learned a lot about programming in IDL and C. I learnt lots of things from **Dr. Bernd Inhester** ranging from preparing presentation, writing paper, numerics and concepts of physics. He is such extraordinary teacher with full of knowledge and eagerness to teach others. His ability in explaining stuff in a more simplified manner and the freedom he gives us to approach him at any time and anywhere is truly admirable. I really appreciate the wonderful working environment inside the corona 3-D group where I always felt comfortable about collaborating with everybody. Apart from many useful scientific discussions they show a good sense of humor providing an extremely friendly atmosphere. I also want to thank my supervisor at the Technical University of Braunschweig **Prof. Dr. Sami Solanki** and **Prof. Dr. Karl-Heinz Glaßmeier** for careful reading of this thesis and useful remarks.

I would like to express my gratitude to my colleague **Dr. Julia Thalmann** for her great efforts in assisting me and many valuable discussions during my entire PhD research. I would like to thank the Directors of MPS, **Prof. Dr. Sami Solanki** and **Prof. Dr. Ulrich Christensen** as well as the International Max Planck Research School (IMPRS) for financing this work and for giving me the great opportunity to work in an exciting scientific environment. Special thanks deserves **Dr. Dieter Schmitt**, the coordinator of the IMPRS, for his support and great efforts in organizing all the seminars and retreats which contributed to the broadening of our knowledge. Thank you, **Dieter**, for giving the chance to many students and me to work in such a great institute. Many thanks also to **Petra Fahlbusch** and **Claudia Rudolph** for all their cordiality, kindliness and for helping me with my non-scientific matters making my life in Lindau easier. I want to express my gratitude to my friends **Shangbin Yang**, **Yacine Saidi**, **Jean-Baptiste Vincent**, **Iulia Chifu**, **Judith de Patoul**, **Chemeda Ejeta**, **Hailu Kebede**, **Mohammed Kedir** and **Belete Regassa** for their valuable discussions and encouragement. Most of all, I want to express my special thanks to my friend and colleague at Addis Ababa University, **Mekbib Alemu**, for taking care of my affairs and his encouragement. Thank you **Mekbibe**.

Finally, I am deeply grateful to my wife **Aklil Metaferia** for supporting in every aspect of my life. Thank you, **Aklil**, for all your love, patience, encouragement and taking care of our son **Zerubbabel**. Without your support I would have never been able to carryout research both during Msc and PhD. I feel very confident that **God** will teach us how to serve **Him** for the rest of our lives.

Curriculum Vitae

Education

1995	**Bachlor of science in physics**, Addis Ababa University (AAU), Department of Physics, Addis Ababa, Ethiopia
2005	**Master of science in physics**, Addis Ababa University (AAU), Department of Physics, Addis Ababa, Ethiopia
2008-2010	**PhD student**, International Max Planck Research School for Solar System and Beyond, Katlenburg-Lindau, Germany

Scientific Experience

2004	MASTERS THESIS, Addis Ababa University (AAU), Addis Ababa, Ethiopia *Braking index of isolated pulsars according to the relativistic plasma diffusion theory for pulsar fields.*
2007	THREE MONTHS RESEARCH VISIT, Max Planck Institute for Solar System Research, Katlenburg-Lindau, Germany *Comparison of different numerical algorithms for the determination of potential fields in the solar corona*
2008-2010	PHD THESIS, Max Planck Institute for Solar System Research, Katlenburg-Lindau, Germany *Nonlinear force-free reconstruction of the coronal magnetic field with advanced numerical methods.*

Teaching Experience

1996-1998	**Full time physics teacher** Bule Hora/ Hagere mariam high school, Bule Hora (Hagere mariam), Borena Zone, Oromia, Ethiopia
1999-2003	**Full time physics teacher** Bore high school, Bore, Guji Zone, Oromia, Ethiopia
2005	**Full time physics lecturer** (Undergraduate students), Jimma University (JU), Jimma, Ethiopia
2005-2008	**Full time physics lecturer** (Undergraduate students), Addis Ababa University (AAU), Addis Ababa, Ethiopia

Additional information

Nationality	Ethiopian
Languages	Afaan Oromoo , Amharic, English (fluent)
Computer skills	Daily usage of Windows and Unix, large experience in programming (IDL, C, FORTRAN, and with various software (Latex, Word, Excel, Powerpoint).